CLRC

Lecture notes from the Training Course in Pulsed µSR Techniques

S H Kilcoyne (Editor)

March 1996

Lecture notes from the

TRAINING COURSE

IN

PULSED μSR TECHNIQUES

Edited by S H Kilcoyne

Contributors

R Cywinski (St Andrews University)
μSR: Muon spin rotation and relaxation

G H Eaton (ISIS)
The ISIS pulsed muon facility : Muon beamline

C A Scott (ISIS)
The ISIS pulsed muon facility : Instrumentation

B D Rainford (Southampton University)
Aspects of data treatment of transverse μSR

S L Lee (Zurich University)
Using positive muons to investigate high temperature superconductors

E A Davis (Leicester University)
Muonium states in crystalline and amorphous semiconductors: relationship to hydrogen centres

S F J Cox (ISIS)
Muon sites and electronic structure

μSR: MUON SPIN ROTATION AND RELAXATION

R Cywinski
J J Thomson Physical Laboratory, University of Reading, Reading RG6 2AF

μSR is an abbreviation for Muon Spin Rotation, Relaxation or Resonance. In this lecture I shall deal with only the first two of these techniques, i.e. the two which are most commonly used in studies of magnetic systems. However, it should be noted that all μSR is strictly a magnetic phenomenon: it is based upon the observation of the evolution with time of the direction of the muon's spin in the magnetic field at the muon site in a sample. Through such observations the magnitude, distribution and dynamics of the internal field can be probed. In fact, so sensitive is μSR that the distribution of fields arising from *nuclear* moments is easily measured.

The first part of the lecture provides an introduction to the basic concepts of μSR, starting with the production of a muon beam and the interaction of individual muons with matter, and leads to the experimental geometries associated with (transverse field) muon spin rotation and (zero or longitudinal field) muon spin relaxation techniques. In the discussion of these techniques I shall introduce and define terms such as *asymmetry, damping rate, depolarisation,* and *Kubo-Toyabe function,* which commonly appear in μSR publications.

I shall then provide some specific examples, (although by no means a comprehensive review !), of the use of muon spin rotation and relaxation in studies of variety of magnetic systems including ordered magnets, spin fluctuating paramagnets and spin glass systems, together with some recent results which point to possible future applications of the muon technique.

For a more detailed and rigorous survey of μSR techniques, I recommend the following references:

A Schenck *Muon Spin Rotation Spectroscopy* Adam Hilger (1985)

J Chappert and R J Grynszpan *Muons and Pions in Materials Research* Elsevier Science (1984)

S J F Cox *Implanted Muon Studies in Condensed Matter Science* J Phys C: Solid State Physics **20** (1987) 3187

Proceedings of the International Conferences on μSR: Hyperfine Interactions, Vol 31(1986), Vol 64 (1990), (1993 in press).

The Muon

Property	Values
Mass (m_μ)	206.76835(11) x m_e
	= 0.1126096 x m_p
Charge	+e, -e
Spin (I)	1/2

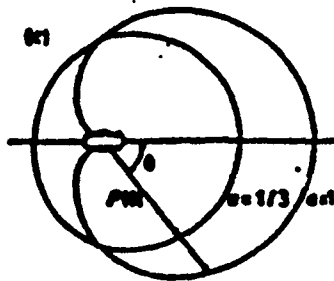|	
Magnetic Moment	$3.1833452(10) \times \mu_p$
Gyromagnetic Ratio	$1.355342 \times 10^8 \text{ s}^{-1}\text{T}^{-1}$
Lifetime	$2.19714(7) \mu_s$

(a)   muon produced from pion decay: $\pi^+ \rightarrow \mu^+ + \nu_\mu$ $(\tau_\pi = 26\text{ns})$

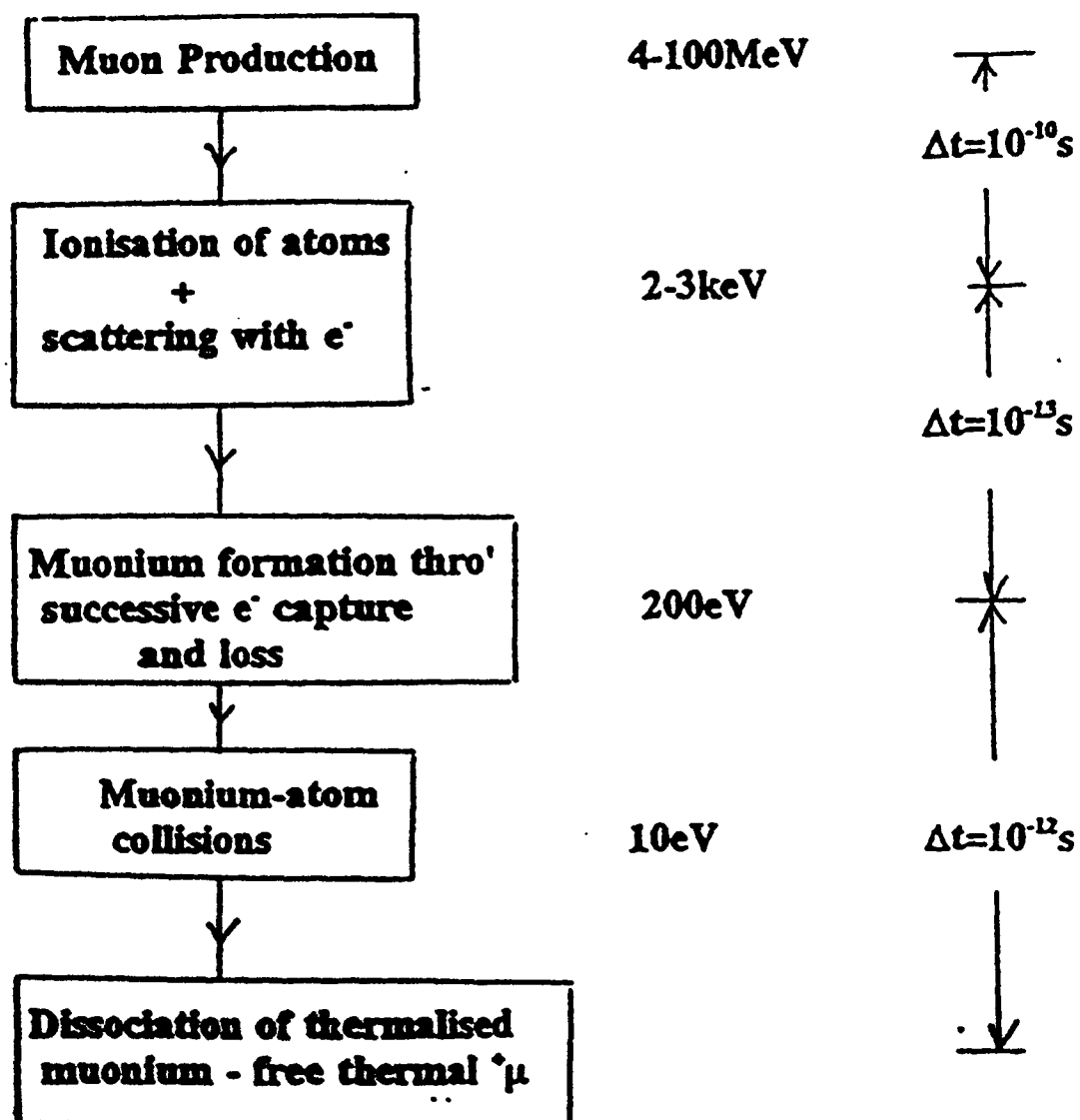(b)   decay of the muon: $\mu^+ \rightarrow e^+ + \nu_\varepsilon + \nu_\mu$

(c)   Angular distribution of the positron intensity: a is the *asymmetry* parameter.

$^+\mu$ thermalisation in metals

Note:

(i)   Depolarisation is proportional to fractional energy loss (i.e. α $(m_c/m_\mu).(v^2/c^2)$)

(ii)   Some atomic displacement may occur, but usually only at the surface on the material

Muon Spin Rotation

(a) Implantation

Polarized beam

Sample

B (b) Precession

(c) Decay

1+a cos θ polar diagram

Scintillator

Forward detector field = 0.0035 T

gaussian damping sigma = 0.1

positron counts

time (microseconds)
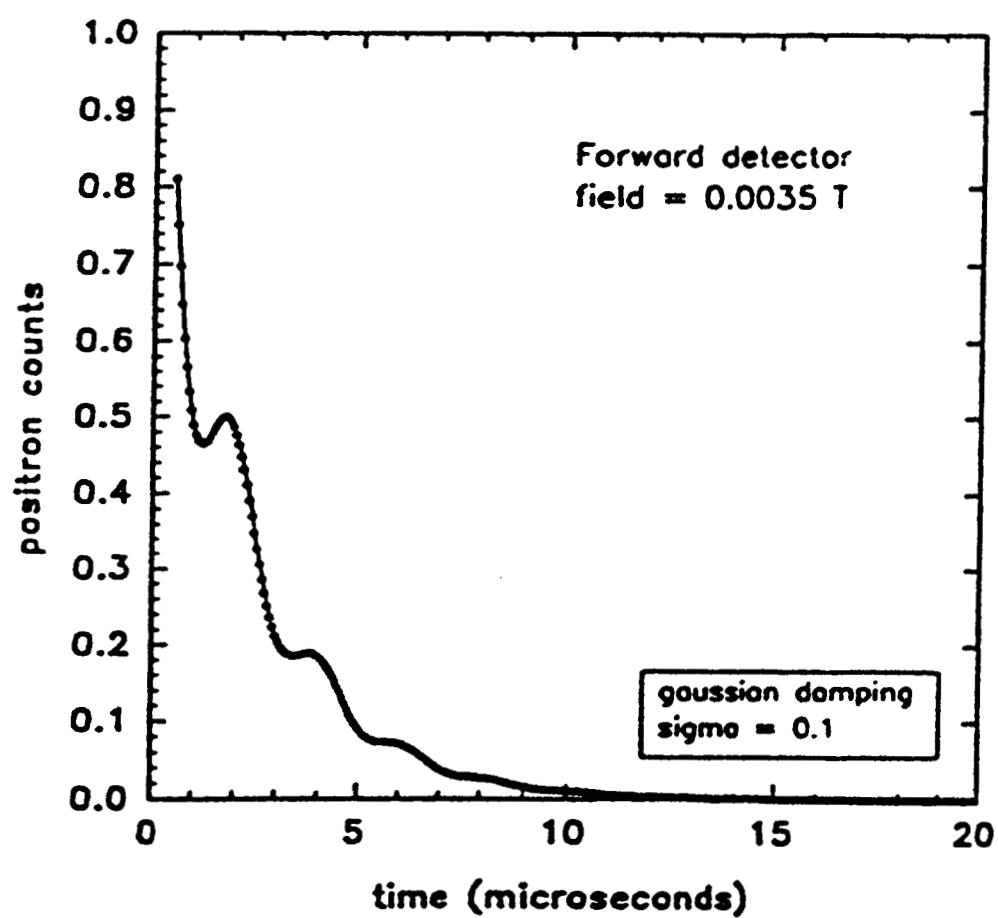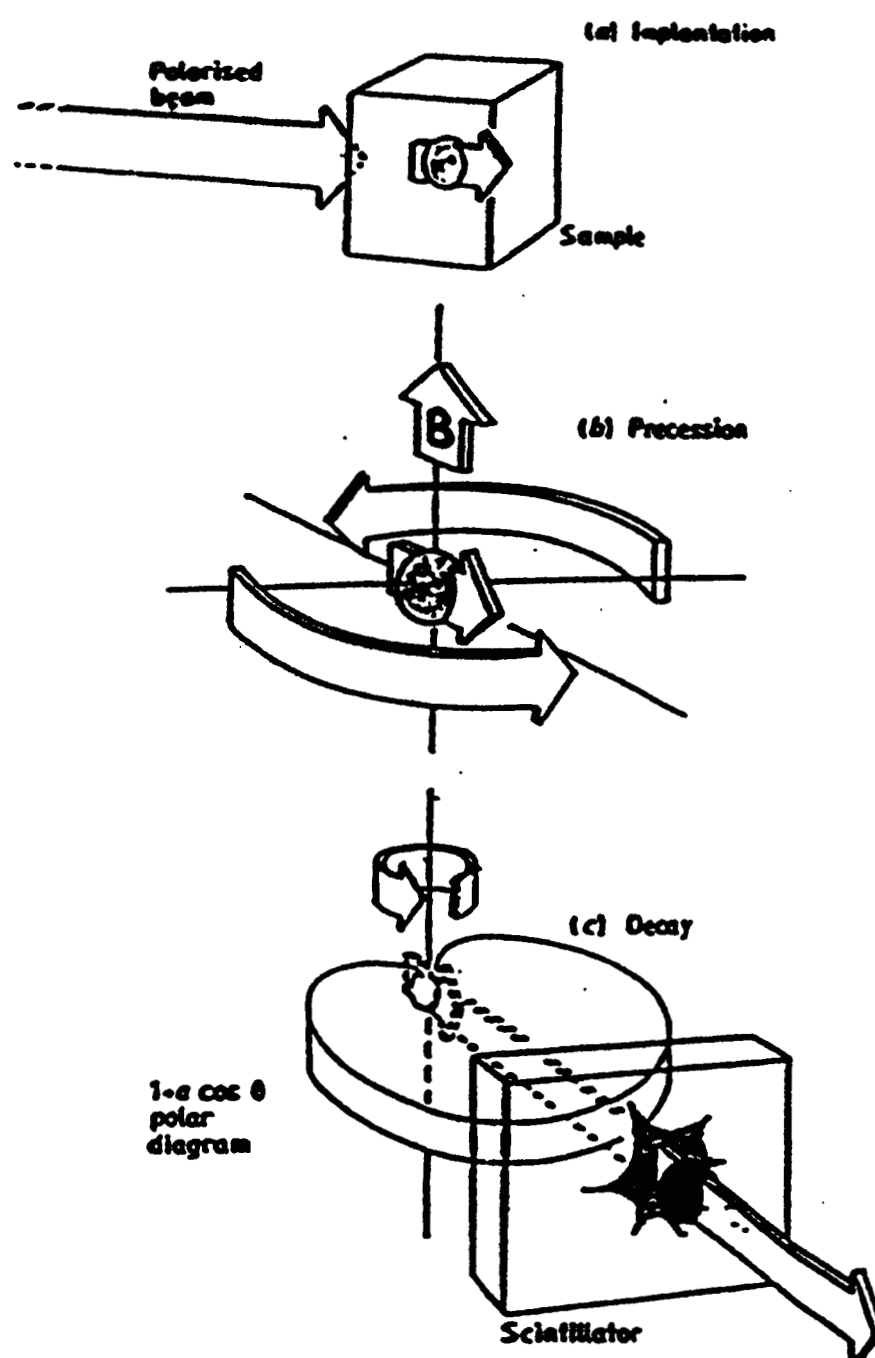
Positron emission preferentially in direction of S_μ

$$W_\theta = 1 + a_0\cos\theta$$

a_0 is the *asymmetry* parameter

The countrate in the forward and backward detectors is:

$$N_{F,B} = N_o exp(-t/\tau_\mu).[1 \pm a_o]$$

with + = F and - = B, $\tau_\mu = 2.2\mu s^{-1}$

In the presence of a static magnetic field B, $\omega_L = \gamma B_\mu$ ($\gamma = 135MHz/T$)

$$N_{F,B} = N_o exp(-t/\tau_\mu).[1 \pm a_o \cos(\omega_L t)]$$

All muons precess with same frequency (no depolarisation). If this is violated we need a (*transverse*) relaxation function: $G_x(t)$

$$R(t) = (N_F(t) - N_B(t)/N_F(t) + N_B(t)) = a_o G_x(t) \cos \omega_L t)$$

$G_x(t)$ is determined by the magnetic (nuclear or atomic) field distribution and dynamics at the muon site:

Static Limit

Depolarisation is assumed to result from a continuous and isotropic Gaussian distribution of *static* fields

$$P(B_x) = \frac{\gamma_\mu}{\sqrt{2\pi}\sigma_x} \exp\left(-\frac{\gamma_\mu^2 B_x^2}{2\sigma_x^2}\right)$$

giving a Gaussian form for $G_x(t)$

$$Gx(t) = \exp(-\frac{1}{2}\sigma_x^2 t^2)$$
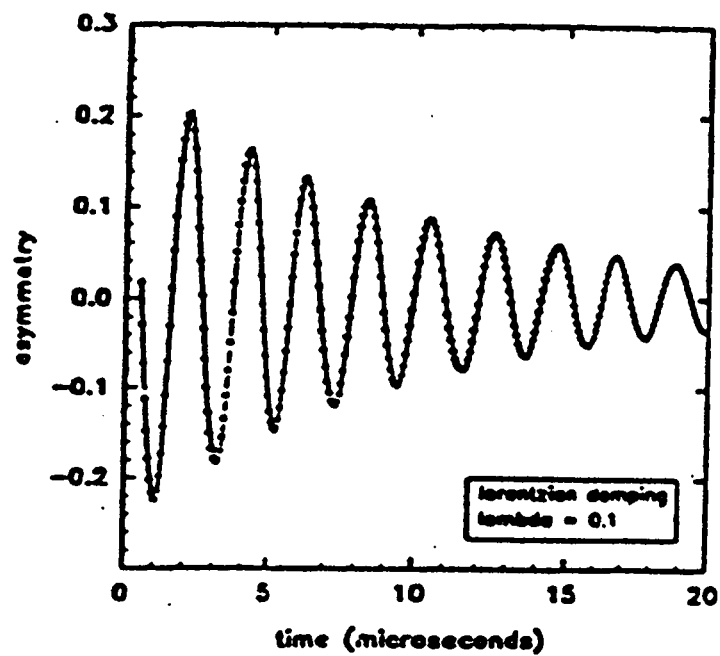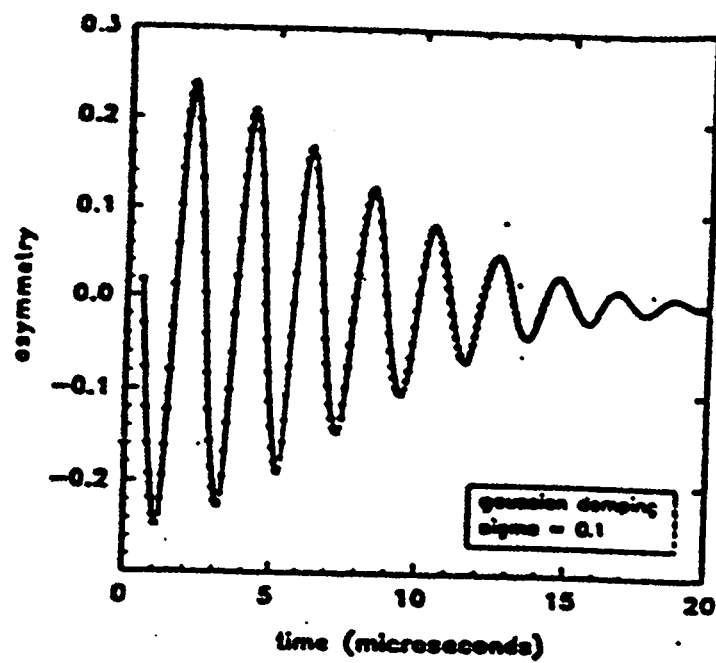
where $\sigma_x^2 = \gamma^2 < B_\mu^2 >$

Dynamic Limit (Fast Fluctuations)

Should the random fields *fluctuate* (either because the muon is hopping, or because the local moments fluctuate) with a correlation time τ_c such that $\tau_c \sigma_x << 1$, $G_x(t)$ has the exponential form

$$G_x(t) = \exp(-\sigma_x^2 \tau_c t)$$

or

$$G_x(t) = \exp(-\lambda t) = \exp(-\frac{t}{T_2})$$

Intermediate Fluctuation Rate Regime

In the limit between the slow (static) and fast ($\tau_c \sigma_x \ll 1$) fluctuation limits *Abragam* has shown

$$G_x(t) = \exp\left\{-\sigma_x^2 \tau_c^2 [\exp(-t/\tau_c) - 1 + t/\tau_c]\right\}$$

Hayano et al (PRB20 (1979) 850 have calculated explicitly for the full range of fluctuation rates $1 \ll \tau_c \sigma_x \ll 1$:
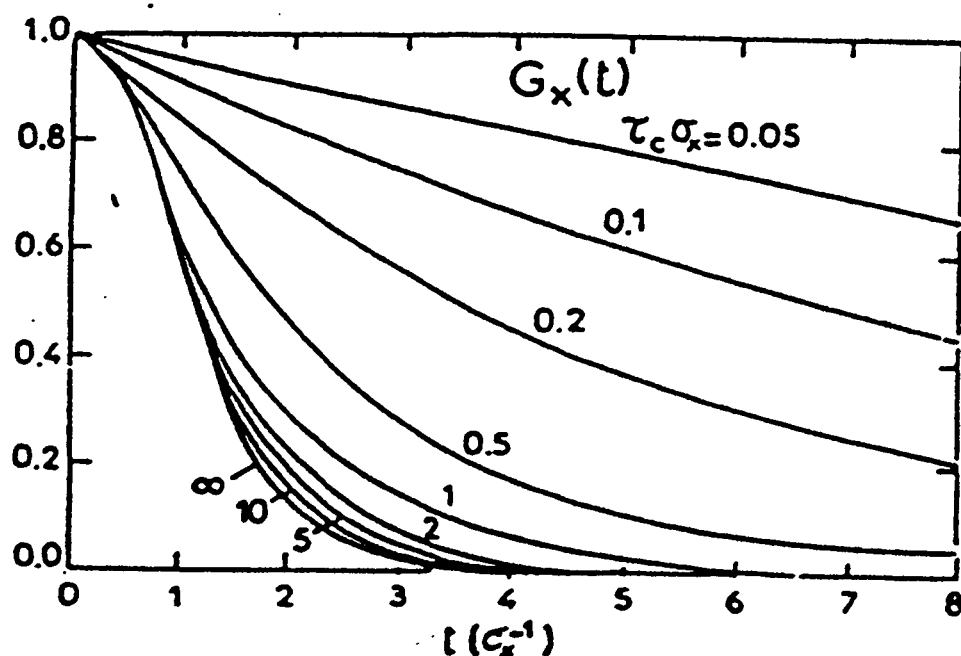
It is clearly difficult to extract accurate data in the limit of slow fluctuations ($\tau_c \sigma_x > 1$). Hence the need for zero field μSR.

Muon Spin Relaxation
Geometry:

$$R(t) = (N_F(t) - N_B(t))/(N_F(t) + N_B(t)) = a_0 G_z(t)$$

where $G_z(t)$ is the longitudinal relaxation function, and is a calibration term which accounts for the relative efficiencies of the F and B detectors.

Zero and Longitudinal Fields

Zero field μSR is more sensitive than transverse field muon spin rotation.
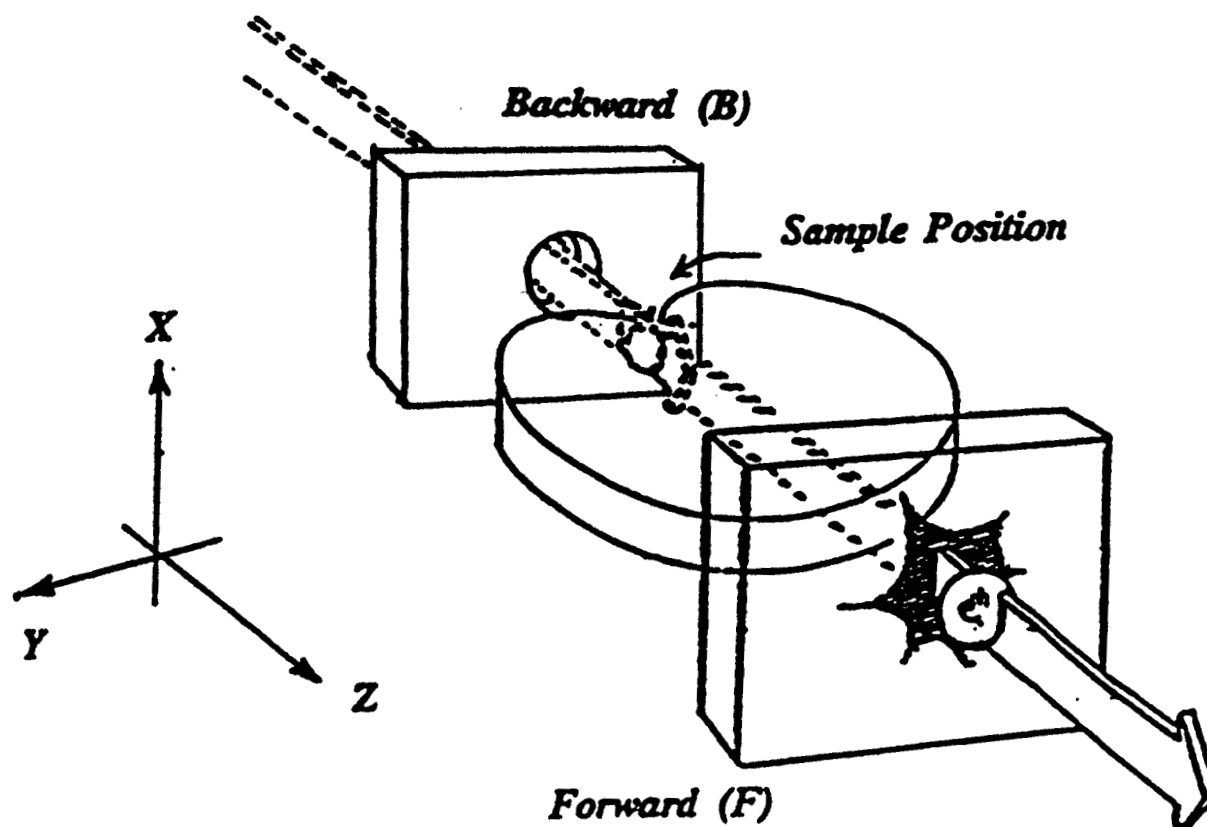
A muon implanted in a sample in zero field will not precess in the absence of an *internal* local field. Any coherent precession in the muon polarisation indicates the presence of a coherent internal field (i.e. long range order).

Any measure decay of the initial asymmetry indicates components of field perpendicular to the initial muon polarisation.

$G_z(t)$ is generally more complex than $G_x(t)$, but at short times Gaussian $G_z(t)$ implies static local moment and a stationary muon.
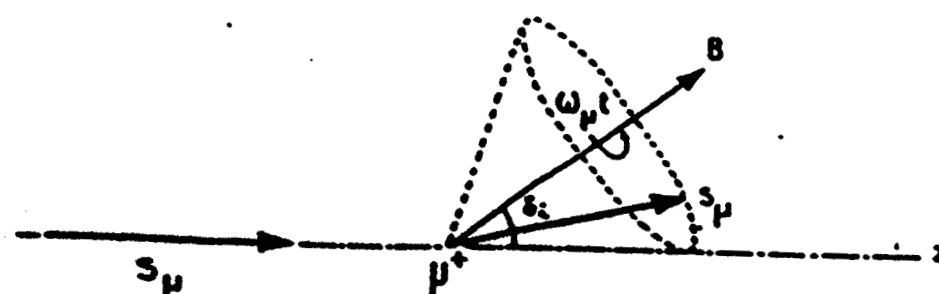Exponential $G_z(t)$ implies either a mobile muon or fluctuating moments.

A characteristic of *static* moments and muon is the recovery of the asymmetry to 1/3 of its initial value at long times (as predicted by Kubo and Toyabe).

A sufficiently strong external field will preserve initial asymmetry.

Zero External Field
Static Local Fields

The time evolution of the longitudinal component of the muon polarisation is

$$P_z(t) = \cos^2\delta_i + \sin^2\delta_i\cos\omega_\mu t$$

with $\omega_\mu = \gamma_\mu B$

Averaging over all directions of B gives

$$<P_x(t)> = \frac{1}{3} + \frac{2}{3}<\cos\omega_\mu t>$$

Adding a Gaussian field distribution gives the Kubo-Toyabe form

$$G_x(t) = \frac{1}{3} + \frac{2}{3}(1 - \sigma_z^2 t^2)\exp(-\frac{1}{2}\sigma_z^2 t^2)$$

where $\qquad \sigma_z^2 = \gamma_\mu^2 <B_x^2> = \gamma_\mu^2 <B_y^2> = \gamma_\mu^2 <B_z^2>$ $\qquad$.

The Kubo-Toyabe Function

Hayano et al (PRB20 (1979) 850) applied the Kubo-Toyabe formulae to zero and longitudinal field μSR:

$$G_z(t) = \frac{1}{3} + \frac{2}{3}(1 - \sigma^2 t^2)e^{-\frac{\sigma^2 t^2}{2}}$$

Expressing the external field strength in units of $\gamma B/\sigma$ and time in units of σ^{-1} where $\sigma = \gamma_\mu <B_\mu^2>^{-1/2}$ we have
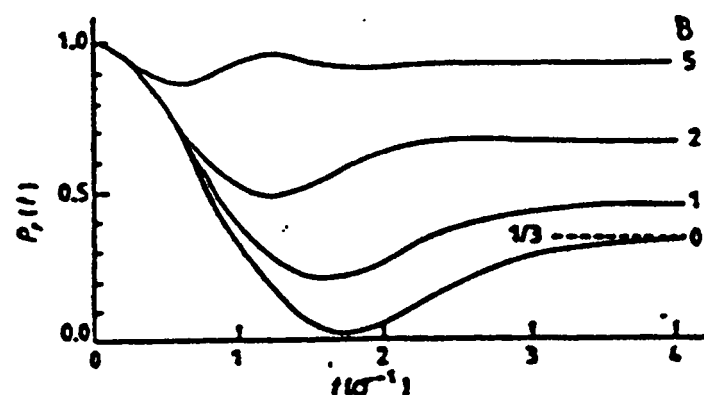
A more complex (exponentially decaying) form is observed if the muon is hopping at a rate of τ_c^{-1}
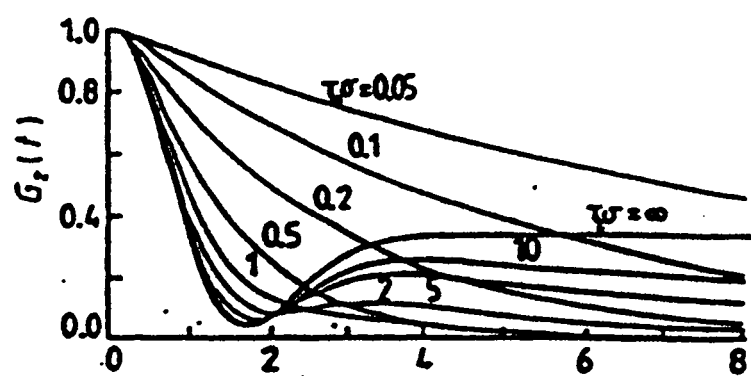
Summary

In both transverse and longitudinal geometry the aim is to extract G(t) and its evolution with temperature.

G(t) provides information on the distribution and dynamics of internal fields at the muon site.

Gaussian G(t) - static moments, static muon

Exponential G(t) - fluctuating moments, or hopping muon small λ, small rms field and/or rapid fluctuations large λ, large rms fields and/or slower fluctuations.

Clearly many other forms of G(t), and complex combinations of these forms can arise.

Calculated G(t) must also account for muon tunnelling, diffusion to and from traps etc.

Zero field μSR provides greater sensitivity to slow fluctuations and ability to measure coherent internal fields (magnetic order).

Transverse field μSR enables muon Knight shift to be determined.
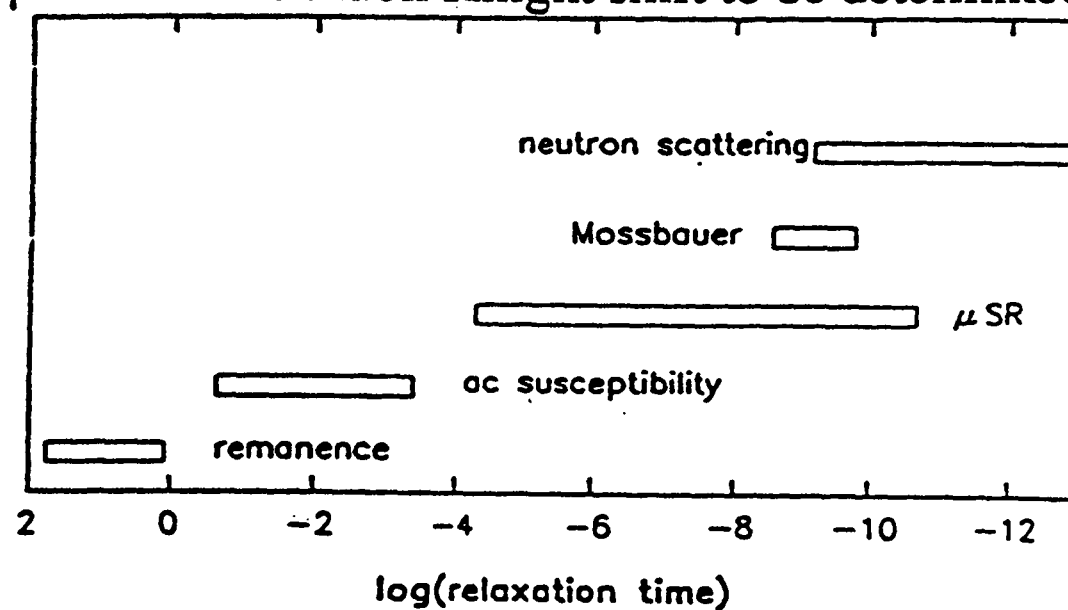
Transverse Field μSR on Ce/As
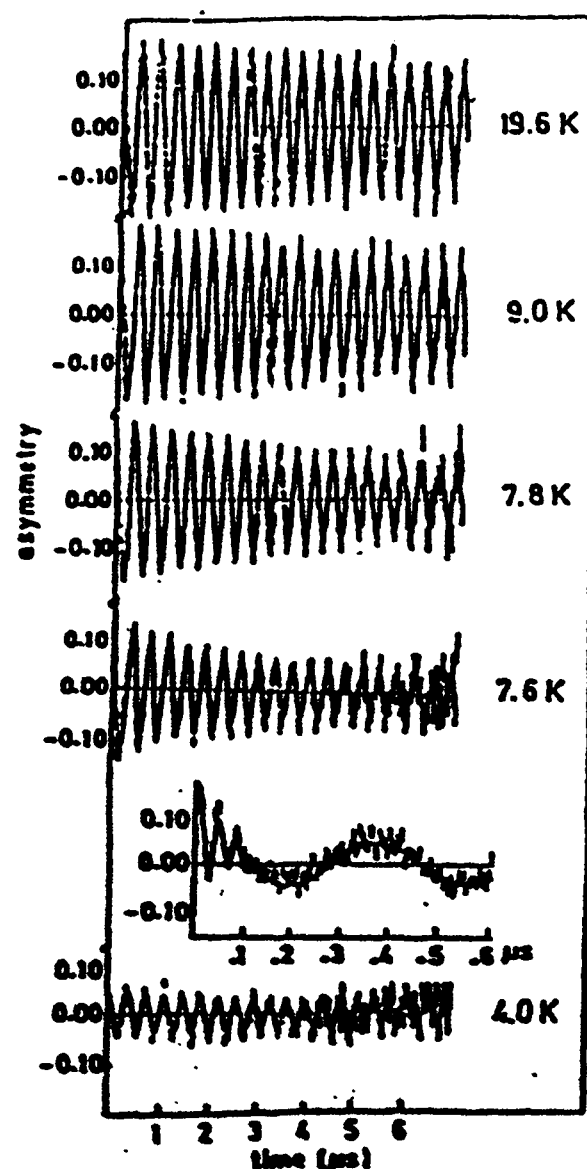
Transverse field spectra in 20mT. The inset at 4K shows the μSR at short times (the residual oscillations are attributed to cryostat background).

Litterst et al Hyp Int 64 (1990) 443

From the transverse field data the damping rate and muon Knight shift (in this case a negative Knight shift) can be determined.
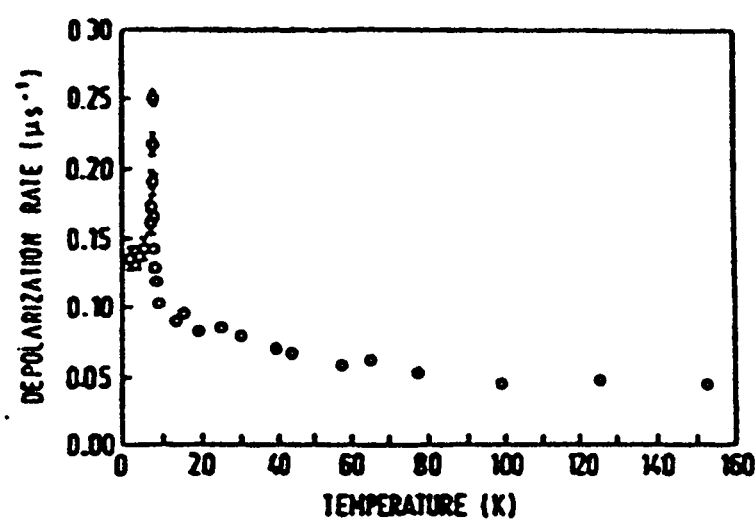
Fig. 2. Temperature dependence of the transverse field depolarization rate.
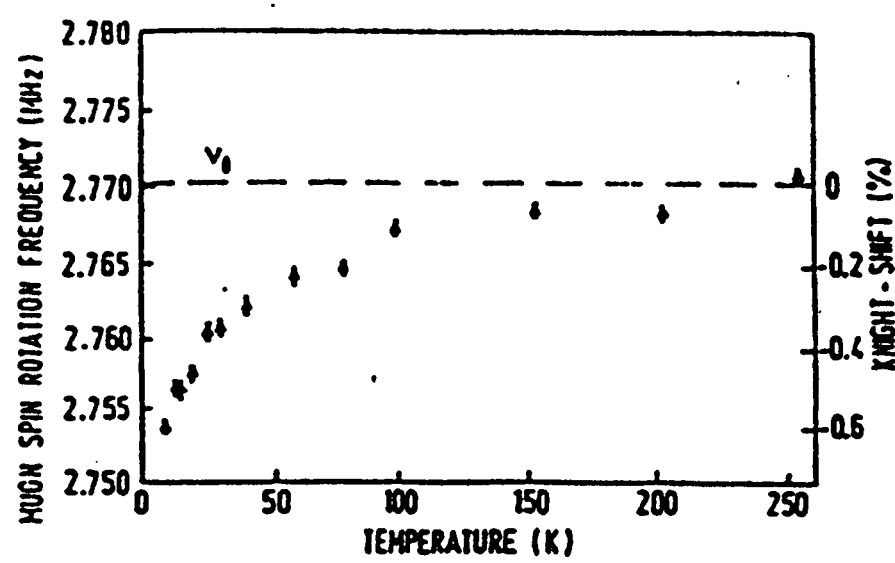
Fig. 5. Paramagnetic Knight shift as a function of temperature.

Longitudinal Measurements on Ordered Magnets

In an ordered ferro- or antiferromagnet a unique internal field at the muon site will give rise to a spontaneous coherent rotation:

$$A(t) = \frac{1}{3}G_1(t) + \frac{2}{3}G_\perp(t)\cos(\omega t)$$

Gadolinium:
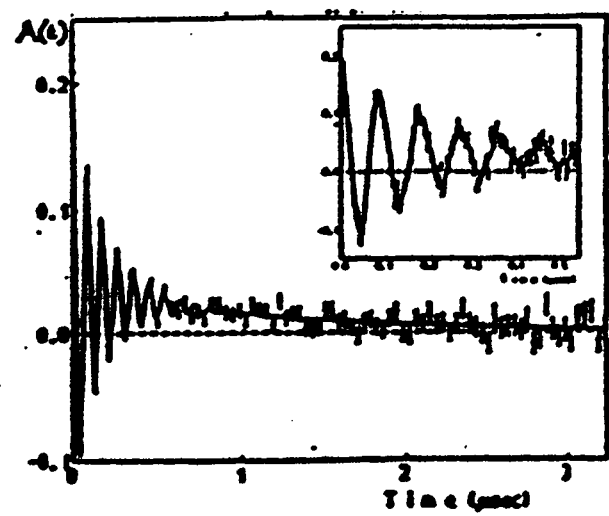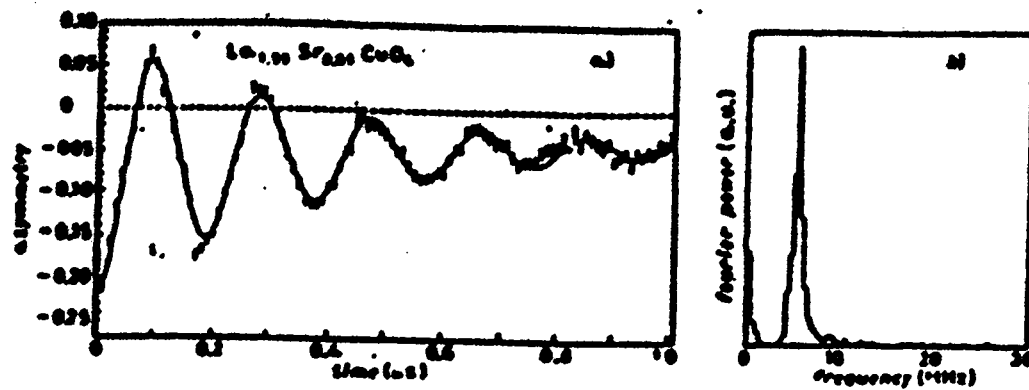
La₂CuO₄:
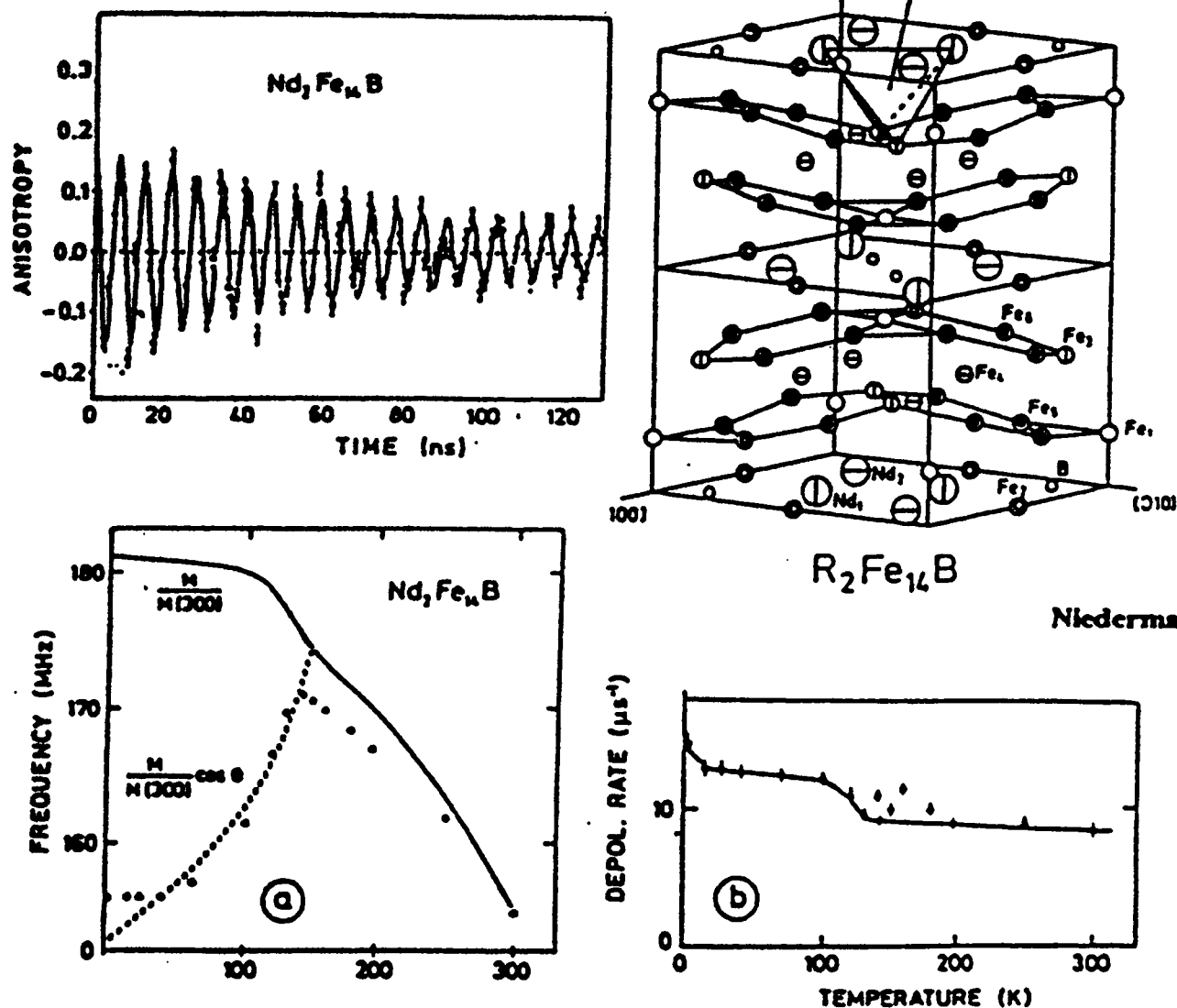
Nd₂Fe₁₄B:

$R_2Fe_{14}B$

Niedermayer et al Hyp Int 64 (1990) 405

Itinerant Magnets

One of the earliest and most successful μSR studies was that of the weak itinerant electron ferromagnet MnSi:

Measurements at 285K show the muon is stationary, while measurements in a longitudinal field of 700Oe leave only the exponential relaxation due to fluctuating atomic spins.
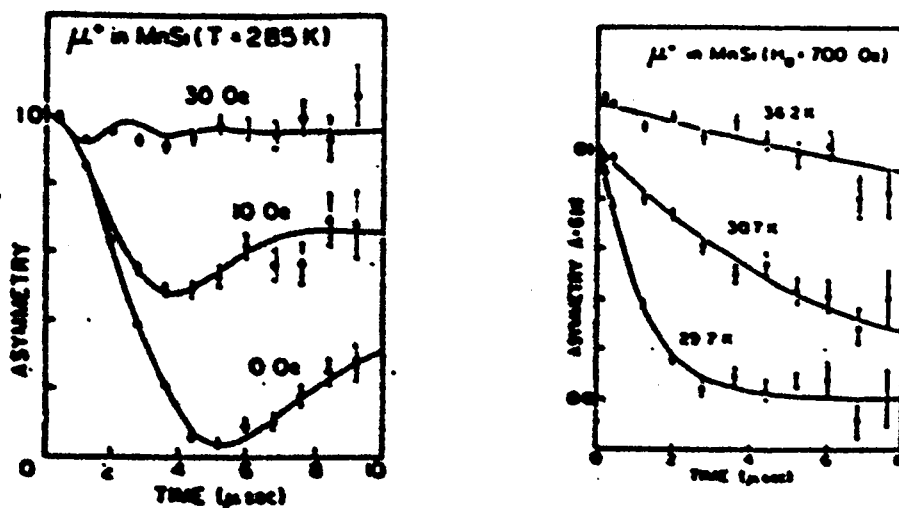
$1/T_1$ determined by fitting $G_z(t) = \exp(-\lambda t)$, NMR data fit SCR theory extremely well:

Hayano et al PRL 41 (1978) 1743
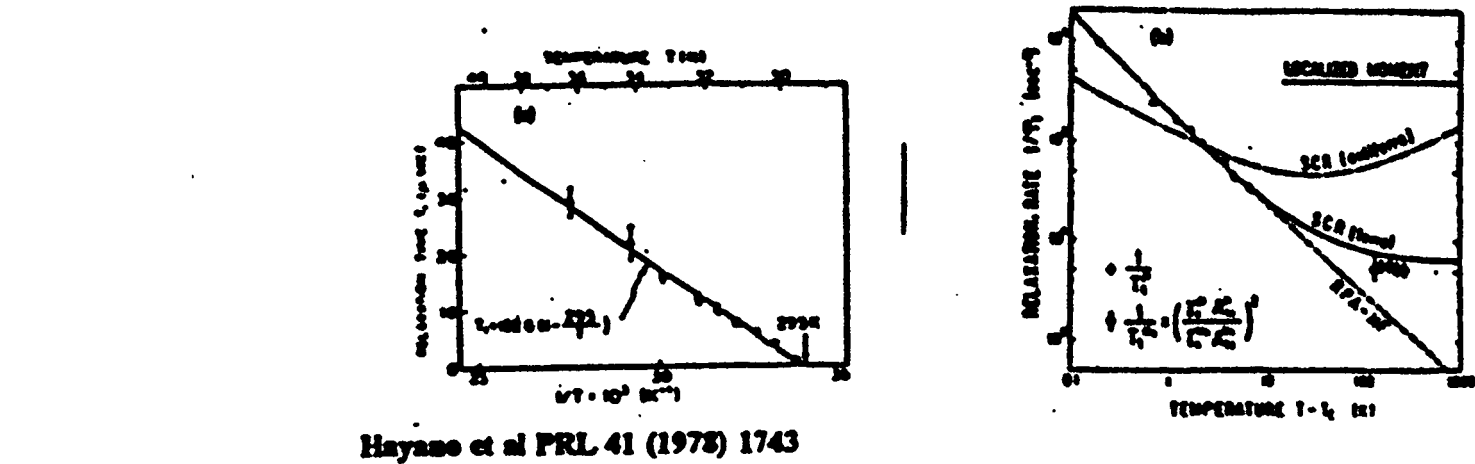
Spin Glass Systems

Uemura et al (PRB31 (1985) 546) were able to show that a

"root exponential"

form for $G_z(t)$ can obtain for spin glass systems in zero field:

$$G_z^U(t) = \frac{1}{3}e^{-\lambda_d t^{\frac{1}{2}}} + \frac{2}{3}\left(1 - \frac{\lambda_s^2 t^2}{(\lambda_s^2 t^2 + \lambda_d t)^{\frac{1}{2}}}\right)e^{-(\lambda_d t + \lambda_s^2 t^2)^{\frac{1}{2}}}$$

where λ_s and λ_d are the static and dynamic components of the relaxation respectively.

μ^+ in $\underline{Cu}Mn$ (5 at.%, $T_g = 27.4$ K)
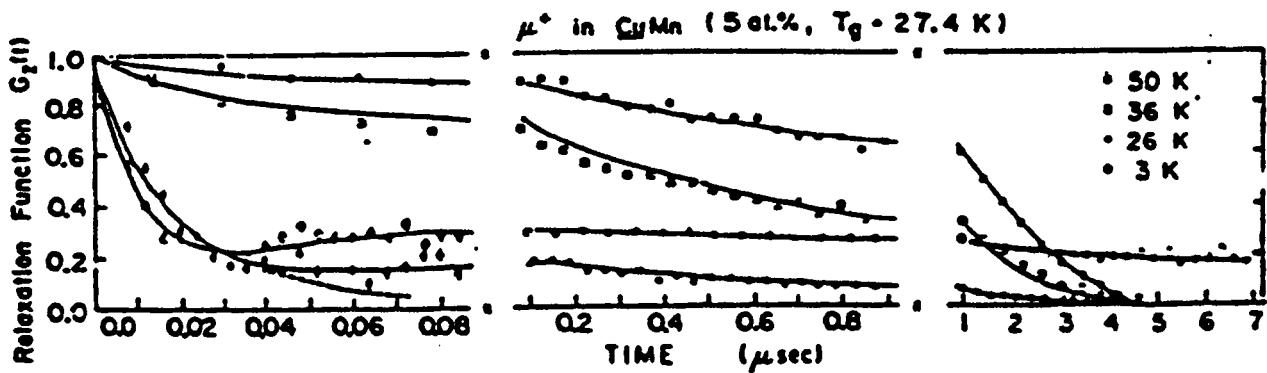
Spin Glasses above T_g

Theory predicts that above T_g the spin correlation function in a spin glass follows the Kohlsrauch form:

$$q(t) = \overline{<S_x(0)S_x(t)>} \propto \exp(-(\omega t)^\beta))$$

Monte Carlo calculations (Ogielski, PRB 32, 1985, 7348) show that β is temperature dependent:
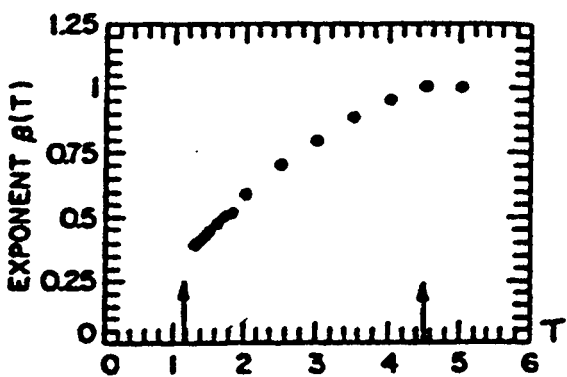
μSR has recently (1993) indicated that $G_z(t) = \exp(-(\lambda t)^\beta)$ with β showing the same temperature dependence:
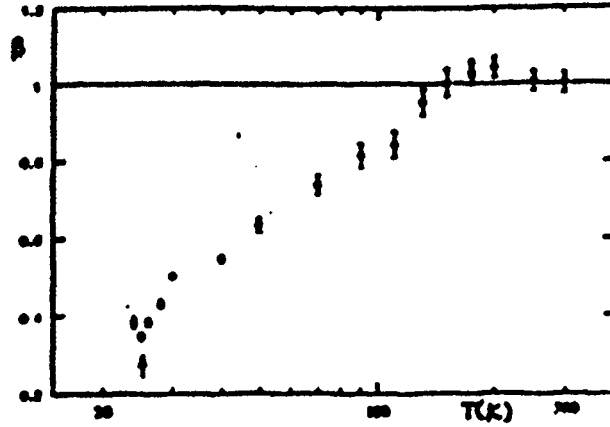
The precise relationship between $G_z(t)$ and $q(t)$ has not yet been established, but it does appear to be universal.

(Cywinski, Campbell and Rainford)

Complementarity with Neutrons?

Muon relaxation rate λ, can be related to the neutron linewidth via the expression

$$\lambda = \frac{BT}{N} \sum_q \frac{\chi(q)}{\Gamma(q)}$$

Inelastic neutron scattering has shown $Y(Mn_{0.9}Al_{0.2})_2$ to be an unusual spin glass with a wide excitation spectrum above T_g. The inelastic linewidth, $\Gamma(q)$ is relatively q-independent, but varies with temperature according to the Arrenhius Law $\Gamma(T) = \Gamma_0 \exp(-E_a/kT)$ where $E_a/k = 278.4K$. In addition

$$\frac{1}{N} \sum_q \chi(q) = \chi_L$$

where χ_L is the local susceptibility, found from INS to be Curie-Weiss like, $\chi_L = C/(T+\theta)$ with $\theta = 93K$. We therefore have

$$\lambda(T) = \frac{T}{(T+\theta)\exp(-E_a/kT)}$$

This form for λ provides a remarkably precise description of the experimentally determined temperature dependence for $Y(Mn_{0.9}Al_{0.1})Mn_2$:

The μSR data points shown were all collected in a twelve hour period. One INS spectrum at a single temperature can be collected in the same time.
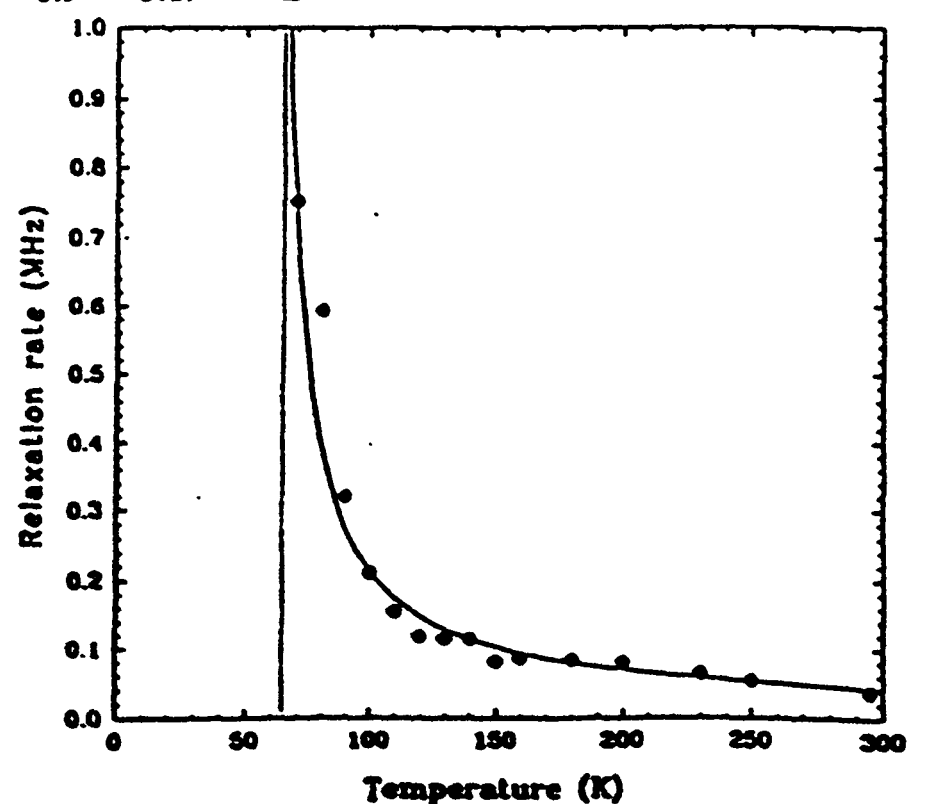
THE ISIS PULSED MUON FACILITY

G H EATON

ABSTRACT

An introductory course is given in the methods whereby muon sources are generated at high intensity intermediate energy proton accelerators. Particular emphasis is placed on the pulsed muon facility at ISIS and its unique properties compared with the continuous sources at the PSI and TRIUMF meson factories.

1)   Production of Low Energy Polarized Muon Sources

All muon facilities rely upon the production of π mesons as the parents of the muons and hence require proton accelerators of an energy well beyond the energy threshold for single pion production in the typical reactions given below.

$$p + p \rightarrow p + n + \pi^+$$
$$\rightarrow p + p + \pi^0$$

$$p + n \rightarrow p + n + \pi^0$$
$$p + p + \pi^-$$
$$n + n + \pi^+$$
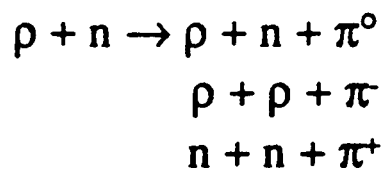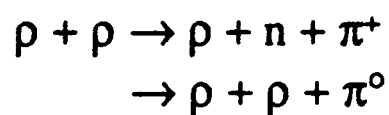
The energy threshold for these reactions is around 180 MeV proton kinetic energy but sizeable production cross sections are achieved only at energies well beyond this threshold, typically above 500 MeV, the energy of the meson factory at TRIUMF. PSI produces 590 MeV protons, while ISIS has an extraction energy of 800 MeV. Increasing the kinetic energy from 500 MeV to 800 MeV has little effect on the production cross sections for low energy pions, but enhances the production of higher momentum pions and allows the onset of double pion production.

The pions are produced from targets inserted into the proton beam. Those targets most commonly used are carbon or beryllium of low Z, to maximise pion production while minimising multiple scattering of the proton beam itself.

The charged pion mass is 139.56 MeV in contrast to the 0.5 MeV, 938.2 MeV masses for the electron and proton respectively. The pion is short lived with a lifetime of 26.03 ns and decays via the following reaction.

$$\pi^+ \rightarrow \mu^+ + \nu_\mu \qquad\qquad \pi^- \rightarrow \mu^- + \overline{\nu}_\mu$$
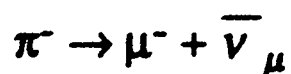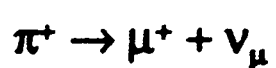
The muon mass (105.65 MeV) is such that in the two body decays above, which occur at rest i.e. stopped pion, the muon has a unique energy and momentum (29.79177 MeV/c) arising from the zero neutrino mass and conservation of momentum and energy in the decay process.

Precise measurements of this muon momentum have placed upper limits on the muon neutrino mass which are consistent with zero mass.

The pion itself has zero spin or angular momentum, so that as a consequence of the negative helicity (longitudinal spin) of the neutrino in pion decay, the emergent muons in any particular direction must be fully longitudinally polarized. This fact forms the basis of the production of polarized muons in a so called 'surface' or 'Arizona' muon channel where the parent pions are at rest before decay. Those pions which stop in the actual target in which they were produced, provide muons which are close to the full muon momentum in the decay process only if they stop at or close to the surface of the target facing the muon channel, hence the expression 'surface' muon beam. By this means very intense beams of fully polarized positive muons may readily be produced. Negative pions on the other hand upon stopping in the target are rapidly captured from their orbits around the target nuclei, producing pionic disintegration of the nucleus concerned. Because of this a surface muon beam is not capable of producing polarized surface muons of negative charge.

To produce polarized negative muons or polarized positive muons of momenta greater than the surface momentum, a different type of muon channel has to be constructed. The so called 'decay' channel uses pions not at rest but at some selected momentum as they escape the production target. These pions are collected and momentum analysed before being introduced into a long superconducting solenoid, in which a fraction decay into muons. The decay length for pions of momentum P_π (MeV/c) is given by:

$$\lambda_\pi = 0.055 \times P_\pi \ (m)$$

Hence to collect a reasonable decay fraction, solenoids of length up to 6m long are required for typical input pion momenta of 100 MeV/c. In typical fields of 5T commonly used, all the decay muons are captured in tight spirals within the solenoid and are prevented from being lost at the internal bore of the solenoid.

The exit aperture of the solenoid acts a source of muons, either positive or negative depending on the change sign of the input pions. The subsequent muon extraction system collects and transports those muons whose momentum corresponds either to forward or backward decays in the pion rest mass. By this method a high muon polarization of (~80%) can be achieved.

2)   Transport of Muons to the Experiment

Muons unlike neutrons are charged particles and hence can be deflected in magnetic and electric fields. Magnetic fields in a typical muon beam line are generated and used in quadrupole magnets which are used for focusing the muon beam, and in bending magnets which are used to select a particular momentum for the transmitted muons. Electrostatic

fields are used in special devices to deflect the muons appropriately or in combination with magnetic fields

Non relativistically the force on a particle of mass m, velocity v, change e, passing through a magnetic field B perpendicular to its path is given by

Force = Bev in a direction perpendicular to B and v

The particle excecutes a circular path of radius R in the field such that

$$Bev = \frac{mv^2}{R}$$

so that the deflection angle in passing

through the field ϕ is proportioned to $\dfrac{Be}{mv}$ i.e. proportional to $\dfrac{1}{P}$

The magnetic fields required in quadrupoles and bending magnets are proportional to the momentum of the particles concerned.

Similar considerations for electrostatic deflections show that these are proportional to $\rho\beta$ of the particles concerned. In general deflecting devices based upon electrostatic fields are suitable only for low particle momenta and velocities, higher momentum particles are more efficiently deflected using magnetic fields.

The primary task of a muon beamline is to collect and transmit as many of the muons produced in the target as is possible within the typical aperture constrants of the various elements in the beam-line. A quadrupole magnet if used as a horizontally focusing device is of necessity vertically defocusing and so these must be used in pairs (quadrupole doublet) or in three (triplet) to produce net focusing in both directions.

In a pulsed beam of muons such as the ISIS facility, special care must be taken to remove contaminant particles other than muons in the beam. These are principally positrons in a positive surface muon beam and because their velocity is close to the velocity of light, in contrast to $\beta = 0.24c$ for surface muons, they are readily removable using a crossed magnetic field / electric field separator.

3)   The ISIS Muon Facility

3.1   Introduction

The ISIS Facility in general layout is shown in Figure (1). The linear accelerator A injects negatively charged hydrogen ions of 70 MeV into the synchrotron after stripping using an injection scheme known as multi-turn injection. The synchrotron accelerates these protons to 800 MeV, using RF cavities operating at twice the

fundamental harmonic. In this way two proton bunches are accelerated during each machine cycle, so that upon extraction using fast magnetic kickers, these two pulses are directed from the synchrotron B along the extracted proton beam channel to the spallation neutron target C. This target consists of uranium or tantalum plates in which the protons are stopped producing approximately 30 (15) neutrons / proton in the case of uranium and tantalum respectively. These fast MeV neutrons are moderated to low energies in an ensemble of four moderators surrounding the target. Each moderator acts as a source for the neutron beam lines D.

The ISIS muon beam lines are produced from thin graphite targets E located some 20m upstream of the spallation target. The time structure of the proton pulses while of no significance to the thermalized neutron beams, is important in the case of the muon facility, where the muon pulses reflect this time structure (70ns FWHM wide pulses, separation 340ns). The layout of the ISIS experimental hall is shown in Figure (2) showing the respective locations of the neutron beams, the KARMEN neutrino facility and the muon beam line complex.

The muon production targets are shown in the photograph of Figure (3). The thickness of muon targets by 1994 will be variable from 5mm to 10mm in the proton beam direction, limited by the losses to the spallation target (~ 3% for 10 mm target) and the induced fast neutron background to the neutrino detector.

These targets are edge cooled at the base and orientated at 45° to the proton beam such that the south side muon facility views the backward face.

3.2   The ISIS Surface Muon Beam (1987-1993)

This is shown in Figure (4). The surface muons are collected by the quadrupoles Q1, Q2 close to the target after passage through the thin aluminium window separating the vacuum systems of the muon and proton channels. These muons are momentum analysed in the magnet B1 which is set at the same integrated magnetic field as B2. Q3, Q4 and Q5 produce a dispersed focus of the beam in the middle of Q4, near to which is a horizontal collimator used to select the momentum bite of the beam.

Q7, Q8 transmit the muons through the drift space Q7-Q8 in which is situated the cross field electrostatic separator A used to eliminate the positrons in the beam. Also in this section of the beam line is a special electrostatic kicker UPPSET which was used to eliminate the second muon pulse. The beam line is completed by a quadrupole doublet Q8, Q9 which produces a simultaneous horizontal and vertical focus of the muons at the sample position in the μSR spectrometer situated at the end of the beam line.

The beam envelopes for this early muon facility are shown in figure (5), illustrating how the quadrupoles are used to transmit the muons with minimal loss from the muon production target to the experimental apparatus.

4

3.3   Positron Elimination in the ISIS Muon Beam

The muon beam line is set at a surface muon momentum of 26.5 MeV/c transmitting all positively charged particles of this momentum.

Besides the surface muons themselves, positrons exist in the beam line some of which arise from the decay of π° produced in the target and the subsequent materialization of electron positron pairs in the reactions:

$$\pi^{\circ} \rightarrow \gamma\gamma \qquad \gamma \rightarrow e^+ e^-$$

Because the π° lifetime is short (0.83×10^{-16} secs), these positrons are prompt and reflect precisely the time structure of the proton pulses. If all of the positrons were prompt, they would not pose such a serious problem in a pulsed muon facility, however, a sizeable fraction ($\sim 50\%$) of the contaminant positrons arise from the decay of muons in the target with a decay time constant of 2.2 μsecs.

The momentum spectrum of positrons from muon decay is shown in the Michel spectrum of Figure (6) where it is clearly evident that many e^+ are produced in this decay at a momentum of 26.5 MeV/c and which we therefore transmitted by the beam line. These must be eliminated in such a beam as they simulate exactly the muon decays in the sample.

This can be done with a cross field electrostatic separator. This is a device which in the ISIS muon beam consists of a vertical electric field between horizontally disposed electrodes, and a horizontal magnetic field generated by anxiliary coils. In such a device, particles of momentum p (GeV/c) and velocity β(V/c) are deviated vertically by an angle $\Delta y'$ (mr) given by the expression.

$$\Delta y' \, (\text{mr}) = \frac{\ell}{p}\left[\frac{\varepsilon_0}{\beta} - 300\,B\right]$$

ℓ length in m

ε_0 Electric field gradient in Mv/m

B field in T

For particles such as surface muons ($p = 0.0265$ GeV/c, $\beta=0.24$) it can be arranged that $\Delta y' = 0$ when $\dfrac{\varepsilon_0}{\beta} = 300B$. This being the case the muons are transmitted through the device without deviation. For positrons $\beta = 1$ and a vertical deviation occurs which for 100kv applied to the device, is sufficient to remove them from the beam. This device essentially acts as a velocity selector.

Typical values used at ISIS are 100 kv over the 13 cm gap of the separator cancelled by a magnetic field of 106.9 Gauss. This produces a vertical deviation for positrons of 92mr.

Incidentally this device induces a polarization rotation of the muon given by $\varphi = \dfrac{eB\ell}{\beta\gamma}$

where e is the charge in the muon and $\gamma = 1 / \sqrt{1 - \beta^2}$

For 100kv $\varphi = 6.6°$ at surface momentum pointing upwards from the direction of travel of the muons. Given sufficient electric field gradient and length, $\pi/2$ rotation can be achieved resulting in a transformation of longitudinal polarization to transverse. Such a capability is useful for high transverse field experiments and for full flexibility of the facility. Such $\pi/2$ rotation would require 454 kv generated over two cross field separators each 1.5m long.

3.4 Provision of Single Muon Pulses Using the UPPSET Kicker (1989)

The existence of two muon pulses per acceleration cycle of the ISIS accelerator restricts the magnetic environment in which these muons may be stopped in a sample and hence the research which can be done with these muons.

In an applied transverse magnetic field of 110 Gauss, 330 Gauss etc., it is possible to rotate the polarization of the first muon pulse by 180°, 540° etc. in the time it takes for the second pulse to arrive, resulting in an essentially unpolarized muon ensemble. This being the case no useful μSR measurements can be made at these applied magnetic fields. This is illustrated by Figure (7) which shows the measured μSR transverse asymmetry against applied magnetic field, where clear 'holes' in the μSR sensitivity can be seen at these fields.

In order to overcome this problem, a fast electrostatic (ε field) kicker was installed in the beam line in 1989, to suppress the second muon pulse. This kicker shown in Figure (8) consists of closely spaced horizontal electrodes, alternately grounded across which an applied HV of -15kv is generated between the two muon pulses. Muons in the second pulse are kicked vertically by ± 50mr such that they impinge upon the closely stacked foils of a Soller collimator downstream of the kicker. In this way these muons are prevented from reaching the experiment. Figure 7 shows how this capability removes the inhibiting features of the double pulse structure with a modest applied voltage of 12kv.

Such operation with single pulses throws away 50% of the available muons. The principle of this method was extended in 1993 with the creation of the European Muon Facility at ISIS, where ε field kicking was used to distribute single muon pulses at 50Hz simultaneously to three experimental areas.

6

3.5 The European Muon Facility at ISIS (1993)

The ISIS muon facility as constructed in 1987 delivered muons to a single experimental port only. Beam time requests for this single port exceeded the available time by typically a factor of three. Combining this with the general preference of experimenters for single pulse operation, motivated RAL to propose the EC upgrade to this facility. The upgraded facility was designed to solve both problems by incorporating a fast E field kicker to divide and distribute the two muon pulses simultaneously to three experimental ports each operating with single muon pulses at 50Hz. This is done with the E field kicker geometry shown in Figure 9 together with the similar geometry of the UPPSET device.

The EC kicker incorporates three vertical electrodes which in contrast to the UPPSET device, are widely spaced (6 cm gap).

HV of 32kv is applied to the central electrode during the passage of the first muon pulse. The two outer electrodes are grounded. The first pulse of muons experiences a reversed direction of the E field on either side of the central electrode, such that a horizontal deviation to the right / left of 66.3 mr is achieved. This muon pulse is therefore equally divided and directed to its respective septum magnet SEPA and SEPC shown in Figure (10), and hence to its experimental area DEVA or EMU.

The HV on the central electrode is ramped to ground before the arrival of the second pulse, which therefore proceeds undeviated to the straight beam area MUSR. In this way the two original muon pulses are divided and distributed to provide three experimental ports with simultaneous single muon pulses at 50Hz.

Figure (11) shows the muons detected in the MUSR (2nd trace) and EMU area (3rd trace) compared with the basic timing pulses (1st trace) derived from an in-beam cerenkov counter. Trace 4 shows the high voltage waveform on the kicker. These traces verify the expected action of the kicker on the two muon pulses.

3.6 The RIKEN Decay Muon Facility at ISIS (1994)

This decay beam is shown in Figure (12). It is derived from the same muon production target as the EC facility but on the north side of the extracted proton beam. This facility due for completion in late 1994 will ideally complement the south-side surface facility in being able to provide polarized muons of both charge signs in a momentum range from 18MeV/c to 120 MeV/c. For momenta up to 55 MeV/c, a magnetic kicker situated immediately downstream of the first extraction quadrupole triplet will separate the muon pulses simultaneously into two experimental areas, one of which will be provided with a switchyard magnet. This allows the choice of distributing this single pulse to one of two areas, providing three areas in total.

For momenta greater than 55 MeV/c, a pair of small switchyard magnets on either side of the magnetic kicker will direct both muon pulses to a single experimental port of choice. This facility will predominantly be used for research with negative muons studying muon catalysis processes and negative μSR.

Upon completion ISIS will provide five experiments simultaneously with single muon pulses; an experimental capability similar to the established meson factories at PSI and TRIUMF. The ISIS Facility will be the worlds most powerful pulsed muon source for many years and will provide European and Japanese scientists with unrivalled research opportunities.
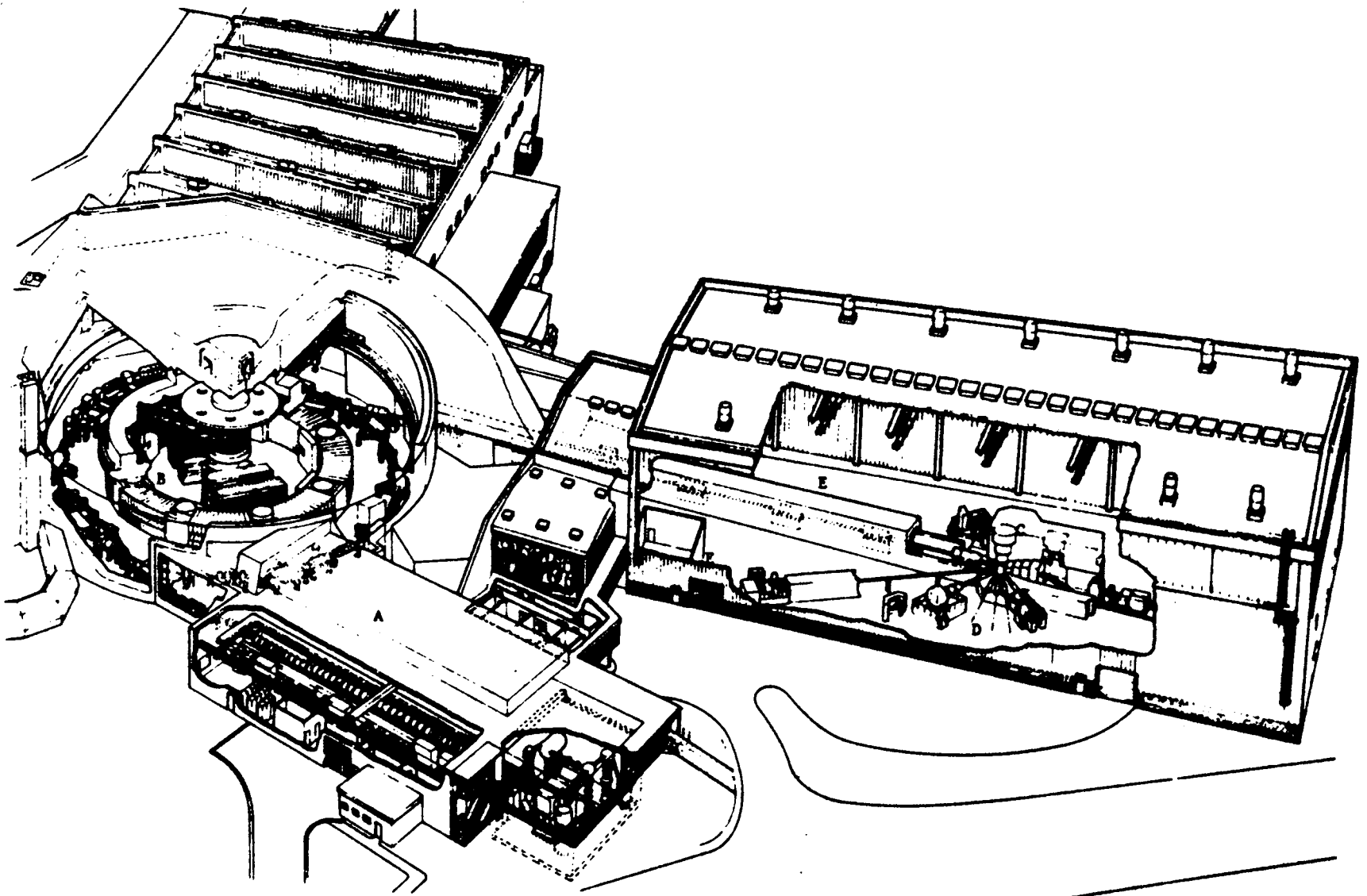
Fig. 1. The Rutherford Appleton Laboratory ISIS facility. The principal components shown are: (A) the linac injector, (B) the synchrotron, (C) the spallation neutron source, (D) neutron beam lines, (E) general location of present and future muon beams.
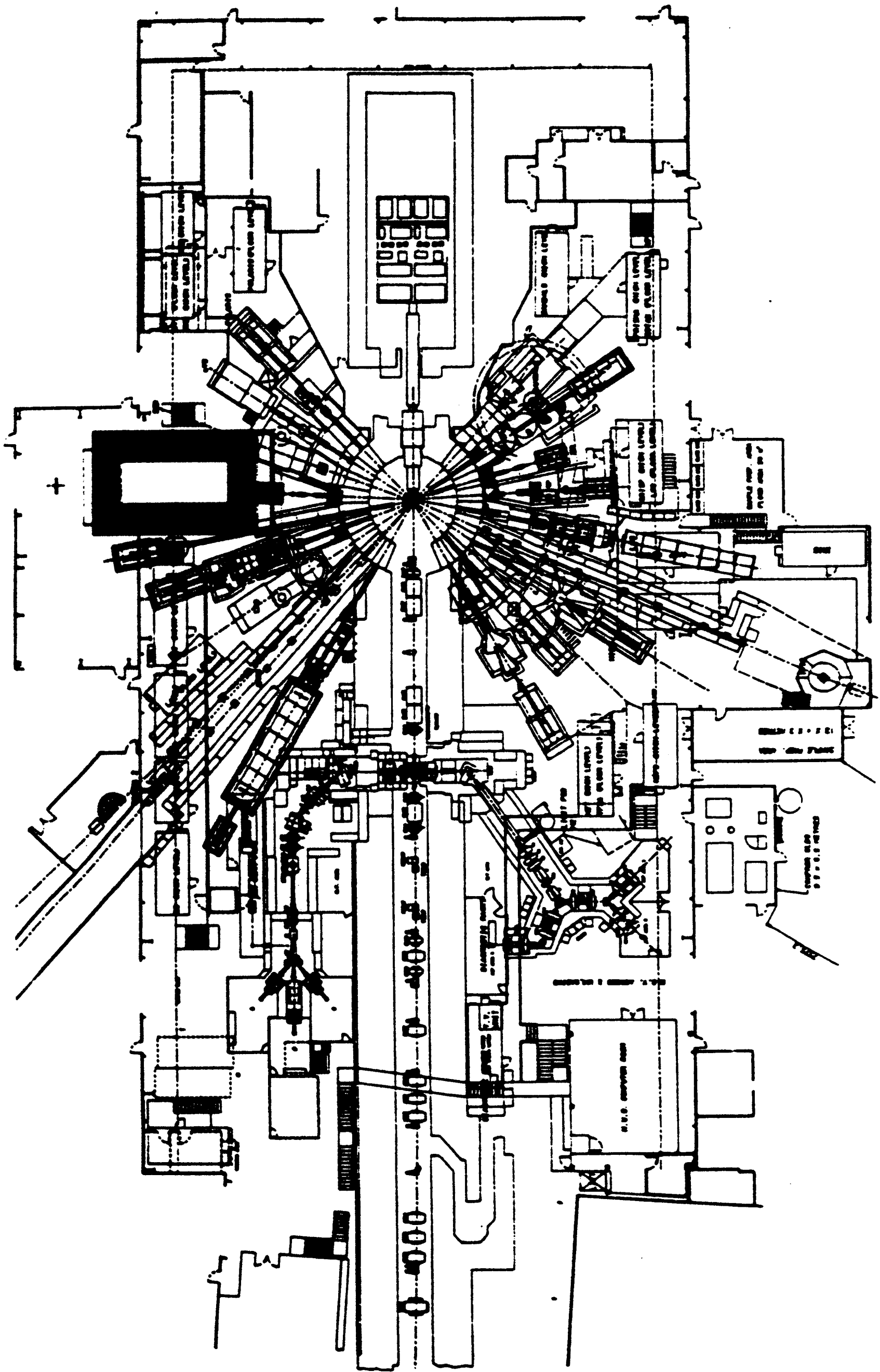
Fig.2. Plan view of the ISIS experimental hall, showing the neutron beams fanning out from the spallation target. The Karmen neutrino facility is shown at the top of the drawing, while the muon facilities (EC and RIKEN) are produced from a separate muon production target in the extracted proton beam some 20m upstream from the spallation target.
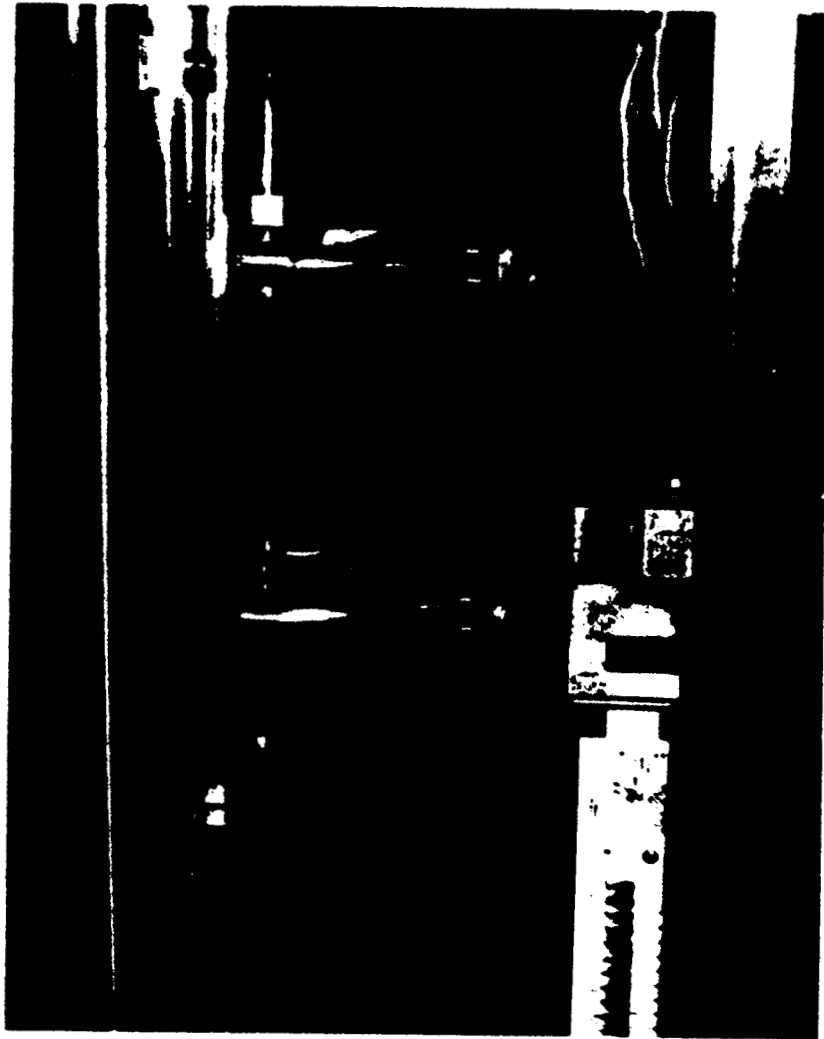
Fig.3. Photograph of the thin graphite targets used to produce muons. These targets are water-cooled at one edge. Also shown is a profile monitor for the extracted proton beam.
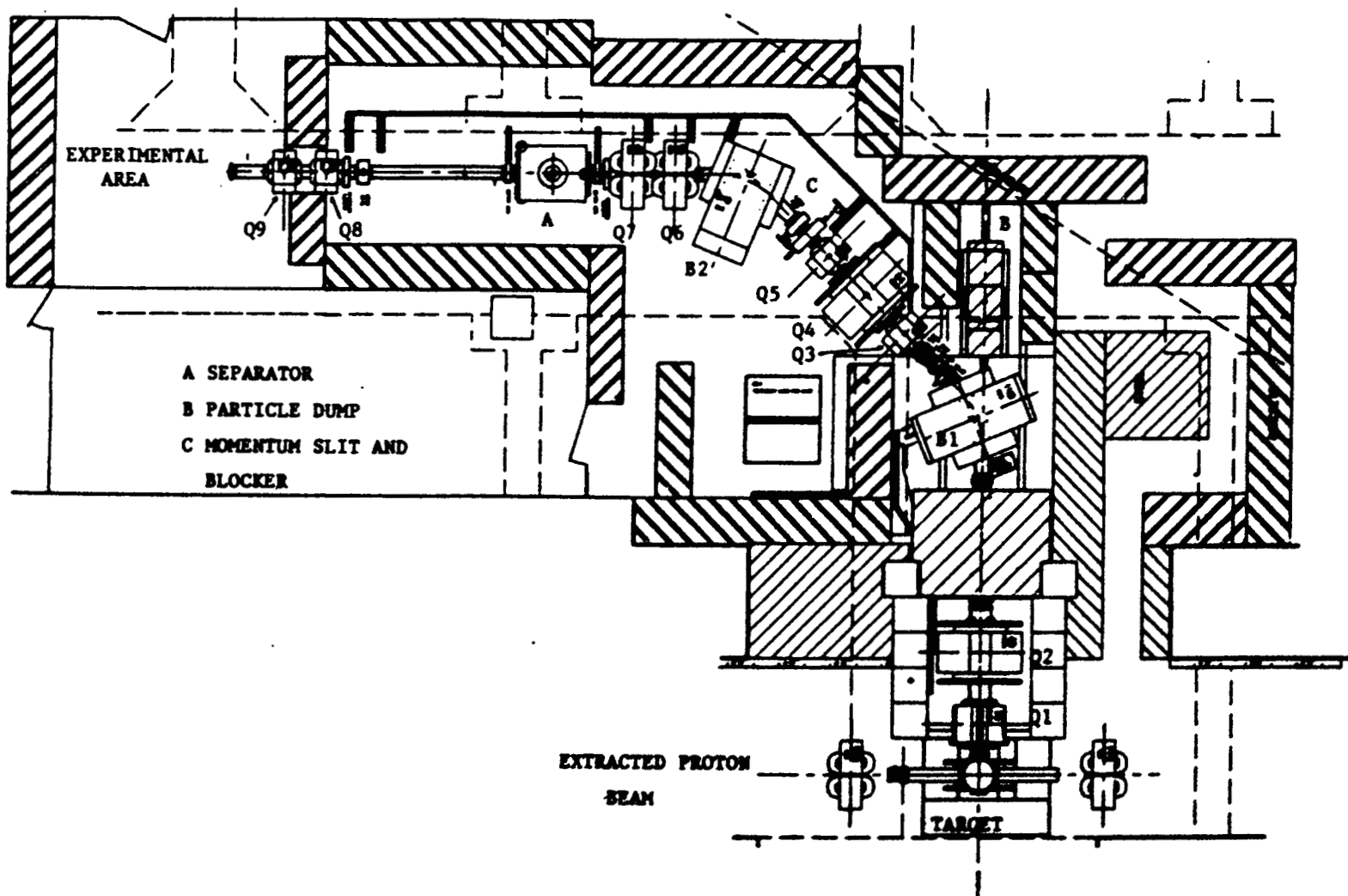
Fig. 4 Layout of the ISIS pulsed muon beam. Muons are produced in thin graphite targets located in the extracted proton beam and collected at a central production angle of 90°. A dispersed focus is produced in the centre of the Q4 quadrupole. Horizontal achromaticity is achieved after the second bending magnet. Positron separation is obtained using the 1 m CERN cross-field separator.
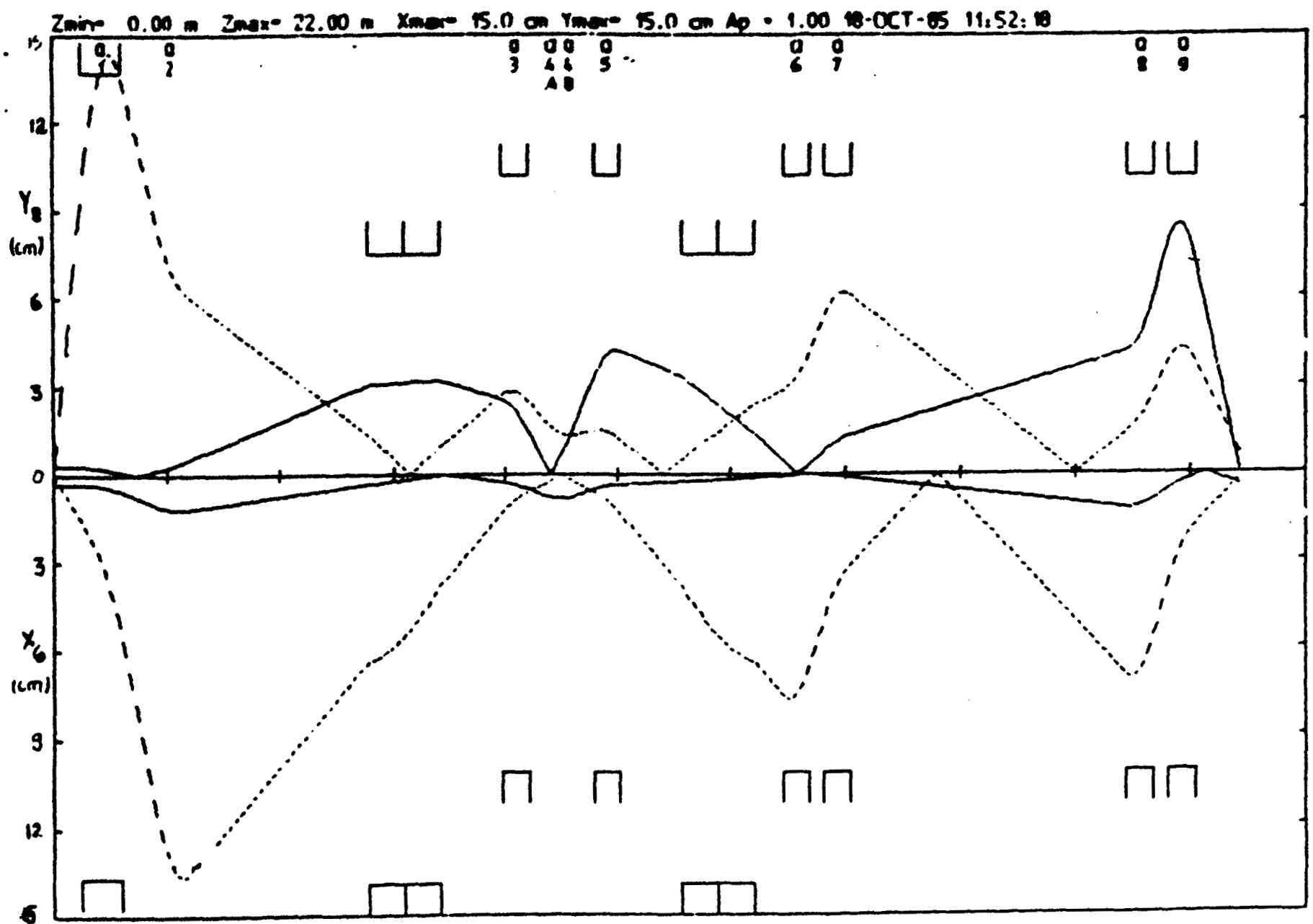
Figure (5). Principal Trajectories from TRANSPORT for the New Version of the Muon Beam. Trajectories shown are from the centre of the Production Target with Maximal Divergence Y' and X', and from the Extremes of the Target with zero Divergence.
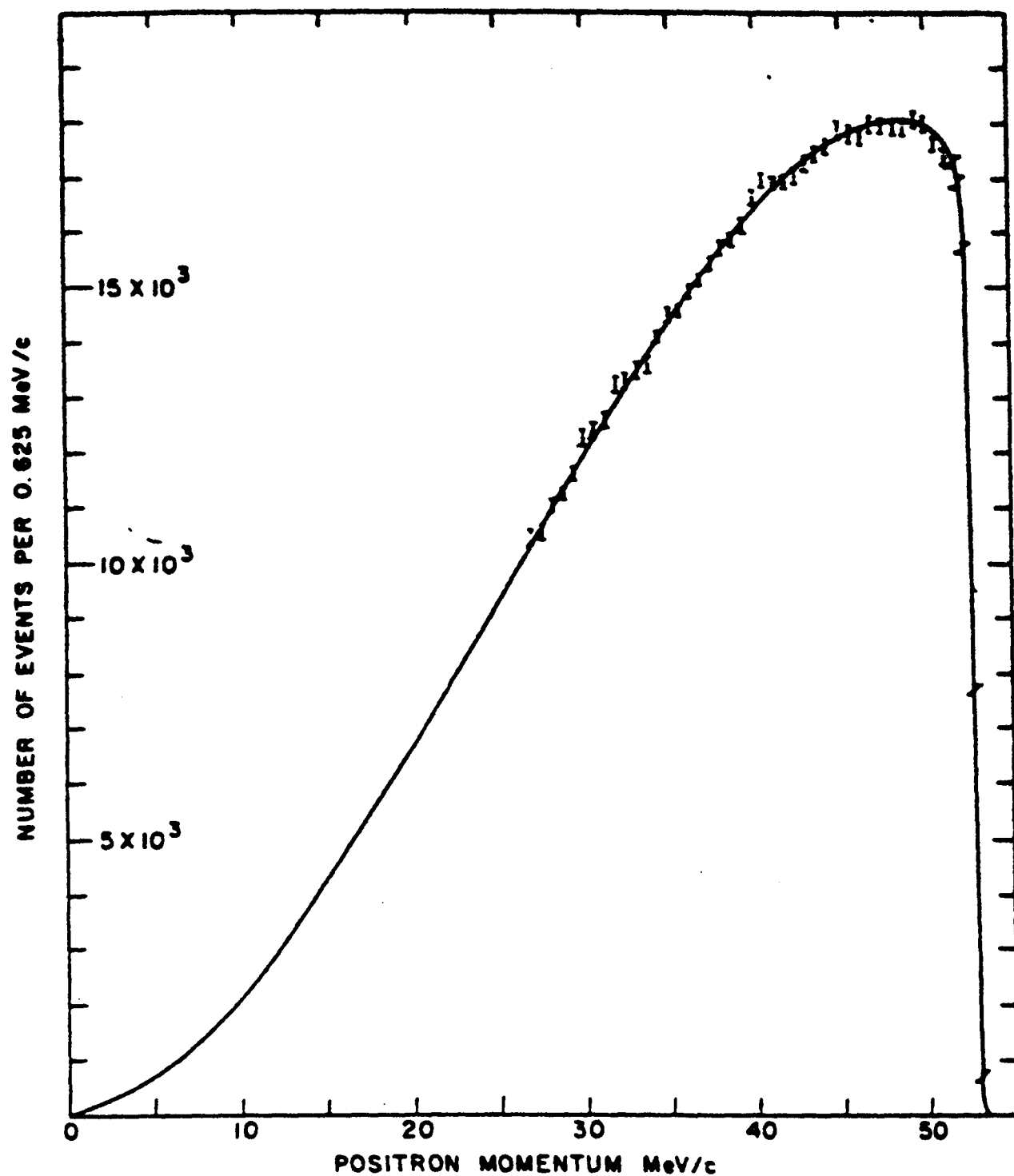
Fig.6. Michel momentum spectrum of positrons from muon decay at rest.
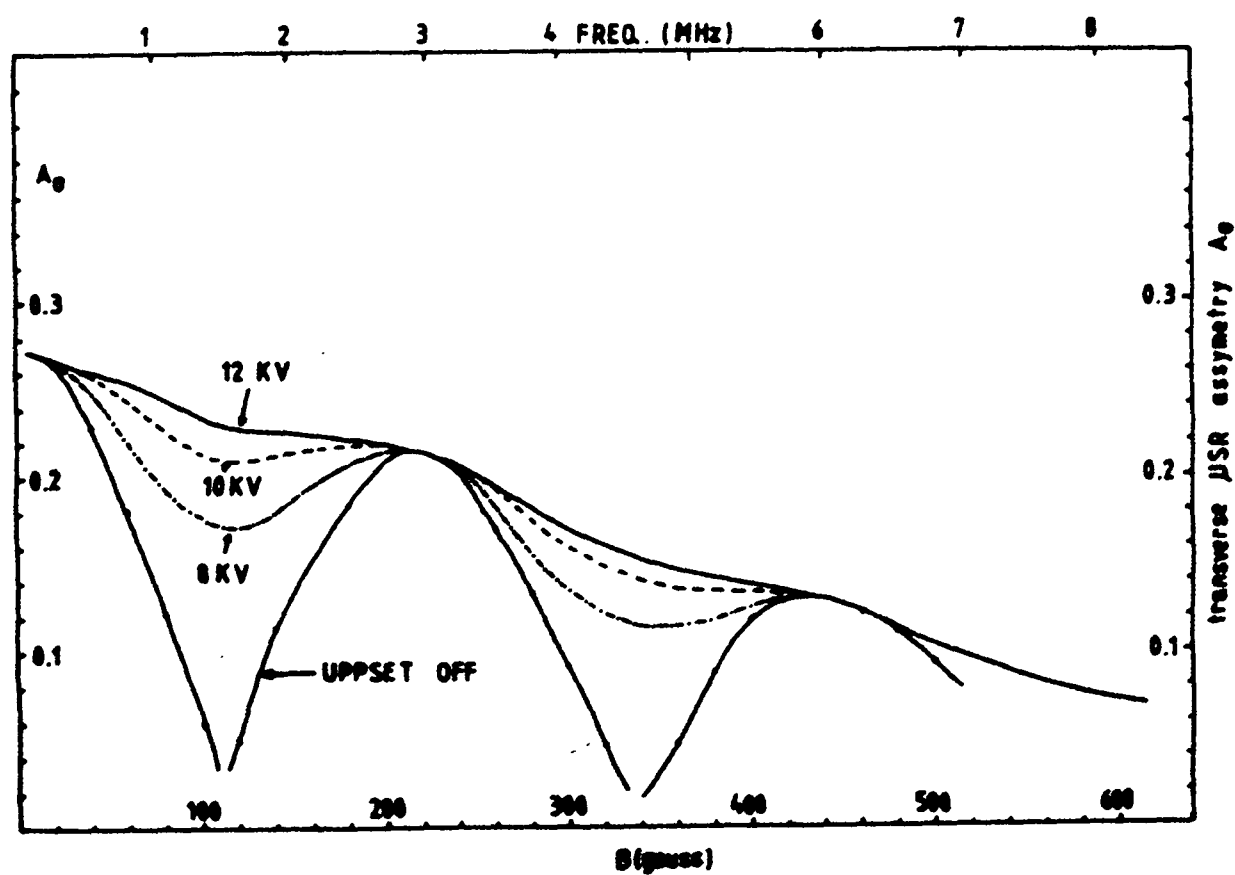
Fig. 7. Dependence of the measured transverse μSR asymmetry from an aluminium sample on applied magnetic field for various operating conditions of the UPPSET device. With the UPPSET device off, the measured response function is a series of peaks with intervening minima close to zero asymmetry. These "holes" in the response function are gradually filled in as the UPPSET voltage is raised in steps to the design voltage of 12 kV.
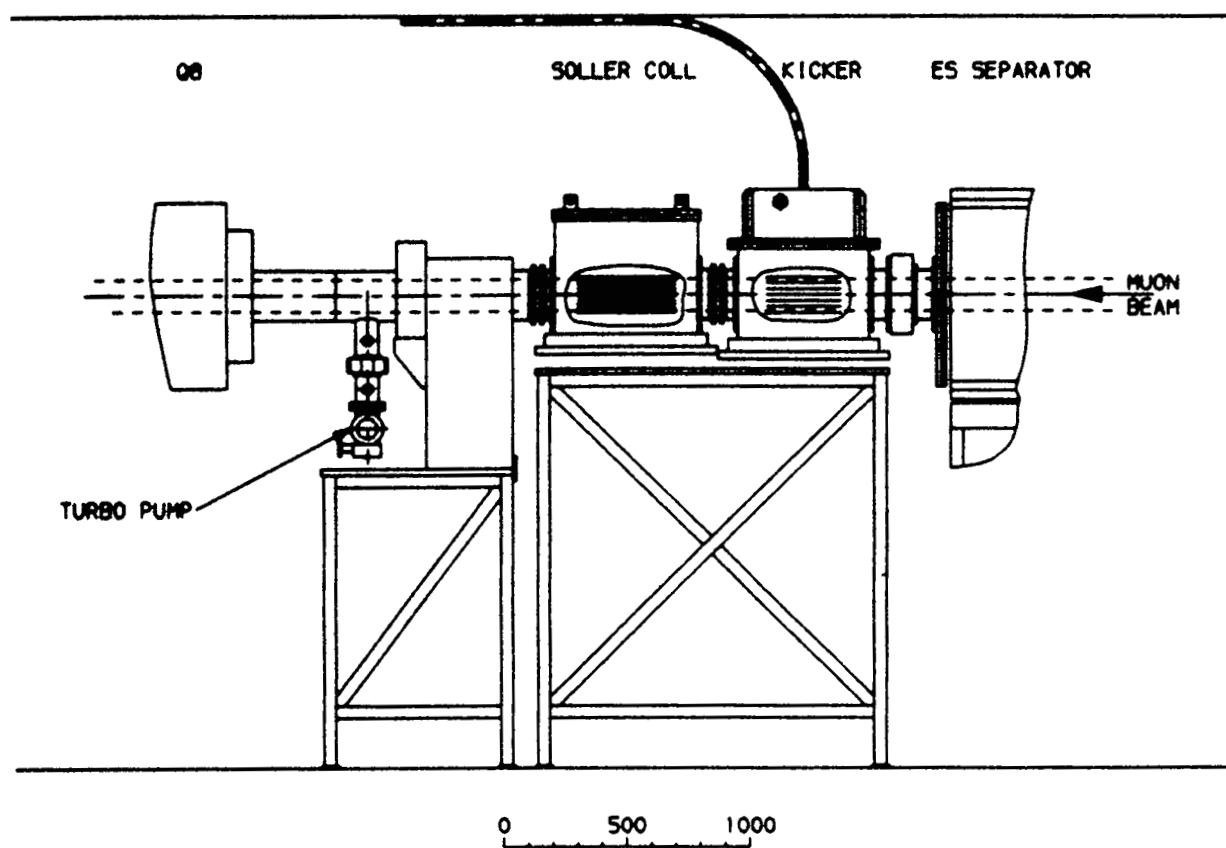
Fig. 8. Side view of the UPPSET system located in the drift space between the cross-field separator and the Q8 quadrupole. The electrostatic kicker is shown relative to the vertical divergence limiting Soller collimator.

UPPSET KICKER
VERTICAL CROSS SECTION

$\mathcal{E}{\sim}1MV/m$
RISE TIME
100ns

300mm

12mm

0-15kV

0-15kV

0-15kV

0-15kV

26.5 MeV/c
μ^+

EC KICKER VOLTAGE

+32kV

UPPSET VOLTAGE

+15kV

muon pulse   #1   #2   muon pulse

100ns   230ns   100ns

EC KICKER
HORIZONTAL CROSS SECTION

700mm

60mm

$\mathcal{E}$

+35kV

60mm

$\mathcal{E}$

26.5 MeV/c
μ^+
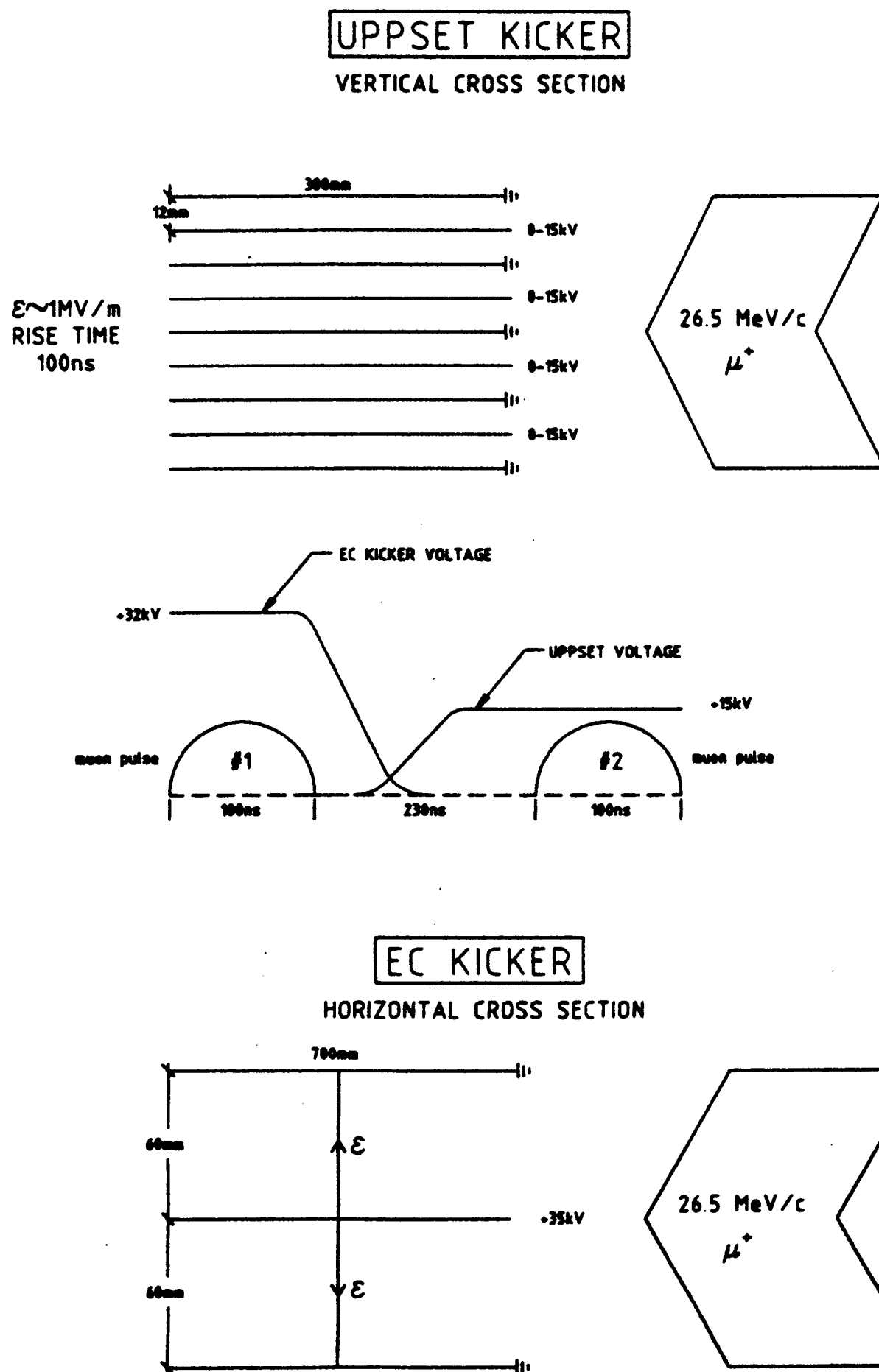
Fig 9. A comparison between the geometrical layout and voltage waveforms of the UPPSET and CEC E-field kickers shown relative to the incoming muons and the timing of the two muon pulses. The UPPSET voltage (0-15 kV) is shown inverted in the diagram.

RUTHERFORD APPLETON LABORATORY

© SERC 1992
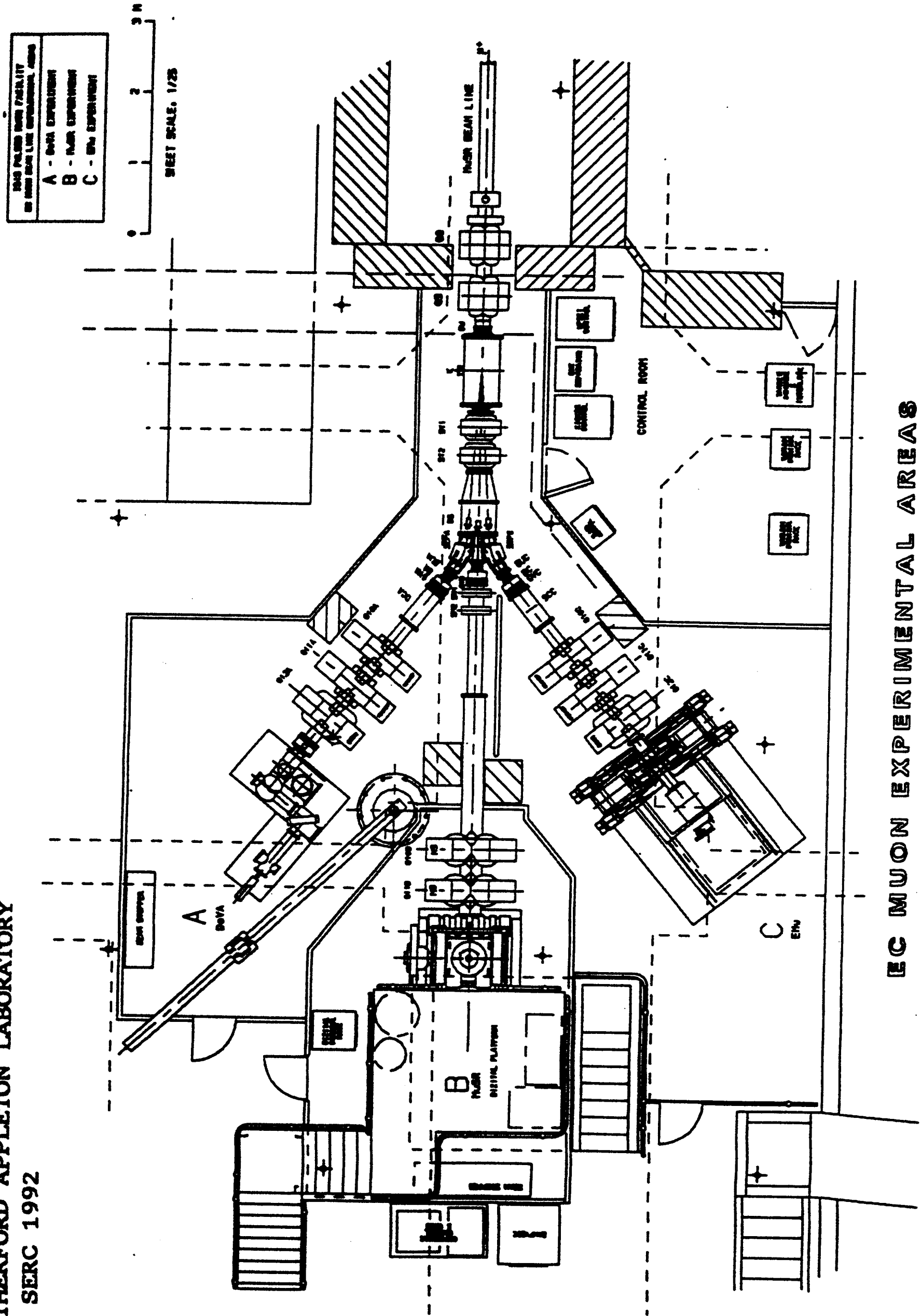
EC MUON EXPERIMENTAL AREAS

Fig.10. Layout of the EC funded upgrade of the ISIS muon facility showing the locations of the fast E-field kicker K, the two septum magnets SEPA and SEPC and the three beamlines.
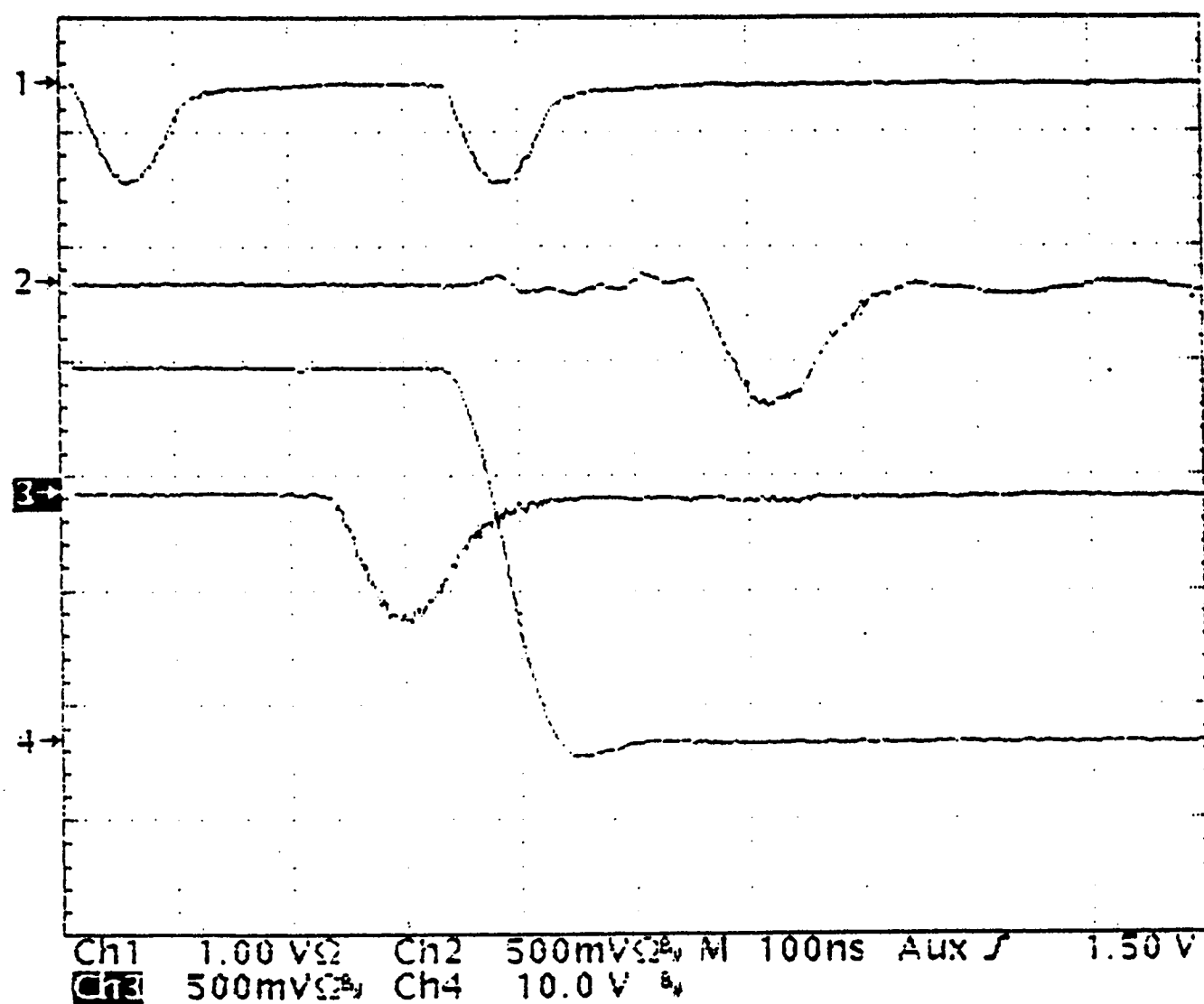
Fig 11. Oscilloscope traces showing the action of the E-field kicker on the double pulses of muons. The top trace shows the Cerenkov pulses revealing the basic time structure of the protons at the production target. The second and forth traces are derived from the MUSR and EMU collimator counters respectively, showing the action of the kicker waveform (third trace) in distributing the two muon pulses to the EMU/DEVA and MUSR beam-lines.
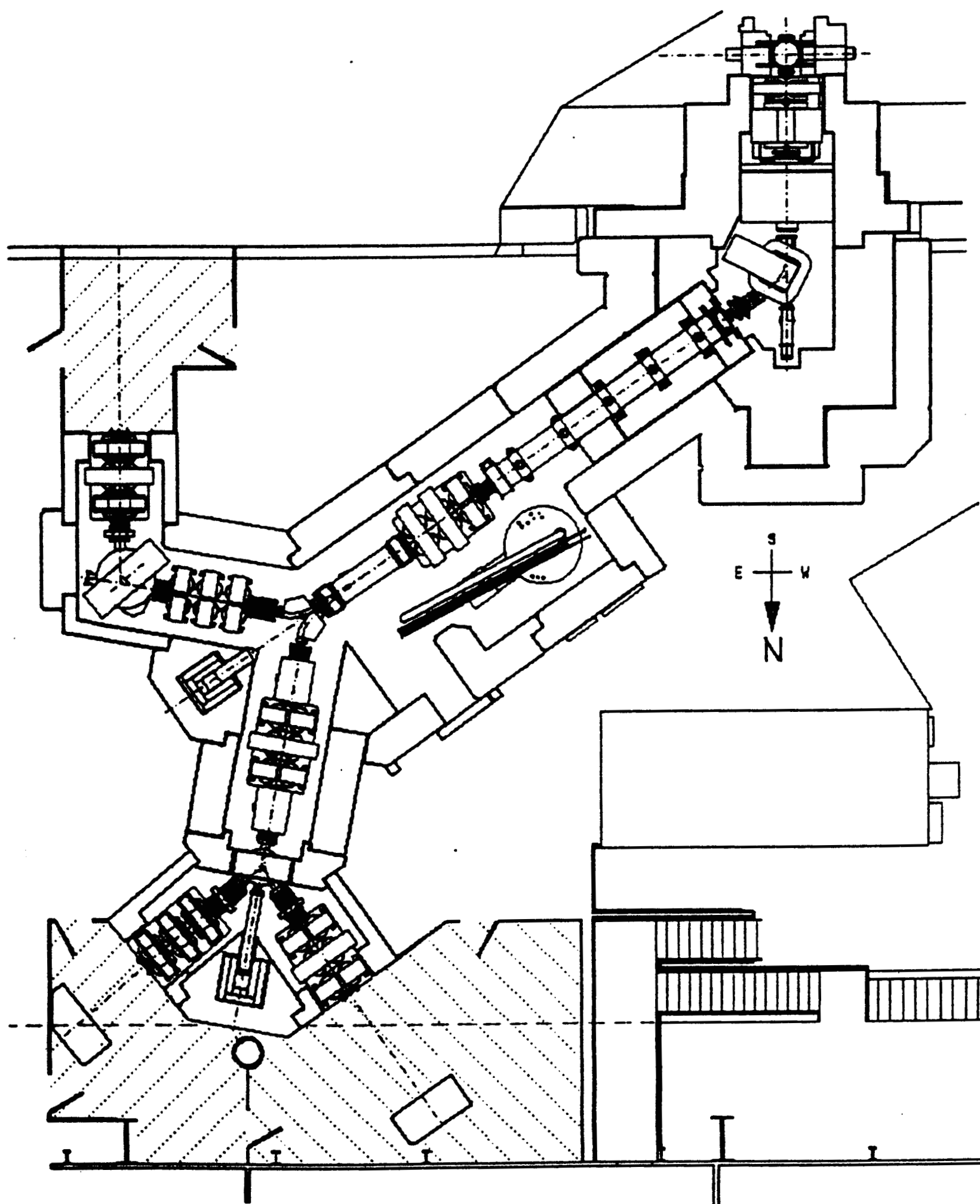
Fig.12. Layout of the RIKEN/RAL decay muon beamline, due for completion
in October 1994.

INTRODUCTION TO THE ISIS MUON SPECTROMETERS

C A Scott
ISIS Pulsed Muon Facility, Rutherford Appleton Laboratory,
Chilton, Oxfordshire, OX11 0QX, UK.

The aim of this talk is to give an introduction to the μSR spectrometers, MuSR and EMU.

1. Fundamentals

The accelerator at ISIS produces protons at an energy of 800 MeV. These protons pass through a graphite slab just before the neutron production target and some pions are produced in the interactions with the carbon nuclei. Positive muons are produced from the decay of the positive pions (lifetime 26 ns)

$$\pi^+ \rightarrow \mu^+ + \nu_\mu \tag{1}$$

The beam-line is designed to accept muons with a particular momentum, "surface muons" as described in Gordon Eaton's talk, and guide them to the sample where they slow down and stop. An important feature of surface muons is that the muons are completely polarised; the muon spin direction is anti-parallel to the muon momentum vector. Muons have a lifetime, τ_μ, of 2197 ns and decay into positrons.

$$\mu^+ \rightarrow e^+ + \bar{\nu}_\mu + \nu_e \tag{2}$$

μSR depends on the fact that the positrons leave the sample with an angular distribution that peaks in the direction of the muon spin at the moment of disintegration (Fig. 1)

$$W(\theta) = 1 + a \cos\theta \tag{3}$$
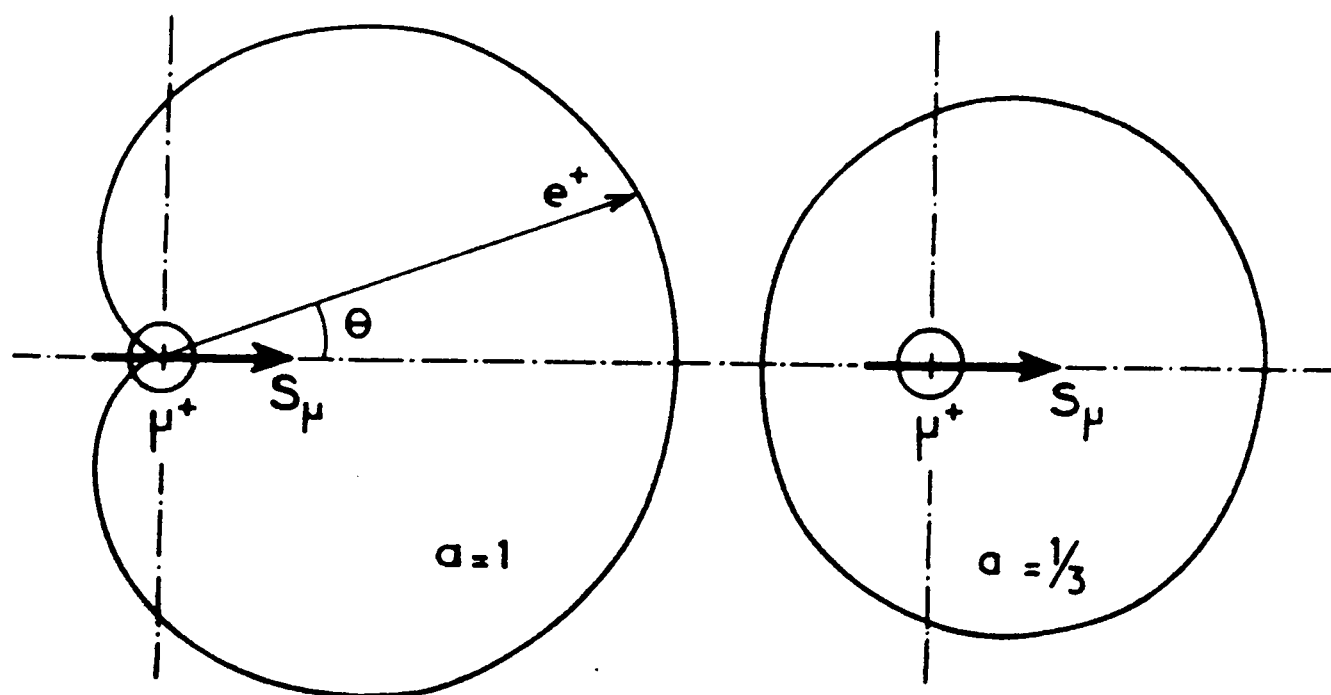
Fig. 1 Angular distribution of positrons for asymmetry parameters 1 and $\frac{1}{3}$

The parameter a characterises the asymmetry of the distribution. Its value depends on the momentum of the emitted positron and has the maximum of 1 only for the small fraction of positrons with the maximum permitted momentum. Averaging over the full spread of positron momenta gives $a = \frac{1}{3}$.

In the absence of any time evolution of the muon polarisation the count rate of positrons in a detector is

$$N(t) = N_0 \exp(-t/\tau_\mu) + B_g \qquad (4)$$

where the first term just represents the the lifetime of the muon and the second term is a background from stray particles in the experimental hall and other unwanted sources. A welcome feature of ISIS is that this term is typically 10^5 times smaller than N_0 and so can usually be neglected. The interest in a μSR experiment lies in the variation of muon polarisation with time so, for instance, in a magnetic field, B, transverse to the initial polarisation the positron rate becomes

$$N(t) = N_0 \exp(-t/\tau_\mu)(1 + a_0 G(t) \cos \omega t) \qquad (5)$$

$$\omega = \gamma B \qquad (6)$$

$G(t)$ describes the decay of the polarisation and ω the angular frequency of the precession (See Bob Cywinski's talk). $\gamma/2\pi$ is $135.5\,\text{MHz/T}$.
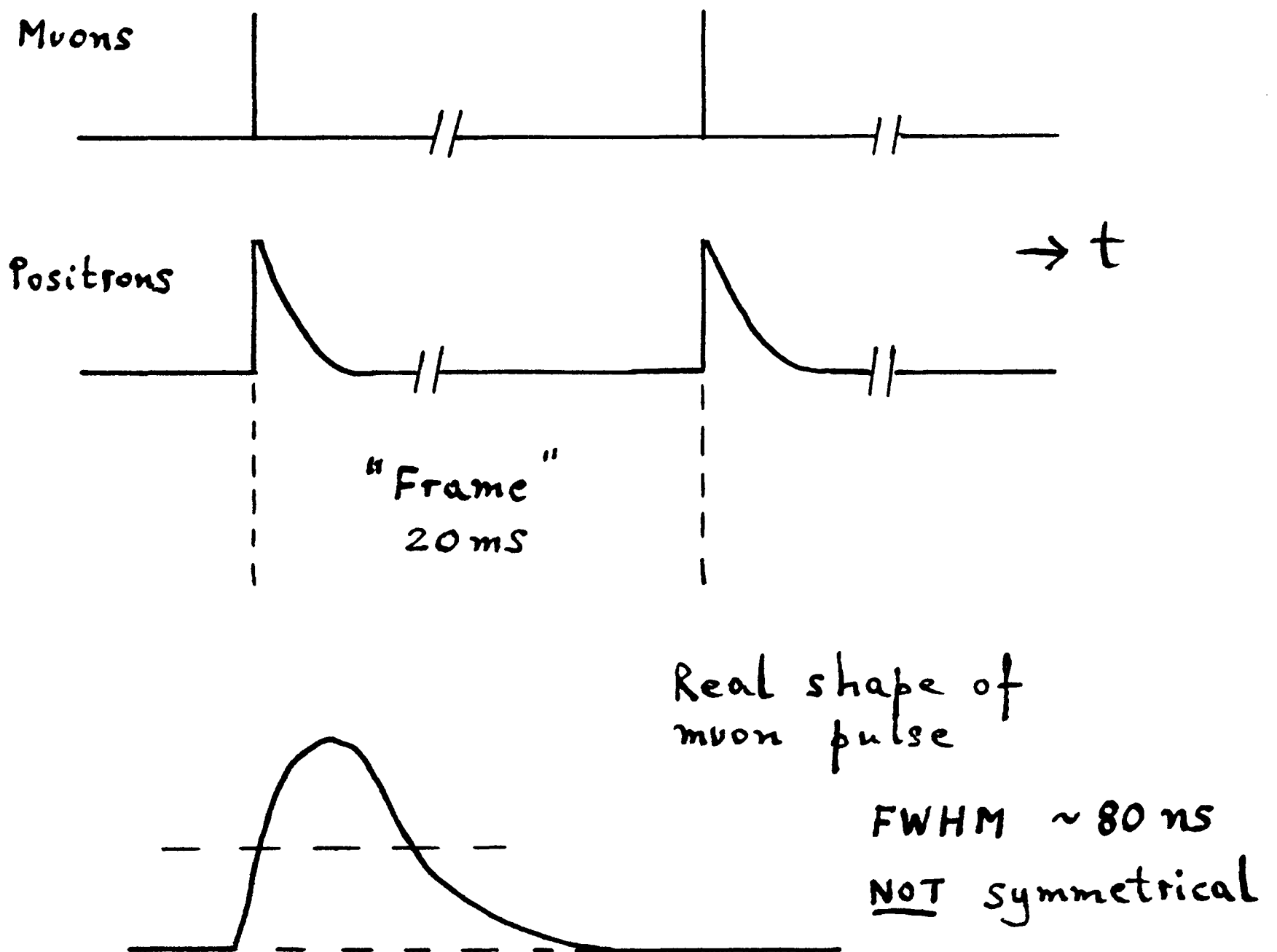
Fig. 2 ISIS muon pulse

2. Frequency Response

At a continuous source of muons t in the above equations is measured from the time of arrival of a muon in the sample to the time at which the decay positron is detected. At ISIS the muons are produced in large numbers in short pulses so it is not practicable to time the arrival of individual muons. Instead the approximation is usually made that an average arrival time near the the centre of the muon pulse can be used as time-zero (Fig. 2). This is adequate if the the time-scale of the evolution of the muon polarisation is long compared to the width of the muon pulse but leads to difficulties in cases where the evolution is rapid. The effect is seen clearly by considering a transverse experiment performed at a succession of magnetic fields. At low fields the frequency is small and the polarisation precesses with the full asymmetry (initial asymmetry $a_0$). As the field increases there is an appreciable phase difference developed between muons from the beginning and end of the pulse and the observed initial asymmetry falls as shown in Fig. 3. The ISIS muon pulse is about 80 ns wide at half height so the asymmetry is down to about 0.2 of the low frequency value by 10 MHz. In practice few people are prepared to work above 5 MHz because of the extra time required to count enough positrons to make a good measurement of the small asymmetry. (The ratio of signal to noise only increases as the square root of the counts in a particle counting experiment).
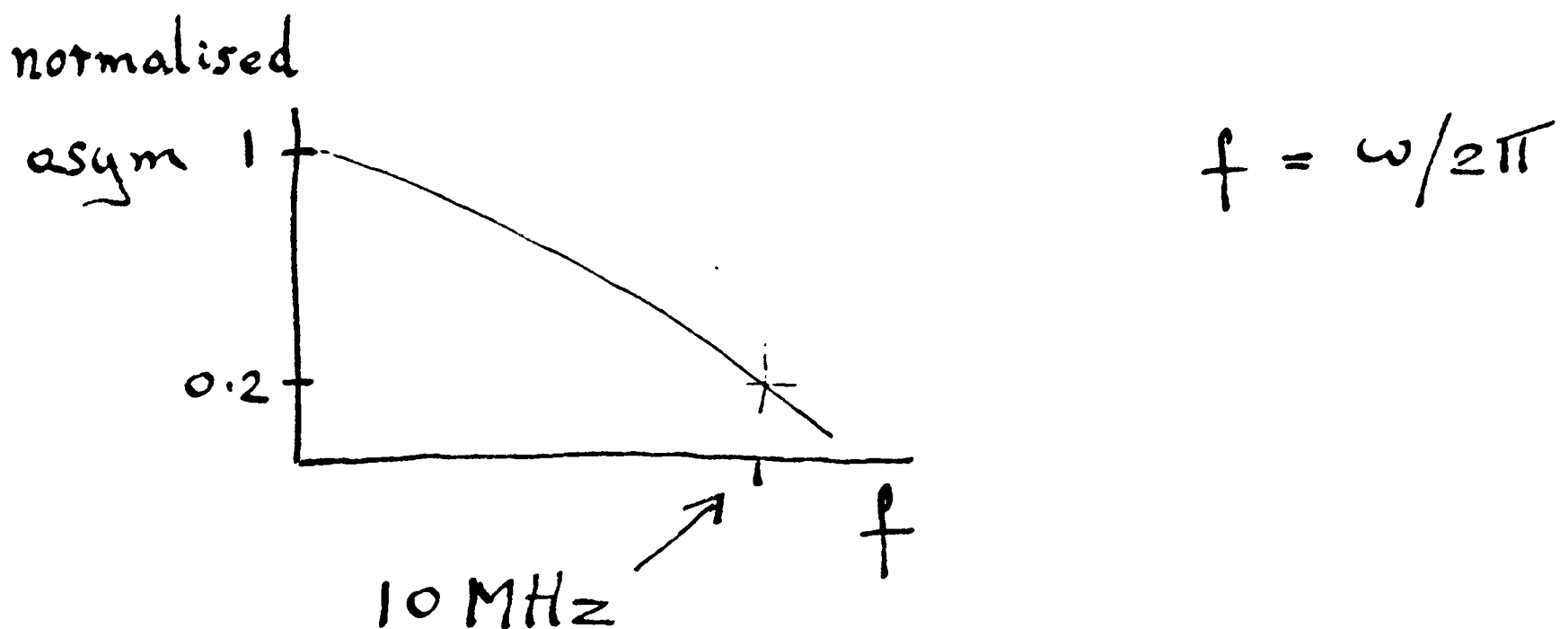
Fig. 3 Frequency response

3. Range Curve

The muons in the beam hit the front surface of the sample at about $0.25c$ and are then slowed by interactions with the material before stopping. Figure 4 shows the variation of stopping density with depth of penetration. The exact form of the curve depends on the material but as a first approximation the position of the peak of the distribution depends only on the density of the material and the muon momentum. This "range" is usually given in the units of mg/cm^2. For MuSR and EMU it is about $110 \, mg/cm^2$. Samples should be appreciably thicker than the calculated range otherwise sufficient extra material has to be placed in front of the sample to bring the peak of the range

curve well inside the sample. The exact value of the range in the various materials is important here so the adjustment is made experimentally by adding thin sheets of metal or plastic in front of the sample to maximise the signal from the sample.
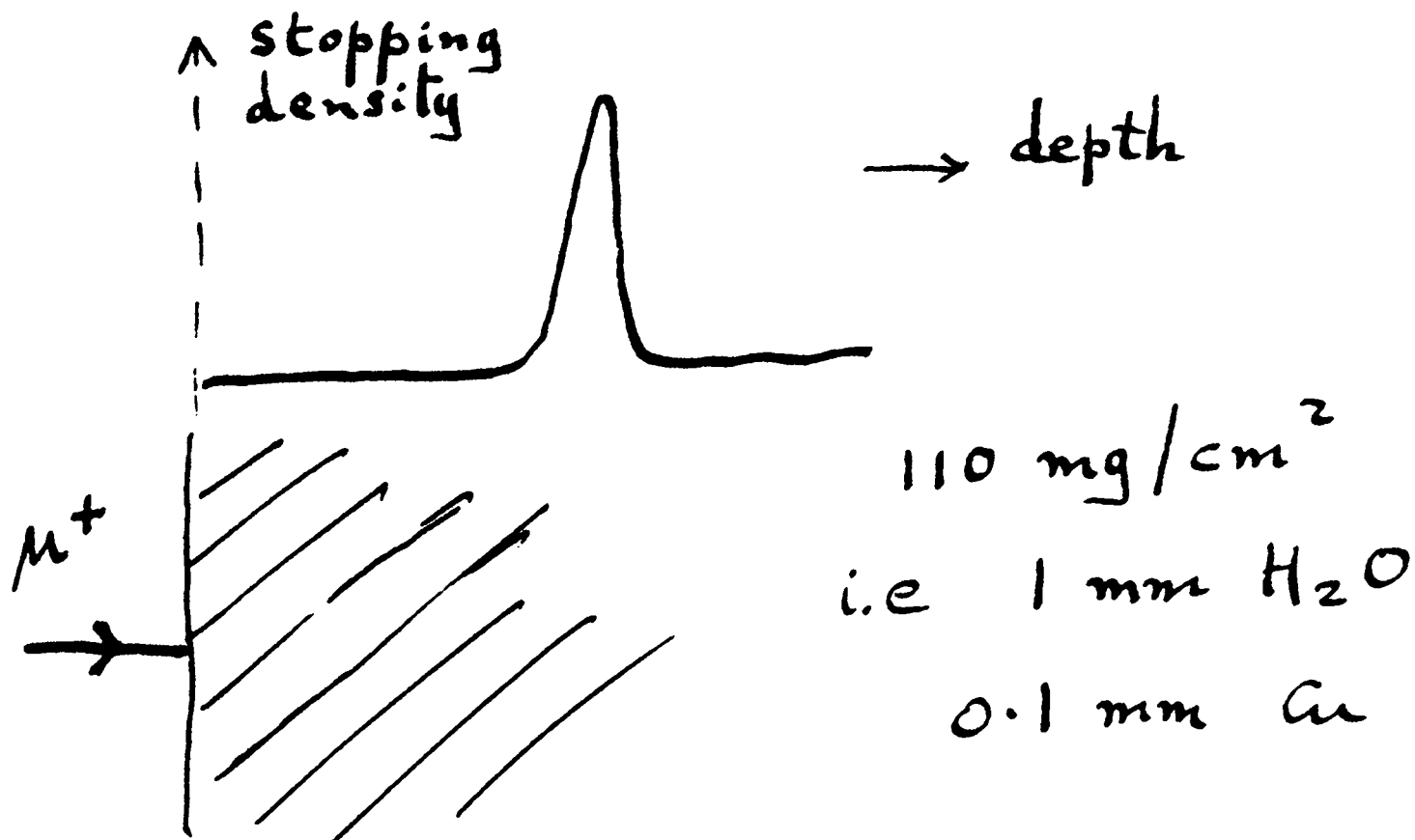
Fig. 4 Range curve

4. Basic Detector

Figure 5 shows a simplified detection chain. The positron from the decay of a muon passes through a plastic scintillator and generates a flash of light. This light is guided to a photomultiplier tube (PMT) where it is converted into a pulse of electrons and greatly amplified. The electrical pulse from the PMT passes to a discriminator which gives a standard logic pulse whenever the pulse is greater than a preset threshold thus discriminating against small (noise) pulses. The time interval between the logic pulse and the trigger pulse marking the arrival of muons in the sample is measured with a time-to-digital converter (TDC). A computer collects these measurements and forms the final histogram of count rate against arrival time of the positrons. Since at ISIS the useful time resolution is limited by the width of the muon pulse a resolution of 16 ns is adequate.
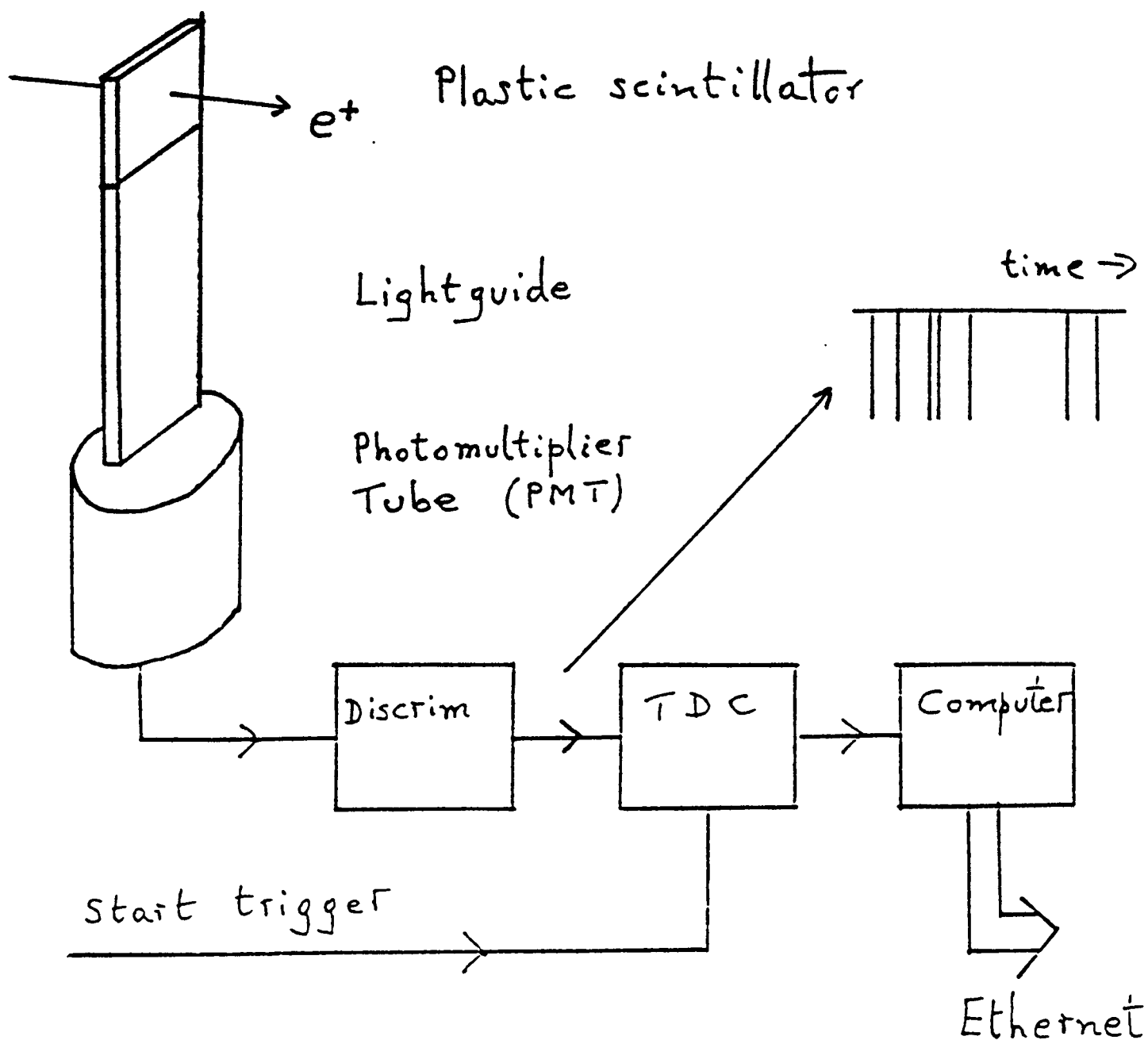
Fig. 5 Basic detector

5. Dead Time

The time at which a muon decays into a positron is completely random so the interval between the pulses from the discriminator (see Fig. 5) varies widely. Because various parts of the detector have limitations on the speed with which they can respond this leads to a failure to record two positrons as separate events if the interval between their arrival in the detector is too small. There is a "dead time" after each event and the observed rate of positron decays will be less than the true rate obtained for a system with negligible dead time. This is a well known problem in particle physics and a detailed treatment can be found in standard textbooks (*e.g Techniques for Nuclear and Particle Physics Experiments*, W R Leo, Springer-Verlag, 1987). The simplest case is when for a true rate, r, there is no response at all for a time τ_d after each pulse but perfect recovery after this interval. In the literature this is called a non-extendable dead time (or alternatively the non-paralysable case). Then the observed rate is:

$$r_{ob} = r/(1 + r\tau_d)$$

$$r = r_{ob}/(1 - r_{ob}\tau_d) \tag{7}$$

There are other models showing dead time effects and in real systems it is often difficult to decide on an appropriate one. However in the MuSR and EMU instruments we find experimentally that the distortion is typically 5% at the beginning of the histogram *i.e* $r_{ob}\tau_d \approx 0.05$ and equation (7) is adequate to correct the data.

6. Longitudinal Calibration

Two basic geometries are used for μSR experiments. In the "transverse" geometry the initial direction of the muon polarisation is at right angles to an applied magnetic field and the positron count rate is given by equation (5). The polarisation precesses in a plane perpendicular to the field and the ideal detector location is symmetrical around the field direction (Fig. 6). In the "longitudinal" geometry the ideal detector arrangement is perpendicular to the initial polarisation (Fig. 7) and to the applied field (if any, this is also the zero field geometry). In the simplest longitudinal arrangement there are just two detectors: "forward" and "backward". The corresponding positron count rates, N_F and N_B, are

$$N_F = N_0 \exp(-t/\tau_\mu)(1 + a_0 G(t))$$
$$\alpha N_B = N_0 \exp(-t/\tau_\mu)(1 - a_0 G(t)) \qquad (8)$$

The parameter α is necessary to take into account the differences in efficiency and solid angle coverage of real detectors. For a pair of perfect detectors placed symmetrically α would be 1.0.

Detectors

$P_\mu(t)$

$P_\mu(o)$

B perpendicular to plane of paper
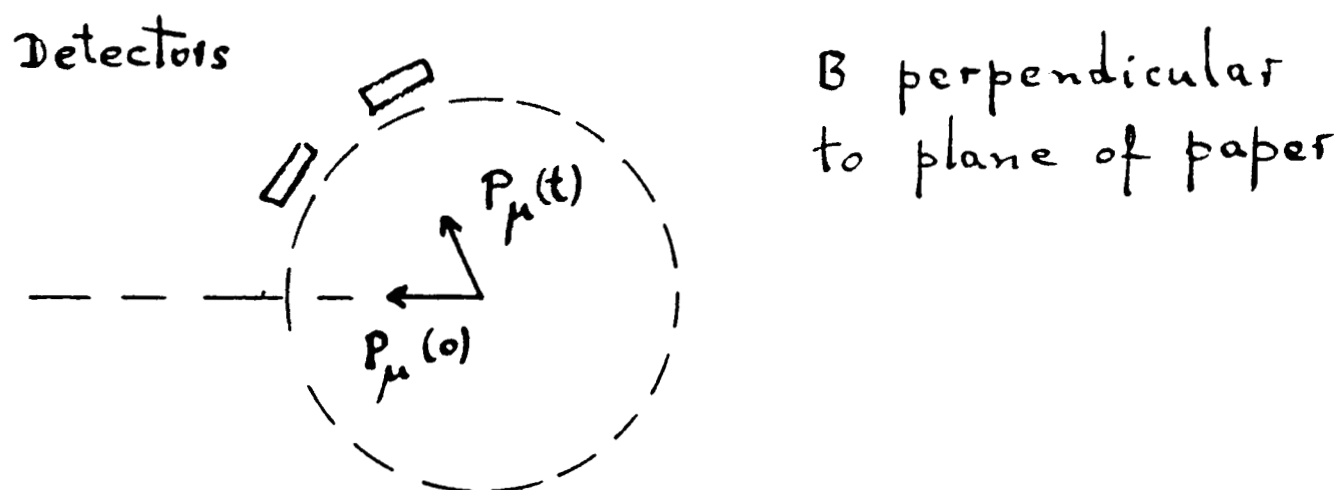
Fig. 6 Basic detector arrangement for transverse measurement

B

$P_\mu(o)$

Forward   Backward
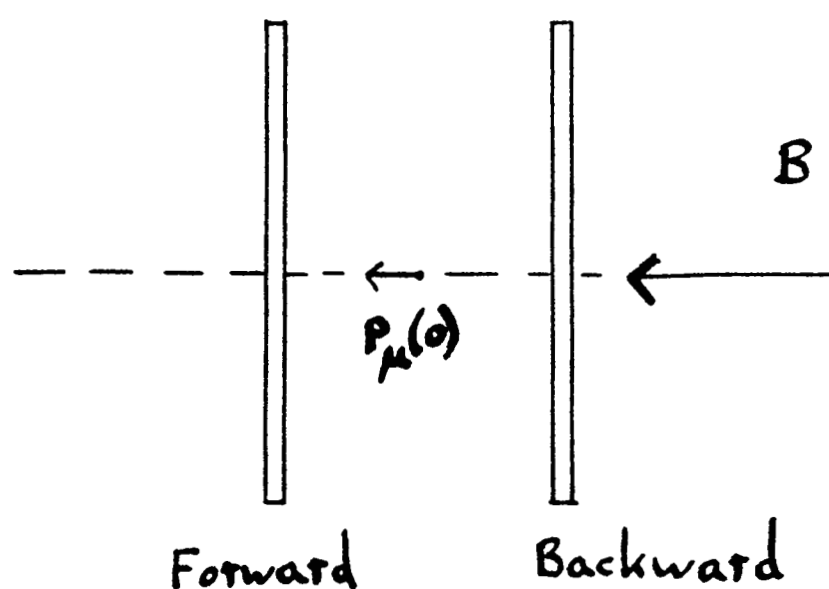
Fig. 7 Basic detector arrangement for longitudinal measurement

The interesting information, $a_0G(t)$, is given by equation (9)

$$a_0G(t) = \frac{N_F - \alpha N_B}{N_F + \alpha N_B} \qquad (9)$$

The correct value for α is very dependent on the exact position of the sample with respect to the detectors and several schemes exist to establish it. At ISIS the most common is to apply a small magnetic field transverse to the polarisation. The polarisation then rotates and after half a cycle is pointing at the backward detector. The signal $a_0G(t)$ oscillates about the time axis if α is chosen correctly. Figure 8 shows the special case in which $G(t) = 1$ as would be obtained with a silver sample. The usual value of the magnetic field for this calibration is 20 G (2 mT). Hence the colloquial name "T20" for this procedure.
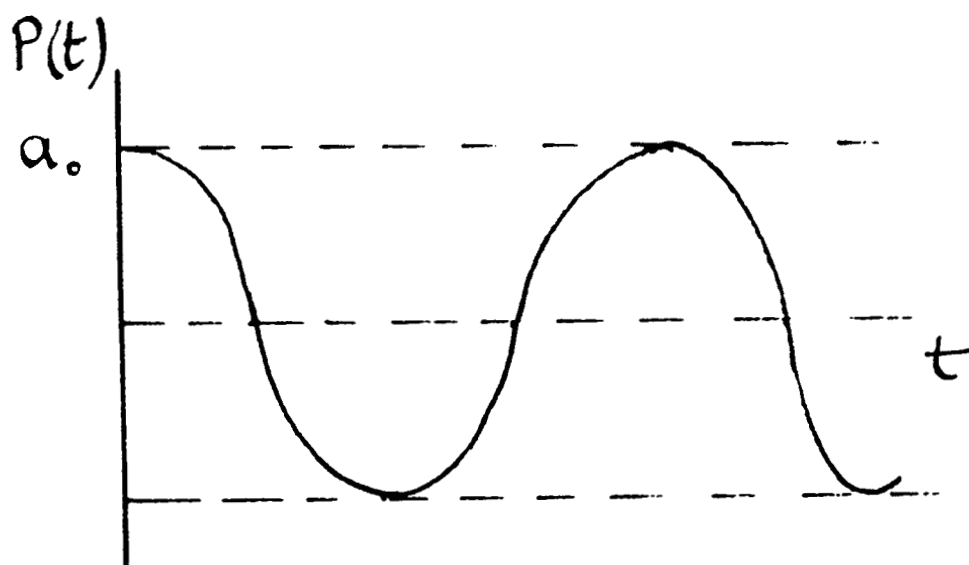
Fig. 8 α calibration – "T20"

7. MuSR and EMU

The layout of a μSR spectrometer is largely determined by the compromises made in fitting three main elements into the space around the sample at the end of a muon beam line. These elements are:

    a) The coils to provide magnetic fields
    b) The positron detectors
    c) Access for sample environment equipment *e.g* cryostats

As in many other μSR spectrometers the magnetic field in MuSR and EMU is generated by water–cooled copper coils and the space around the sample is maximised by dispensing with an iron yolk. At a pulsed source the positron detectors need special attention because the count rate is very high. Typically hundreds of muons are stopped in the sample in each pulse and on average decay in 2.2 μs. This rate is far too high to be handled by just a few detectors bearing in mind the dead time of a typical detector chain. The solution is to subdivide the detectors into many small *segments* each with its own detector chain so that the rate is manageable in each segment. Thus both MuSR and EMU have 32 segments and collect 32 histograms. The data is arranged into more
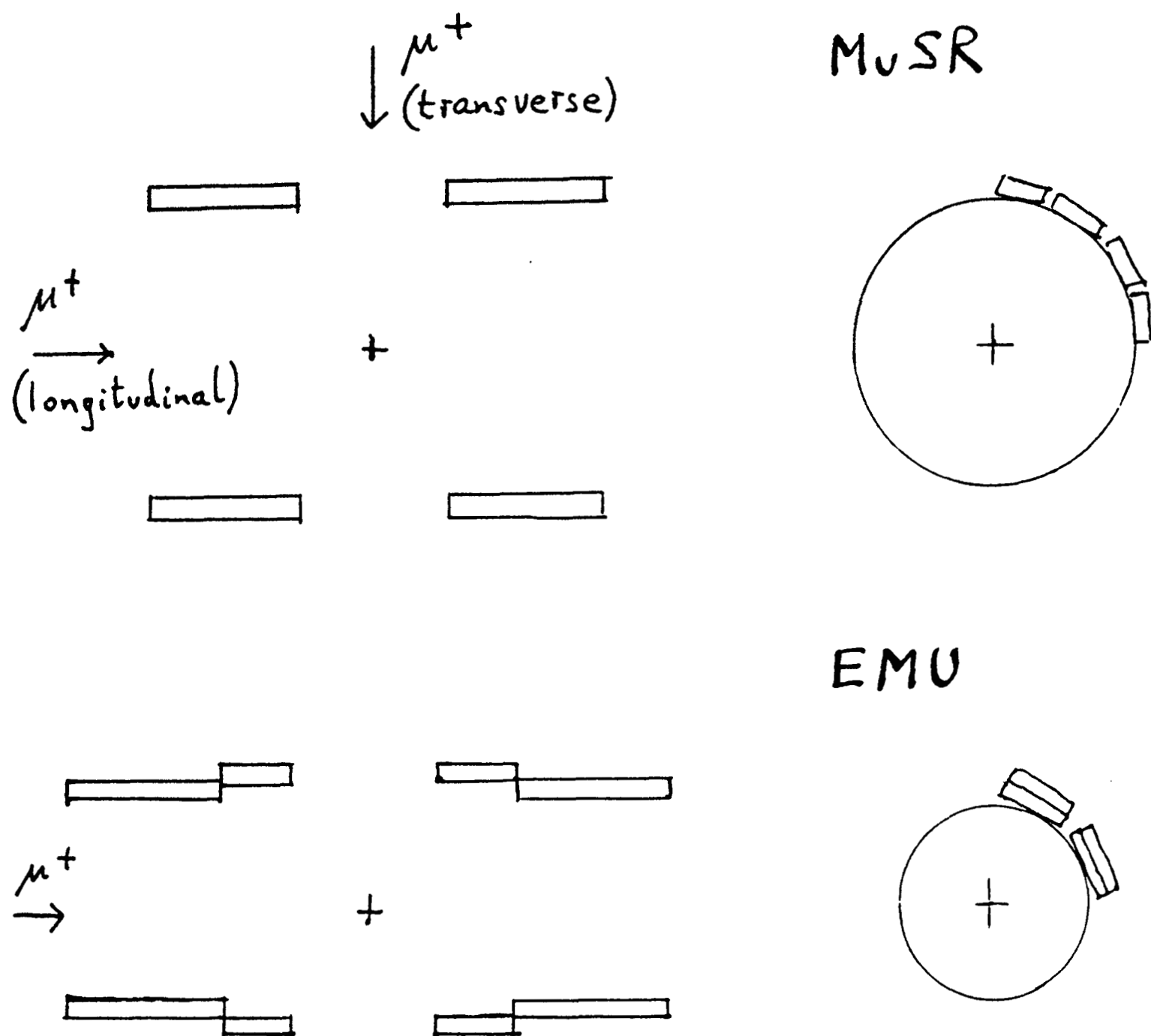
Fig. 9 MuSR and EMU detectors

tractable form in the analysis software. In MuSR the segments are identical and arranged in two sets on the surface of a cylinder co-axial with the coils providing the main magnetic field (Fig. 9 and Fig. 10). The coils are mounted on a turntable which for longitudinal geometry is turned so that the muon beam enters along the axis. The forward and backward detectors each consist of 16 segments. Transverse geometry is obtained if the assembly is rotated through 90°. There are then 16 transverse detectors each with two segments.

The MuSR spectrometer was designed by the Parma Group to be a good compromise between a transverse and a longitudinal instrument. By the time that the EMU instrument was designed it was clear that the demand at ISIS was principally for longitudinal geometry so EMU has its main field coils fixed and the detectors located closer to the position for optimum longitudinal performance (Fig. 9 and Fig. 10). There are two sizes of detector designed so that the solid angle, and thus the positron rate, of the inner and outer sets is equal. Transverse μSR is still possible on EMU because the small coil intended for the calibration T20 measurements is water-cooled and can provide 100 G.

In summary, the main features of μSR at a pulsed source compared to a continuous source are that the histogram background is much lower (good for LF and ZF), but the frequency response is poor (not so good for TF) and that it is necessary to subdivide the detectors and thus multiply the quantity of electronics to limit dead time problems.

POLARISED
MUON BEAM

DETECTORS

CRYOSTAT

MuSR

CRYOSTAT

LIGHT GUIDES & SCINTILLATORS

MAIN COILS

EMU

0   0.5   1 M
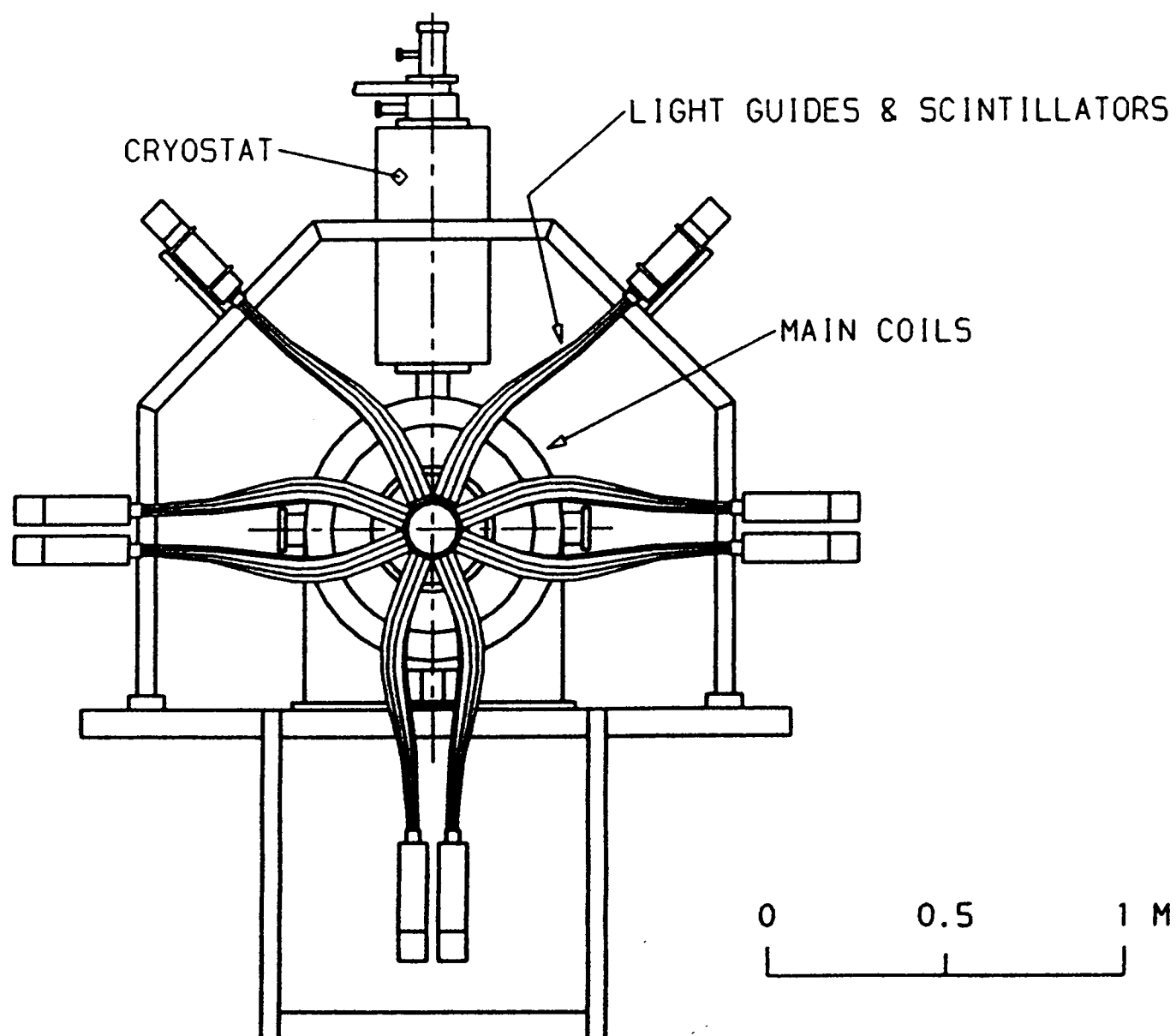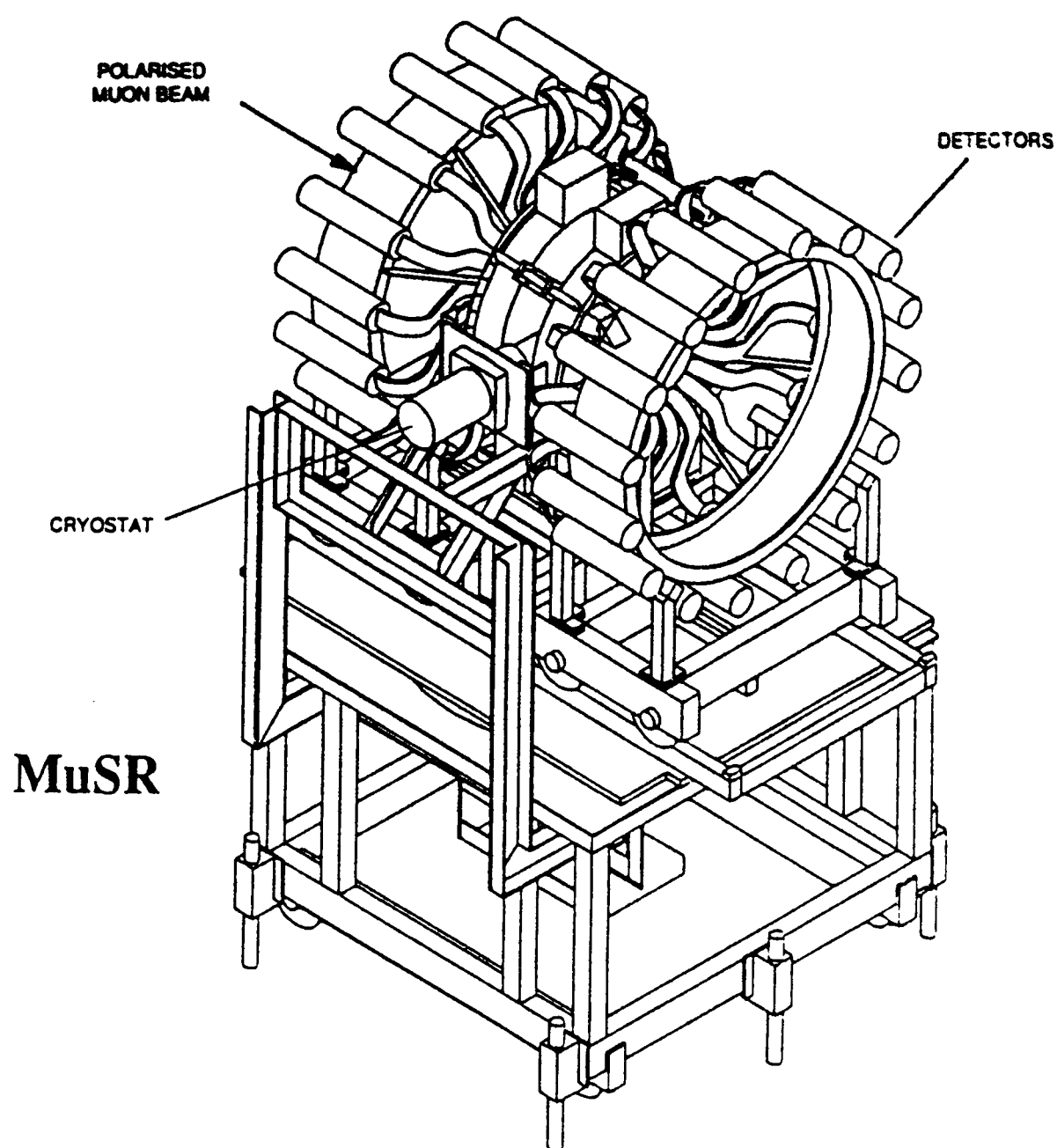
Fig. 10 MuSR and EMU

8. Technical Specification for MuSR and EMU (revised 1996)

Beam

Production target	5, 7 or 10 mm graphite
Momentum of μ^+	26.5 MeV/c, 10% momentum bite
Pulse structure	single pulse 80 ns FWHM
Contamination	$e^+/\mu^+ < 0.015$ (separator voltage > 70 kV)
Beam size at focus (FWHM)	vertical 8 mm (MuSR), 10 mm (EMU)
	horizontal, adjustable 7 – 15 mm (MuSR)
	10 – 27 mm (EMU)
Total intensity	$4 \times 10^5 \mu^+/s$ shared by the three areas
	(5 mm target, ISIS current 180 μA)
Polarisation	100%
Range	approx. 110 mg/cm^2
Background	Histograms contain a constant background of about 10^{-5} times the count in the first bins
Data acquisition	Both instruments have 32 TDCs with time resolution settings of 8, 16, 24 or 32 ns and each instrument is controlled by a VAXstation 3200

Sample environment

MuSR	Helmholtz coils (0 – 200 mT)(transverse or longitudinal)
	Zero field compensation ($< 3 \mu$T)
	Closed cycle refrigerator (12 – 340 K)
	Orange cryostat (2 – 300 K)
	Dilution refrigerator (40 mK – 4.2 K)
EMU	Helmholtz coils (0 – 450 mT)(longitudinal only)
	Calibration coils (0 – 10 mT)(transverse)
	Zero field compensation ($< 3 \mu$T)
	Closed cycle refrigerator (12 – 340 K)
	Oxford Instruments cryostat (2 – 300 K)
	Sorption cryostat (350 mK – 300 K)

Aspects of Data Treatment for Transverse μSR

B.D.Rainford

Department of Physics, University of Southampton

Introduction

My main message is that in μSR experiments we are always fighting with poor counting statistics, so we must do nothing to our data which makes matters worse, and we should do whatever we can to extract the most from what we have. The approach is geared to the typical set-up encountered at the pulsed muon beams at ISIS, but is readily generalised to other situations.

1. A typical ISIS μSR data set.

A data set collected on the MUSR or EMU spectrometers at ISIS consists typically of 32 histograms containing between 1000 to 2000 time channels; channel widths are 8 or 16 ns. These widths are chosen to match the width of the muon pulse, which is of order 70ns (FWHM). As an example let us consider a data set of 1500 channels, with channel width 16ns. The total time window for data collection is then 0 to 24 μs. As the muon lifetime τ_μ is 2.2 μs, the end of the time window corresponds to 10.9 τ_μ, by which time the initial decay count rate will have dropped by a factor $\exp(-10.9) = 2 \cdot 10^{-5}$! Fortunately the background at ISIS is very low, so it is still possible to collect data out to these times, though the statistics will inevitably be poor.

To develop a feeling for counting statistics, let us consider a standard silver run, measured for one hour (this is a typical duration for a measurement), corresponding to $2 \cdot 10^7$ events (20"Mev"), summed over all 32 histograms. The counts in the n'th channel of the j'th detector are given by:

$$C_j(t_n) = N_j^0 \Delta t \, \exp(-t_n/\tau_\mu)[1 + A_j \cos(\omega_L t_n - \phi_j)] \qquad (1)$$

where A_j is the asymmetry parameter (typically $A_j = 0.23$ at ISIS), ϕ_j is the phase, Δt is the channel width, N_j^0 is the initial count rate, $\omega_L = \gamma B$ is the muon Larmor precession frequency for an applied field B and the gyromagnetic ratio $\gamma/2\pi = 135.54$ MHz/Tesla. Ignoring the oscillatory term in (1) for the moment, we can sum over all time channels, to estimate the total number of events per histogram:

$$\sum_n C_j(t_n) \approx \int_0^\infty N_j^0 \exp(-t/\tau_\mu) dt = N_j^0 \tau_\mu = C_j(0)\tau_\mu/\Delta t$$

Taking the total counts to be $2 \cdot 10^7/32$, then we find that $C_j(0)$, the counts at the start of the histogram, to be about 4500. The statistical error in this count is $\sqrt{C_j(0)} = 67$. Of all the events, we are only interested in that portion associated with the asymmetry, $A_j C_j(0) = 0.2 \times 4500 = 900$ counts. It follows that the statistical error in the asymmetry, at the *beginning* of the histogram, where we have the highest countrate, is only $67/900 \approx 7.4\%$ This is not very impressive! And at longer times it will be worse. If we wanted, say, 1% statistics on the initial asymmetry we would need $\sqrt{C}/(0.2C) = 0.01$, corresponding to $C_j(0) = 2.5 \cdot 10^5$ counts, or a total of 10^9 events in all 32 histograms! This would mean running for 55 hours on ISIS!

The moral is that in the average μSR experiment we are dealing with quite poor counting statistics. This is largely a consequence of (i) the signal being associated with only 20% of the total counts, and (ii) the short lifetime of the muon. Clearly it is essential, in analysing μSR data, to make every event count, and to avoid any process which throws away information, e.g. grouping detectors with different phases together: this might be useful for summary purposes, or plotting data during an experiment, but it will reduce the effective asymmetry, and is therefore *a bad thing* for the ultimate analysis of μSR data.

2. Determination of instrumental parameters.

2.1 Phases and start time.

The time t_n in (1) is measured with respect to the start time t_0, when the muons arrive in the sample: $t_n = n\Delta t + t_0$. The effective phase of the oscillatory term is therefore:

$$\psi_j = \phi_j - \omega_L t_0 = \phi_j - \gamma B t_0 .$$ All detectors should have a common value of t_0. This can be determined by measuring silver spectra for several different transverse fields B, fitting the countrate to (1) to determine the effective phases ψ_j, then plotting these as a function of B. The plots give straight lines which, when extrapolated to zero field, give the true phases ϕ_j. The start time can be extracted from the gradients. Alternately the phases ψ_j can be determined for different assumed values of t_0, then plots of $\psi_j(t_0)$ for different fields should intersect at the true value of t_0.

Fitting of (1) to a silver spectrum in order to determine the phases is straightforward: it can be implemented by a linear least squares method, since (1) can be written as:

$$C_j^t = \alpha_j F_t + \beta_j G_t ,$$ with $\alpha_j = \sin\phi_j$; $\beta_j = \cos\phi_j$. Then following the usual approach

$$\chi^2 = \sum_t [C_j^t - \alpha_j F_t - \beta_j G_t]^2/\sigma_{jt}^2$$

and the values of α_j and β_j can be found by minimising χ^2 in the normal way.

2.2 Dead time corrections

The countrate equation (1) assumes a linear detector response, i.e. that the number of detected events in a given time channel is simply proportional to the number of decay positrons at that time. In general this is a reasonable assumption for low count rates, but at high count rates we have to correct for the "dead time" of the detector. This arises because the counting chain cannot respond to two events which come very close together: the counter is "dead" for a time τ_d after the first positron is detected. Since for μSR data the count rate is initially high and then falls with time, the effect of the dead time will be biggest at early times, and will become negligible at later times. The corrections for dead time can be derived from a standard zero field silver run, preferably one with good statistics.

To see the effect of dead time, let us consider a simple case, where N(t) represents the ideal counting rate and M(t) is the recorded counting rate. In a single time channel of width Δt, the detector will be dead for a time $M(t) \Delta t \tau_d$, so the measured count in this time channel will be $M(t)\Delta t =$

$N(t)\Delta t[1-M(t)\tau_d]$. It follows that the recorded count rate is

$$M(t) = \frac{N(t)}{1+N(t)\tau_d} \qquad (2)$$

Clearly when $N(t)$ is small, and the product $N(t)\,\tau_d \ll 1$, then $M(t) \approx N(t)$. However when the countrate is very high, the measured counts tend to the limiting value $M(t) = 1/\tau_d$. To determine the dead times for each detector, the measured counts in a zero field silver run can be fitted to (2), with $N(t) = N_0 \exp(-t/\tau_\mu)$. If only a transverse field silver run is available, the same procedure can be used, but in this case the ideal counts are as given in equation (1). In practice for a typical ISIS count rate the dead time corrections at short times are about 5% or less. Since this is small, it is feasible to linearise (2) by using the binomial expansion then discarding terms beyond the second:

$$M(t) = N(t) + N(t)^2 \tau_d + \cdots$$

We can then use an efficient linear least squares approach to estimate the dead time corrections to an acceptable level of precision.

3. Analysis of μSR spectra

There are two perspectives for the interpretation of transverse field μSR spectra:

(a)   the muon spins precess at a frequency ω_L, but their polarisation decays with time due to the muons' interaction with static or dynamic fluctuations in its environment. In metals the precession frequency ω_L might be shifted slightly from the value γB (Knight shift), reflecting an enhanced susceptibility at the muon site in the sample.

(b)   the muons at different sites see a distribution of internal fields, and therefore precess at different rates. This is the case, for example, in the mixed state of superconductors (see contribution by S.Lee).

We will consider these situations in turn.

3.1 (a)   If the muons precess at a common frequency ω_L, but their polarisation decays with time, the counts in each detector can be written:

$$C_j(t_n) = N_j^0 \Delta t \, \exp(-t_n/\tau_\mu) \, [1 + A_j P_x(t_n) \cos(\omega_L t_n - \phi_j)] \qquad (3)$$

$P_x(t)$ describes the decay of the muon polarisation. The form of this decay depends on the physics of the muon's interaction with its environment. In the limit of fast temporal fluctuations of the local field or of rapid hopping of the muon from site to site it can be shown that $P_x(t) = \exp(-\lambda t)$: this is traditionally (and confusingly) called "Lorentzian damping" because this limit is identical to the limit of strong motional narrowing in NMR, where the lineshape (equivalent to the Fourier transform of $P_x(t)$), is indeed a Lorentzian function. In the limit of slow temporal fluctuations, but where there is a Gaussian distribution local fields (inhomogeneous broadening) it is readily shown that $P_x(t) = \exp(-\sigma^2 t^2)$. Other functions in the literature, e.g. the Abragam function, are designed to describe circumstances between these two limiting cases. The point is that the shape of the envelope of the decaying polarisation gives information about the physics of the interaction at the muon site, which

can be described by an analytical function with a few parameters (e.g. λ or σ in the above expressions). Analysis of the data is then a simple matter of least squares fitting the expression (3) to the data, with the appropriate form of $P_x(t)$. Following our dictum in section 1, we should, if possible, fit *all* the histograms (j=1 to 32) at the same time, without grouping them together, after making necessary corrections for dead times. In this case there will be three instrumental parameters for each histogram, namely N_0^j, A_j and ϕ_j, as well as the parameters describing the polarisation $P_x(t)$. In practice it is best to predetermine the phases as described in section 2.1, using a standard silver run, since the phases might not be well determined in a fit to the data, especially when the polarisation is rapidly damped. Fitting 32x1500 time channels with 65 parameters might seem like a tall order, but computing power is cheap compared to the cost of doing μSR experiments.

3.1 (b) If the muon sees a distribution of internal fields the counts in each detector will be:

$$C_j(t_n) = N_j^0 \Delta t \exp(-t_n/\tau_\mu) \, [1 + A_j F_j(t_n)] \tag{4}$$

where
$$F_j(t_n) = \int_0^\infty F(\omega)\cos(\omega t_n - \phi_j)d\omega.$$

The function $F(\omega)$ gives the distribution of precession frequencies, which maps directly onto the distribution of internal fields through the gyromagnetic ratio: $\omega = \gamma B$. The problem is how to extract $F(\omega)$ from the data. This is clearly a Fourier transform problem, but standard Fourier methods have some drawbacks, in particular:

(i) the poor statistical accuracy of the μSR data at long times leads to very noisy transforms. Of course there are standard techniques for coping with this, for example use of window functions ("apodisation"). There is a large literature on how to choose the optimum window function, however whichever one is chosen, they all involve throwing away data, and some deterioration of the frequency resolution.

(ii) we have a problem of how to derive a unique frequency spectrum $F(\omega)$ from 32 separate histograms, with different phases ϕ_j.

Recently this problem has been tackled using the Maximum Entropy method [1]. This technique has been widely used to deal with a range of inverse problems in fields such as radio astronomy, geophysics and image reconstruction (including processing images from the Hubble telescope to correct for the aberrations in the mirror) etc. Applied to the present problem it has many advantages:

● It uses all the data available, but allows a unique frequency spectrum to be determined from multiple histograms.
● The frequency spectrum derived is necessarily positive.
● There are no prior assumptions about the form of the function $F(\omega)$.
● It gives the most uniform (N.B. *not* smoothest) distribution consistent with the data.
● It is possible to include convolution with the muon pulse shape.
● The ultimate frequency resolution can be achieved.

Details of the method will not be given here, since they are discussed in ref.[1]. Briefly the entropy S is defined in the information theoretic sense as:

$$S = -\sum_{i=1}^{N} (p_i/b_i)\log(p_i/b_i)$$

where the $\{p_i\}$ represent the heights of the bins in the histogram representing the frequency spectrum. The b_i represent the default values which give a scale to the magnitudes of the p_i. In practice the default is taken to be a flat level, independent of i. Starting from this featureless default level, the ME algorithm searches for a solution which maximises $S - \lambda\chi^2$, where λ is a Lagrange multiplier. Initially λ is chosen so that the algorithm puts most effort into minimising χ^2, with the aim of reducing its value to be equal to the number of data points. In the later stages the value of λ is altered to concentrate on maximising the entropy. The advantage of the technique is that it tackles the forward problem, i.e. generates a frequency spectrum which is then transformed, as in (4), to give the measured counts in each histogram, which are then compared to the measured values. This facilitates the incorporation of any transformation between the frequency domain and the time domain, e.g. convolution with the pulse shape of the muon bursts. The resulting frequency spectra produced by the method are impressive. For example Fig.1 shows the frequency spectrum for silver, which is very close to a delta function, as we might expect.

Figure 1. Maxent frequency spectrum for silver at an applied field of 220 gauss. The width of one frequency channel corresponds to 30.5 kHz or 2.25 gauss.

Applications of the maximum entropy method to data for superconducting samples in the mixed state are presented in Dr. Lee's contribution.

4. Limitations to the transverse µSR method.

4.1 Effect of finite muon lifetime.

Clearly µSR would not work if the muon did not decay! However the finite lifetime of the muon means that we can only collect useful data for, perhaps, five muon lifetimes (data at longer times are useful if we are prepared to count for a long time to improve the statistics). This immediately implies a limit to the frequency resolution of the transverse µSR technique. To see this consider the standard approach from the theory of discrete Fourier transforms (DFT): in a DFT of data comprising n channels with channel width Δt the frequency resolution Δf is simply $1/n\Delta t = 1/T$, i.e. the reciprocal of the total time for which data has been collected. If we take $T = 5\,\tau_\mu = 11$ µsec, then $\Delta f \approx 90$ kHz. Transforming this from frequency to magnetic field, using the gyromagnetic ratio of the muon, the resolution in magnetic field is about 0.7 mT or 7 gauss. Note that this is a
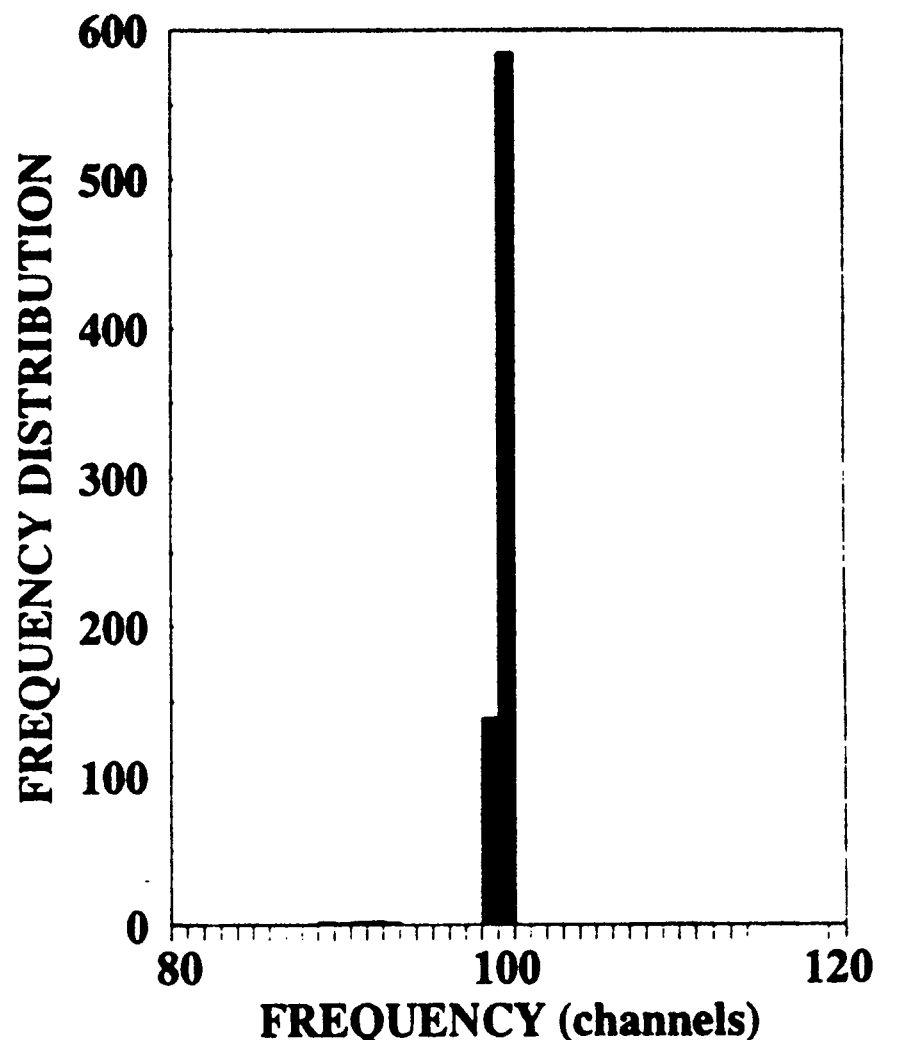
fundamental restriction, no matter how good our instrumentation or data analysis.

4.2 Effect of finite pulse width.

The time structure of the muon beam at ISIS reflects that of the proton pulses at the production target, i.e. two pulses of width 70 ns (FWHM) with a separation of 320 ns. The repetition rate is 50 Hz. The pulses are further smeared by the 26 ns lifetime of the parent pions. The first of the double pulses is split between the two μSR instruments EMU and DEVA, while the second pulse passes on to the MUSR instrument. It follows that the time dependent countrate (3) or (4) should be convoluted with the pulse shape of the incident muon beam. This will have a significant effect only when there are variations in the countrate on a time scale comparable to the pulse width. There are two particular cases where this might be important: (i) when the Larmor precession frequency is high, and (ii) where there is rapid decay of the muon polarisation. Let us consider these in turn.
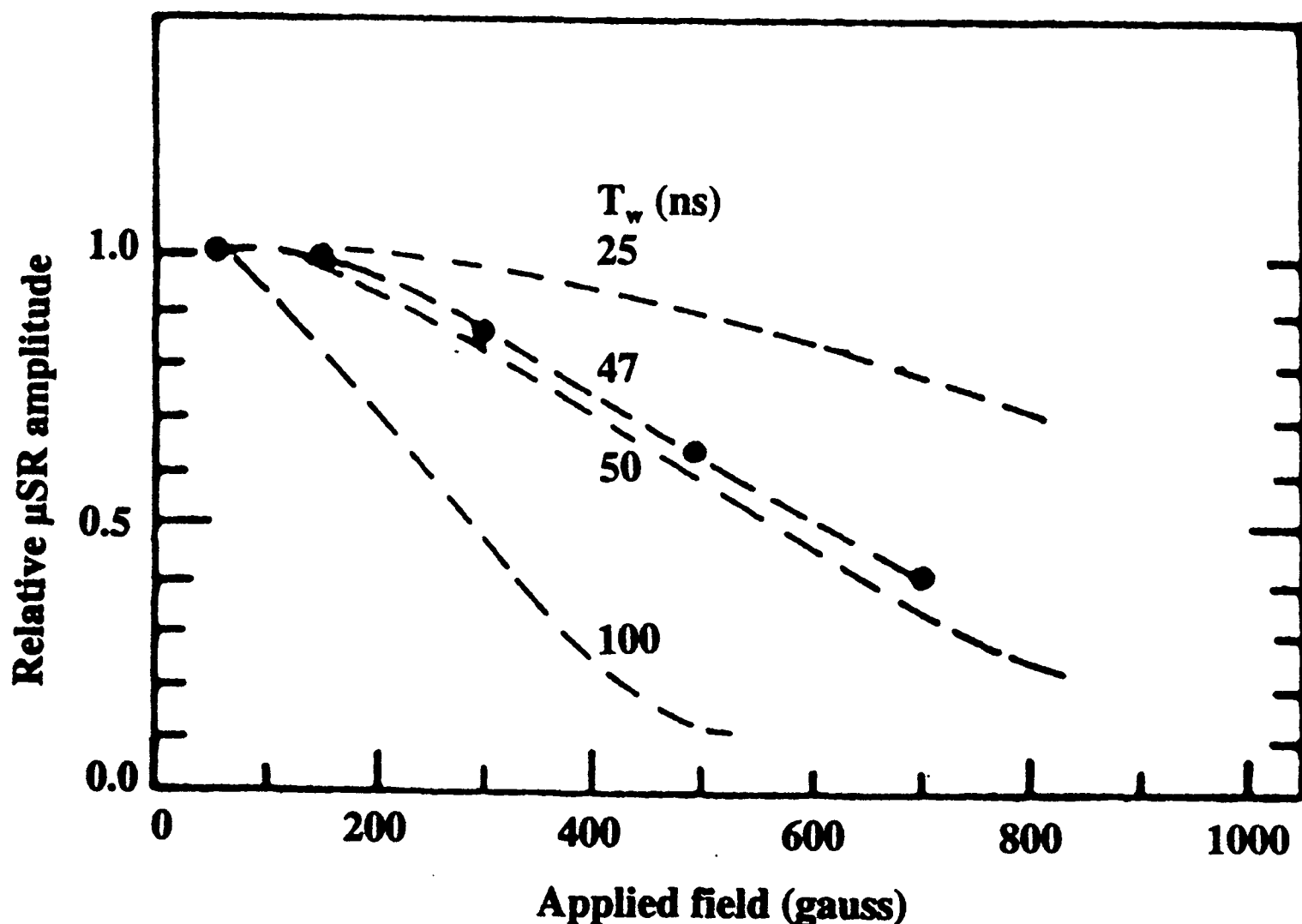

Figure 2. Variation of asymmetry with external field due to the finite width of the muon pulses (T_w is FWHM pulse width in nsec), after Nagamine and Yamakazi.

4.2 (i) Upper limit to the external field.

Suppose that we take the muon pulse shape to be a gaussian: $W(t) = \exp(-t^2/\tau_w^2)$. This is not strictly correct: a better approximation at ISIS is an inverted parabola, describing the proton pulse, convoluted with a decaying exponential, in order to account for the pion lifetime component. However a simple gaussian simplifies the result greatly. If we are studying a material like silver which is weakly damped, the resulting signal would be the convolution of the "ideal" signal ~ $[1 + A \cos(\omega_L t)]$ with $W(t)$. Here A is the ideal asymmetry and ω_L is the

Larmor precession frequency, as usual.   It is straightforward to show that the effect of the convolution is to reduce the asymmetry to a value $A\exp(-\omega_L^2 \tau_w^2 / 4)$. The reduction in the asymmetry with applied field is shown in Fig.2 for different values of the pulse width T_w (FWHM). It follows that the asymmetry falls to $1/e$ of its ideal value at an applied field B given by $(\omega_L/2\pi) = (\gamma/2\pi)B_{1/e} = 1/(\pi \tau_w)$. For a pulse width of 70 ns (FWHM) the value of $\tau_w \approx 42$ ns, and the corresponding field $B_{1/e}$ is 560 gauss. The reduced asymmetry resulting from high Larmor precession rates degrades the signal to noise ratio, as is clear from the discussion in section 1 above.

4.2 (ii) Upper limit to damping rate.

If the damping rate were very high then the muon polarisation $P_x(t)$ would fall to a small value within one Larmor precession period, or in the extreme case, within the muon pulse width. In the latter case, Lorentzian damping would only be visible for values of the damping rate smaller than λ_{max} given by, say, $\exp(-\lambda_{max}\tau_w) \approx e^{-1}$: that is we suppose that the muon polarisation decays by $1/e$ over the duration of the muon pulse. Using the above value $\tau_w = 42$ ns gives a value for $\lambda_{max} \approx 24$ μs^{-1}. However to extract such a value from real data would require a very accurate knowledge of the pulse shape and the start times for each histogram: λ could then be derived by fitting the appropriate form for $P_x(t)$ after convolution of (3) with the pulse shape. Notice that the situation at ISIS for measuring heavily damped signals is very much improved now that single pulses are used: with the same criterion as above for a double pulse of muons separated by 320 ns we find a value of λ_{max} of only 2.9 μs^{-1}. In practice convolution with the pulse shape is necessary to extract reliable values of λ for damping rates greater than 3 - 5 μs^{-1}, but the extra data analysis effort required is well justified.

References

[1]   B.D.Rainford and G.J.Daniell, Hyperfine Interaction **87** (1994) 1129.

USING POSITIVE MUONS TO INVESTIGATE HIGH-TEMPERATURE SUPERCONDUCTORS

S.L. Lee
Physik-Institut der Universität Zürich, Winterthurerstrasse 190, CH-8057 Zürich, Switzerland.

Abstract

A short review is presented of the application of the muon-spin rotation (μ^+SR) technique to the investigation of high-temperature (HTC) superconducting materials. An elementary discussion of the mixed state in extreme type-II superconductors is given, and it is shown how μ^+SR may be used to measure the probability distribution $p(B)$ of the internal magnetic fields in this state. Different methods for extracting the superconducting penetration depth λ from $p(B)$ are described. Measurements of the temperature dependence of λ are briefly discussed, and a review is given of some recent measurements and theories concerning 'universal' trends of λ in the HTC materials. Recent μ^+SR measurements of $p(B)$ in $Bi_2Sr_2CaCu_2O_8$ (BSCCO) are presented, which provide strong evidence for flux-lattice melting in this material.

1. Introduction

Over the past decade the use of muons to investigate problems in solid state physics has become a powerful and established technique [1, 2]. This is particularly true in the field of superconductivity where the muon has proved to be a unique microscopic probe of the magnetic properties. While muon techniques have been applied successfully to the study of magnetic ordering in families of superconducting materials, especially in the high-temperature (HTC) superconductors (see e.g. [2]), it is on the investigation of the superconducting state itself that I shall concentrate.

The muon-spin rotation (μ^+SR) technique provides a sensitive measure of microscopic field distribution inside a type-II superconductor, which in turn is related to the magnetic penetration depth λ; this is one of the fundamental lengths of a superconductor, and is related to to the superconducting order parameter. By using μ^+SR to measure λ as a function of temperature it might therefore be possible to investigate the pairing mechanism of the superconducting state. The details of the microscopic flux distribution itself is also of great interest, particularly in view of some of the exotic magnetic phases proposed by recent theories for HTC systems [3]. Here I would like to discuss the application of μ^+SR in some of these areas, with specific reference to some recent results. Although necessarily incomplete, it is hoped that the examples given are representative of trends in the application of the μ^+SR-technique to HTC research.

The discussion is organised as follows: In Section 2 I shall review some basic aspects of the mixed state in type II superconductors, and how we may utilise the μ^+SR-technique to investigate the microscopic field distribution. In Section 3 the measurement of the magnetic penetration depth will be discussed, for arbitrary geometry in an anisotropic

superconductor; the temperature dependence will also be briefly considered. In Section 4 trends of the superconducting properties within families of HTC materials will be discussed, including some recent results and ideas. The application of μ^+SR to the investigation novel vortex structures is discussed in Section 5, together with some recent results which give evidence for flux-lattice melting. A summary is presented in Section 6.

2. Probing the mixed state with muons

In the mixed state of a type-II superconductor, for applied fields larger than the lower critical field H_{c_1}, flux enters the bulk in the form of quantised lines of flux (see e.g. [4]). Each flux-line carries one quantum of flux $\Phi_o = h/2e$ and consists of a core of normal electrons around which there is a vortex-like flow of supercurrents. Such a vortex line is shown schematically in Fig.1(a), where two of the important lengths of the superconducting state have also been indicated; the first is the temperature-dependent superconducting coherence length $\xi(T)$, which may loosely be thought of as the distance over which the superconducting wavefunction $\psi(r)$ can fall to zero, and effectively defines the dimensions of the normal core. The second is the magnetic penetration depth $\lambda(T)$, which is a measure of the distance over which the circulating supercurrents may screen a magnetic field, and thus gives the spatial extent of the isolated flux-line. As the applied field is increased, so is the internal density of flux-lines, so that they begin to overlap. In this case the field no longer falls to zero between flux-cores, as shown Fig.1(b). Due to the mutual repulsion between flux-lines they form a regular Abrikosov-lattice of plane spacing d, so that the internal flux-density $B \approx \phi_o/d^2$. At low temperatures HTC superconductors are characterised by $\lambda(0) \geq 1300$Å and $\xi(0) \leq 30$ Å, so that the Ginzburg-Landau parameter $\kappa = \xi/\lambda \gg 1$; such materials are normally described as extreme type-II superconductors. For such a system the finite core size only becomes important for very high flux-densities, at which the cores themselves begin to overlap. Thus, for a very large range of fields $H_{c_1} \ll H \ll H_{c_2}$, the flux distribution over most of space is determined largely by λ.
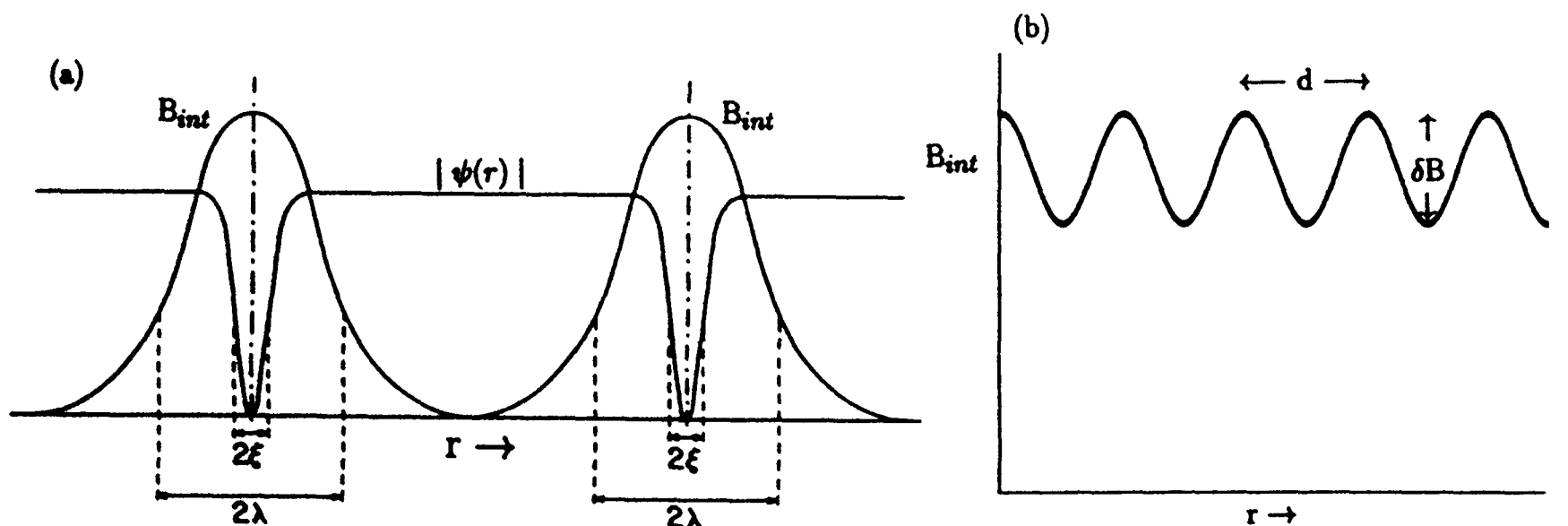

Figure 1: The structure of flux-lines in the mixed state (a) $H_{ext} \sim H_{c_1}$ and (b) $H_{c_1} \ll H_{ext} \ll H_{c_2}$, where a lattice of period d exists with a field contrast $\delta B = B_{max} - B_{min}$.

In the μ^+SR-technique, highly spin-polarised muons are brought to rest in a sample which sits in a magnetic field H_{ext} directed perpendicular to the muon spin. The muons then undergo Larmor precession in the local internal magnetic field B_{int} at an angular frequency $\omega = \gamma_\mu B_{int}$, where $\gamma_\mu = 2\pi \times 1.36 \times 10^8$ Hz T^{-1}. The evolution with time of the

muons may be measured by the detection of positrons which are emitted preferentially along the muon-spin direction during the decay of the muon, which has a mean lifetime of $\tau_\mu =2.2\mu s$. (For a more detailed discussion see for example [1]). A typical spectrum from such an experiment is shown Fig.2, where the positron detector output is shown as a function of time. One can clearly see the oscillations due to muon-spin precession superimposed on the exponential muon decay. In general the observed spectrum may be described by the following function:

$$N(\theta,t) = N_o exp(-t/\tau_\mu)[1 + AR(t)cos(\omega t + \theta)] + b \qquad (1)$$

where N_o is the normalisation constant, A is the precession amplitude, θ is the initial phase, b is a constant background and ω and τ_μ are as defined above. The relaxation function $R(t)$ describes the damping of the precession signal, which in the mixed state arises from the distribution of internal fields $B(\mathbf{r})$ around the average internal field $B_{av} = \langle B(\mathbf{r})\rangle$, where $\langle\rangle$ denotes the spatial average. Thus $R(t)$ contains information about the internal field distribution of the vortex structure. This damping of the signal amplitude is readily observable in Fig.2(a). If one divides out the exponential decay from Eq.1 and performs a Fourier transform of the data using some suitable technique, then one obtains the probability distribution $p(B)$ of the internal field, which has a form determined by the details of the vortex structure. Such a $p(B)$ for an idealised triangular lattice of vortex-lines is shown in Fig.2(b), and its details may be related to the spatial distribution $B(r)$ [5]. In particular the long "tail" at fields higher than the applied arises from regions close to the vortex cores. Thus one may investigate the field distribution arising from different vortex arrangements in the mixed state by measuring the μ^+SR-lineshapes [6, 7].
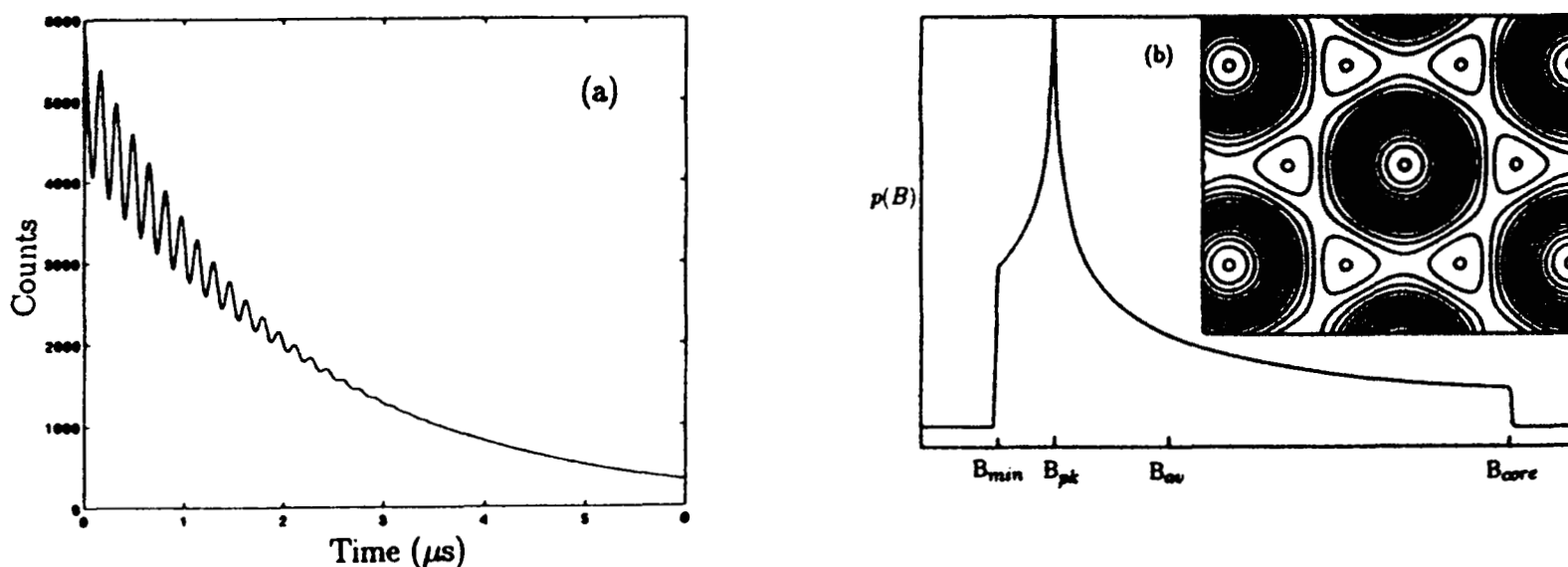

Figure 2: (a) A typical μ^+SR time spectrum obtained from a superconductor in the mixed state. (b) Probability distribution $p(B)$ for an ideal triangular vortex-line lattice. The inset shows the field contour plot of the corresponding lattice.

3. Measurement of the magnetic penetration depth λ

For an isotropic type II superconductor in the 'clean limit' [4] the magnetic penetration depth may be determined from:

$$1/\lambda^2(0) = \mu_o e^2 n_s(0)/m^*, \qquad (2)$$

3

where $n_s(0)$ is the density of the superfluid pairs at zero temperature and m^* is the effective mass of the superconducting pairs. Due to the short coherence length in HTC materials Eq.2 should be a good description of λ. Thus λ is directly related to the superconducting charge carrier density and its temperature dependence provides important information on the pairing mechanism [4, 8, 9]. $\lambda(T)$ may often be described by the empirical formula:

$$\lambda(T) = \lambda(0)/(1 - t^n)^{1/2}, \tag{3}$$

where $t = T/T_c$ is the reduced temperature. Setting $n = 4$ gives the two-fluid model [4], which for extreme type-II superconductors ($\kappa \gg 1$) represents a good approximation of the temperature dependence of an s-wave superconductor in the limit of strong coupling [8].

It has long since been realised that magnetic resonance methods can be used to measure directly the penetration depth of extreme type-II superconductors [10]. More recently the analysis has been extended to describe the case of an anisotropic high-κ system such as the HTC cuprates [11, 12, 13, 14, 15]. The penetration depth λ may be obtained from the second moment (linewidth) $\langle \Delta B^2 \rangle$ of the field distribution $p(B)$, which in general may be written as the sum over reciprocal lattice-vectors $\mathbf{G}$ of the Fourier component of the internal magnetic field:

$$\langle \Delta B^2 \rangle = \sum_{\mathbf{G} \neq 0} h(\mathbf{G}). \tag{4}$$

In the HTC cuprates, for the simple geometry of the applied field H_{ext} parallel to the crystallographic $\hat{c}$-direction, this has been calculated to give

$$\langle \Delta B^2 \rangle = 0.00371 \Phi_o^2 / \lambda^4 \tag{5}$$

for a triangular lattice when $H_{c_1} \ll H_{ext} \ll H_{c_2}$ [11, 12]. Thus for a very wide range of fields the second moment is independent of field, and Eq.5 may be used to evaluate λ directly. The conduction properties of HTC materials are anisotropic and have roughly uniaxial symmetry, so two principal values of the effective mass must be considered, m_{ab}^* and m_c^*; these describe the supercurrents flowing parallel and perpendicular to the ab-planes (copper-oxide planes) respectively. For an arbitrary angle θ of the applied field to the $\hat{c}$-direction, the effective penetration depth must then be described by a tensor relation [13]. It has been shown that within the London approximation one may describe a uniaxial superconductor for arbitrary field orientation by

$$\langle \Delta B^2 \rangle(\theta) = \langle \Delta B^2 \rangle(0)[cos^2(\theta) + \gamma^{-2} sin^2(\theta)] \tag{6}$$

where $\langle \Delta B^2 \rangle(0)$ is given by Eq.5 and $\gamma = (m_c^*/m_{ab}^*)^{1/2} = \lambda_c/\lambda_{ab}$ is the anisotropy ratio [14, 13, 15]. Eq.6 was found to be a good description of the angular-dependence of $\langle \Delta B^2 \rangle(\theta)$ in $YBa_2Cu_3O_{7-\delta}$ (YBCO), giving a value of $\gamma = 5$ [14]. However, for the highly anisotropic material $Bi_2Sr_2CaCu_2O_8$ (BSCCO) such a description was found to be inappropriate, probably due to the quasi-2D nature of the flux-structure [16] (Fig.3). To calculate $\langle \Delta B^2 \rangle$ for polycrystalline or powder samples an average must be taken over all the possible crystal orientations. It has been shown that for a powder sample with an anisotropy ratio $\gamma \geq 5$, $\langle \Delta B^2 \rangle$ depends only on m_{ab}^* and may be written as

$$\langle \Delta B^2 \rangle = 0.00371 F \Phi_o^2 / \lambda_{ab}^4 \tag{7}$$

where $F \approx 0.44$ [12]. Thus the penetration depth λ_{ab} due to the in-plane currents may be measured from polycrystalline samples without a precise knowledge of γ.
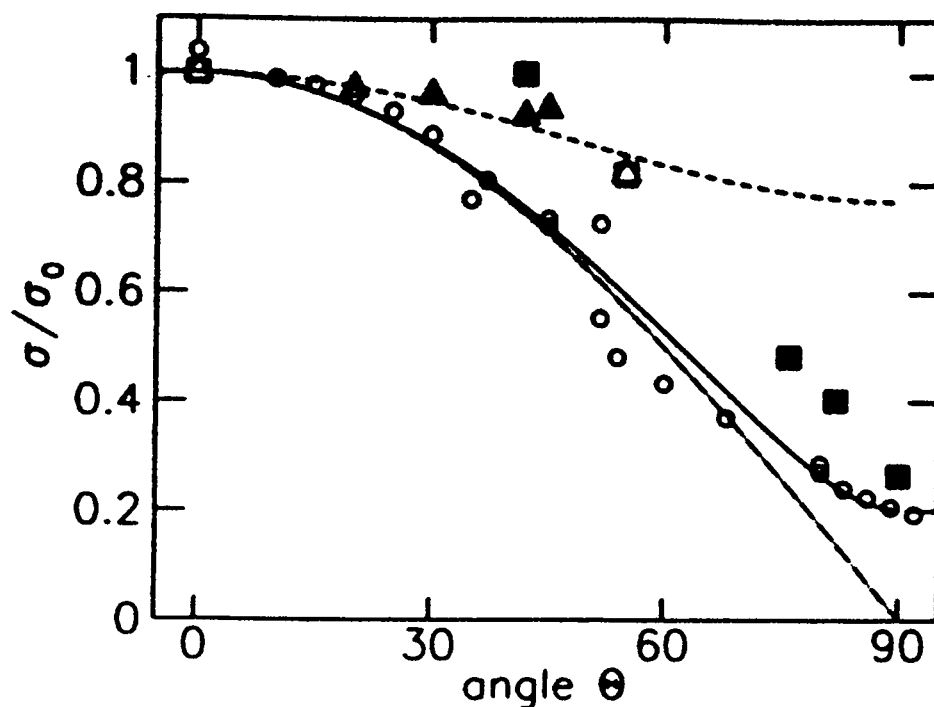
Figure 3: Angular-dependence of the muon-depolarisation rate σ (a) in single-crystal YBCO (open circles) and (b) in single-crystal BSCCO (triangles, squares). The solid-line is a fit to the YBCO data to Eq.6, giving a $\gamma = 5$. This model could not be used to describe the angular-dependence of the much more anisotropic BSCCO ($\gamma \geq 100$); the short and long dashed line correspond to $\gamma \approx 1$ and $\gamma \approx \infty$ respectively (taken from ref. [16]).

The μ^+SR-technique has proved to be an indispensible and reliable tool with which to measure the penetration depths of HTC materials. This has allowed systematic trends of the superconducting condensate density within families of materials and also to investigate 'universal' trends between different families (see Section 4). In practice for HTC systems the observation of probability distributions $p(B)$ resembling Fig.2(b) are rare, due to a variety of factors. Imperfections of the vortex lattice due to random pinning may have the effect of convoluting this lineshape with a Gaussian, which smears out the van Hove singularity [11, 5], while demagnetisation effects may cause significant distortions of the spectra from polycrystalline samples (see e.g. [17]). For a great many cases the observed spectra are in fact found to be approximately Gaussian. It follows that in the μ^+SR time-spectra the relaxation function $R(t)$ of Eq.1 may also be approximated by a Gaussian

$$R(t) = exp(-\sigma^2 t^2/2), \qquad \sigma = \gamma_\mu \langle \Delta B^2 \rangle^{1/2}. \qquad (8)$$

By this means the λ may be extracted by fitting Eq.1 to the raw μ^+SR time spectrum.

Despite the apparent ease with which values for λ may be extracted from μ^+SR measurements, there are several considerations which should be taken into account. Firstly, for a vortex-line lattice the effects of lattice imperfection may cause a significant broadening of the observed $\langle \Delta B^2 \rangle$ leading to an underestimate of λ [11, 5]. In general, therefore, the values of λ obtained from μ^+SR should be considered as a lower limit. However, for the case of a close to ideal lineshape such as Fig.2(b) the long tail towards high-field values has a low probability $p(B)$. For finite statistics not all of this tail will be observable above the experimental noise, leading to an incomplete spectrum. This apparent shortening of the tail will lead to an overestimate of λ. In such cases it is better to extract λ from the distance $B_{pk} - B_{av}$, where B_{pk} is the peak field of $p(B)$ and B_{av} is the average internal field, which may be determined from an independent method such as magnetisation measurements (see e.g. [18]). In highly anisotropic superconductors such as BSCCO the flux-structure may be quasi-2D [19], in which case random-pinning or thermally-induced disorder may cause a narrowing of the linewidth [20, 7, 21, 22], which can again lead to an overestimate of λ if a only simple interpretation of the lineshape is made.

5

The experimental results regarding $\lambda(T)$ are still still somewhat inconclusive. While the two-fluid model has been found to be a good description of the data in highly-oxygenated ceramic samples of YBCO [23], in ceramic $YBa_2Cu_4O_8$ and BSCCO the behaviour was found to be more BCS-like (weak-coupling) [24]. A recent study of the exponent n in Eq.3 as a function of δ in $YBa_2Cu_3O_{7-\delta}$ has shown a systematic variation, with values ranging from $n \approx 2$ at low oxygen contents to $n \approx 4$ for well oxygenated samples [25]. In general the situation may be complicated due to the influence of other factors on the measured second moments, as discussed above. Recent results in single-crystal BSCCO suggest that in that system thermal fluctuations of the vortex-positions may have a significant affect on the measured $\langle \Delta B^2 \rangle$, particularly at high fields [18, 7, 16, 22].

4. 'Universal' relations and trends in HTC materials

There have been many studies of the μ^+SR relaxation rate σ in both HTC and other extreme type-II materials (see e.g. [26] and references therein). In particular Uemura *et al.* performed a systematic study of the low-temperature value of σ for a large range of doped HTC materials. It was found that for all systems studied there was a common empirical relation between the transition temperature T_c and the zero-temperature relaxation rate $\sigma(0)$; such a diagram is shown in Fig.4 and is known the 'Uemura plot' [27]. Using Eqns. 2, 5 and 8 it can be seen that $\sigma(0) \propto n(0)/m_{ab}^*$, so the Uemura plot effectively shows the dependence of T_c on the condensate density. As the carrier doping is increased T_c increases up to a maximum value T_c^m and then saturates, and is eventually suppressed for higher doping levels. The initial rise of T_c is common to all families of materials, but each family saturates at a different T_c^m. Such a relation provides an important testing ground for theoretical models which attempt to account for high-temperature superconductivity. For instance, it has been argued that the specific dependence of T_c on σ cannot be accounted for within the framework of weak-coupling BCS theory [27].

A phenomenological theory has recently been proposed to describe the Uemura plot [26]. A parabolic maximum of T_c close to the optimum condensate density $\sigma_m(0)$ is assumed which leads to the following scaling form

$$\overline{T_c} = 2\overline{\sigma}(1 - \overline{\sigma}/2), \quad \overline{T_c} = T_c/T_c^m, \quad \overline{\sigma} = \sigma(0)/\sigma_m(0). \quad (9)$$

In this way a given family forms a unique branch, which is characterised by T_c^m and $\sigma_m(0)$. When the data for various families are plotted in this way they are found to lie on a single curve (Fig.4(b)). By assuming such an empirical relation, quantitative predictions may be made about thermodynamically related variables such as the pressure and isotope coefficients, where remarkable agreement is found with measured values [26, 28].

Recent μ^+SR measurements on the thallium-based system $Th_2Ba_2CuO_{6+\delta}$ have extended the Uemura plot well into the 'overdoped' region ($\sigma(0) > \sigma^m(0)$), where remarkably a *reduction* of $\sigma(0)$ is observed as the hole doping is increased beyond the optimum [29, 30]. For this system in the regime $\sigma(0) > \sigma^m(0)$ the Uemura is no longer parabolic, but curls back on itself and extrapolates back to the origin, forming a 'fly-wing'. Several suggestions have been made to account for this apparent decrease of the superconducting carrier density which occurs despite an increase in the density of normal charge carriers. This behaviour has been attributed by ref. [29] to pair-breaking scattering processes which reduce the effective condensate density. A recent theory by ref. [31] describes the observed behaviour in terms of the Bose-Einstein condensation of a charged Bose gas with

a strongly screened Coulomb repulsion. In this scenario it is the finite extent of the bosons which gives rise to some critical density, above which they become immovable and $T_c \to 0$. An interpolation between the dilute ideal Bose-gas regime and the dense regime gives the required behaviour. It seems clear that these and future μ^+SR measurements will provoke further theoretical ideas which may be important to the detailed understanding of the superconducting state in the HTC materials.
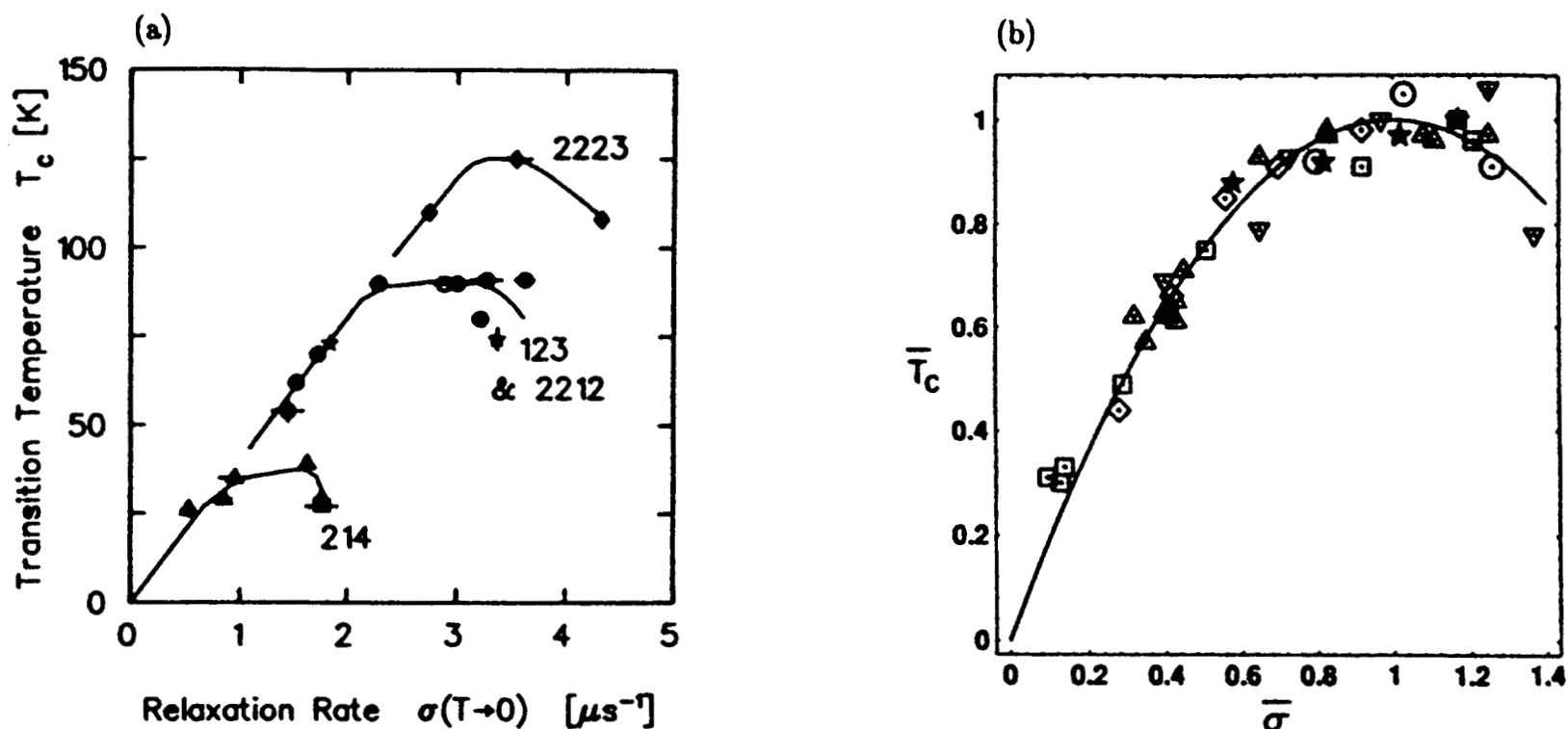

Figure 4: (a) The Uemura plot for various families of HTC superconductors. Details of the data shown may be found in ref. [27]. (b) The data for various families rescaled according to Eq.9. The reader is referred to ref. [26] for details of the materials represented in the plot. Axis symbols are as defined in the text.

5. Microscopic observation of flux-lattice melting

The HTC superconductors have several properties which distinguish them from conventional low-T_c systems: these include a very short coherence lengths ξ, high transition temperature T_c and large anisotropy γ. The combination of these not unrelated properties leads to the possible occurrence of flux-vortex structures in the mixed state other than a regular Abrikosov-lattice, and also of transitions between these phases [3, 32, 33, 34, 19]. In particular the existence of a melting-line $B_m(T)$ in the field-temperature (B-T) phase diagram has been the subject of much experimental effort (see e.g. [7, 35, 36, 37, 38, 39]). Such a transition involves a change from a 'vortex-solid' to a 'vortex-liquid', and is made more likely in HTC materials because (i) high thermal energies are accessible, (ii) the shear modulus c_{66} of the flux solid is made small due to the high value of the Ginzburg-Landau parameter κ and (iii) the high value of the anisotropy parameter γ allows the possibility of enhanced quasi-2D fluctuations [33, 34, 32]. Bulk measurements such as magnetisation and resistivity reveal the presence of an irreversibility-line B_{irr}, below which hysteretic behaviour is observable, and attempts have been made to identify such a line with the microscopic melting-line [37, 38, 39]. However, until recently clear evidence on a *microscopic* scale for vortex melting was not available. As discussed in Section 2, μ^+SR is a very useful probe of the microscopic field distribution $p(B)$ inside the mixed state, and as such may be used to measure changes of vortex structure. μ^+SR measurements have recently

been performed on the single-crystal BSCCO which reveal clear evidence for flux-lattice melting in the region of the irreversibility-line, and are described below [7]. This material was chosen because of its high anisotropy ($\gamma > 100$), which causes the melting-line to occur well below the upper-critical field $H_{c_2}(T)$.
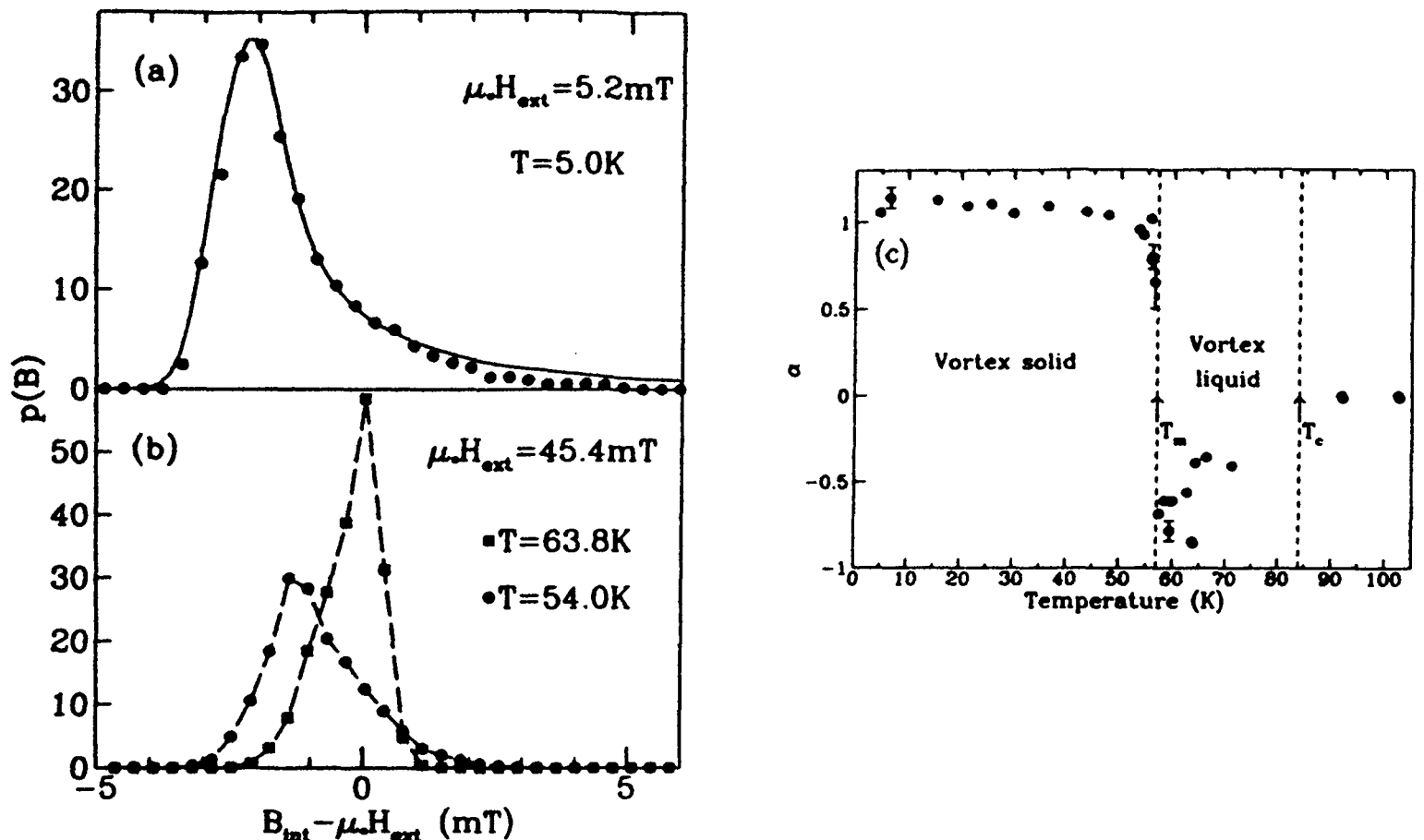

Figure 5: The probability distribution of the internal magnetic fields in $Bi_{2.15}Sr_{1.85}CaCu_2O_{8+\delta}$: (a) At $\mu_o H_{ext}$ =5.2mT and $T = 5.0K$, (b) At $\mu_o H_{ext}$ =45.4mT, for (i) $T = 54.0K$ (circles), (ii) At $T = 63.8K$ (squares), just below and above the irreversibility line respectively [7]. (c) The temperature dependence of the lineshape asymmetry parameter $\alpha = \langle(\Delta B)^3\rangle^{1/3}/\langle(\Delta B)^2\rangle^{1/2}$ (see text) .

In Fig.5(a) is shown the lineshape taken at 5K after field-cooling the BSCCO single-crystals in a field of 50mT. This has the characteristics of a vortex-line lattice, notably the long high-field tail as discussed in Section 2. In Fig.5(b) are shown lineshapes measured at two temperatures after cooling in 45.4mT, one above and one below the irreversibility-line. The lineshape measured below the line again has characteristics of a vortex-line lattice, while that taken above has a completely different probability distribution; in particular, the long high-field tail is no longer present. This latter lineshape cannot be described in terms of a static vortex-line solid, and its features are not incompatible with those of a vortex liquid. Such changes of lineshape may be quantified by defining a parameter derived from the third and second moments of the lineshape $\alpha = (\langle\Delta B^3\rangle)^{1/3}/(\langle\Delta B^2\rangle)^{1/2}$. This is a dimensionless measure of the asymmetry of the distribution, changes of which reflect changes of the vortex structure. This parameter is plotted in Fig. 5(c) as a function of temperature, and shows a clear indication of a sharp transition of the vortex structure. The field dependence of this transition has also been measured and is as expected for the melting of a vortex-line lattice. Furthermore, the melting-line $B_m(T)$ is found to closely coincide with the irreversibility-line $B_{irr}(T)$. These results have also been confirmed by neutron scattering measurements from the vortex-lattice [35]. However, the μ^+SR results are unique in being able to provide information about the vortex structure within the liquid phase, where the neutron signal becomes unobservable due to the lack of long range order.

8

6. Summary

The μ^+SR technique is a unique probe of the probability distribution $p(B)$ of the internal magnetic fields in the mixed state of a type-II superconductor. Measurements of the second moment $\langle(\Delta B)^2\rangle$ of $p(B)$ can be used to measure the penetration depth λ in HTC systems, provided care is taken in the interpretation of the data. The temperature dependence of λ may yield information concerning the symmetry and strength of the superconducting pairs, while the observation of universal trends in λ within and between families of HTC materials may also provide important information concerning the microscopic behaviour. The measurement of $p(B)$ can also be used to gain information about the microscopic vortex structure in the mixed state, and of flux-vortex phase transitions. Among other things this has recently been used to observe flux-lattice melting in BSCCO.

Although restrictions of space have allowed only a rather narrow review of the applications of μ^+SR to HTC research, I hope that I have been able give some impression of the importance of the technique to this field. It seems certain that in future μ^+SR research will continue to play a key role in this area.

Acknowledgements

References

[1] See e.g. Muon Spin Rotation Spectroscopy: Principles and Applications in Solid State Physics (Adam Hilger, Bristol 1985).

[2] See e.g. Proceedings of the 5th International Conference on Muon Spin Rotation, Relaxation and Resonance, Oxford, U.K., Hyperfine Interactions **63-65** (1990).

[3] D.S. Fisher, M.P.A. Fisher and D.A. Huse, Phys. Rev. B **43**, 130 (1991).

[4] M. Tinkham, Introduction to Superconductivity (McGraw-Hill, New York 1975).

[5] E.H. Brandt, J. Low. Temp. Phys., **73**, 355 (1988).

[6] D. Herlach *et al.*, Hyperfine Interactions **63**, 41 (1990).

[7] S.L. Lee *et al.*, Phys. Rev. Lett. **71**, 3862 (1993).

[8] J. Rammer, Europhys. Lett. **5**, 77 (1988).

[9] J. Annett, N. Goldenfeld and S.R. Renn, Phys. Rev. B **43**, 2778 (1991).

[10] P. Pincus *et al.*, Physics Letters **13**, 21 (1964).

[11] E.H. Brandt, Phys. Rev. B **37**, 2349 (1988).

[12] W. Barford and J.M.F. Gunn, Physica C **156**, 515 (1988).

[13] S.L. Thiemann, Z. Radović and V.G. Kogan, Phys. Rev. B **39**, 11406 (1989).

[14] E.M. Forgan *et al.*, Hyperfine Interactions **63**, 71 (1990).

[15] V.I. Fesenko, V.N. Gorbunov and V.P. Smilga, Physica C **176**, 551 (1991).

[16] R. Cubitt *et al.*, Physica C **213**, 126 (1993).

[17] M. Weber *et al.*, Phys. Rev. B **48**, 13022 (1993).

[18] Y.-Q. Song *et al.*, Phys. Rev. Lett. **70**, 3127 (1993).

[19] J.R. Clem, Phys. Rev. **43**, 7837 (1991).

[20] E.H. Brandt, Phys. Rev. Lett. **66**, 3213 (1991).

[21] D.R. Harshman *et al.*, Phys. Rev. B **47**, 2905 (1993).

[22] D.R. Harshman *et al.*, Phys. Rev. Lett. **67**, 3152 (1991).

[23] B. Pümpin *et al.*, Journal of the Less-Common Metals **164** & **165**, 994 (1990).

[24] H. Keller *et al.*, Physica C **185-189** 1089 (1991).

[25] P. Zimmermann *et al.*, Physik-Institut der Universität Zürich, Private communication (1993).

[26] T. Schneider and H. Keller, Phys. Rev. Lett. **69**, 3374 (1992).

[27] Y.J. Uemura *et al.*, Phys. Rev. Lett. **62**, 2317 (1989); Y.J. Uemura *et al.*, Phys. Rev. B **38**, 909 (1988); Y.J. Uemura *et al.*, Phys. Rev. Lett. **66**, 2665 (1991).

[28] T. Schneider and H. Keller, Physica C **207**, 366 (1993).

[29] Ch. Niedermayer *et al.*, Phys. Rev. Lett. **71**, 1764 (1993).

[30] Y.J. Uemura *et al.*, Nature **364**, 605 (1993).

[31] T. Schneider and M.H. Pedersen, submitted for publication (1993).

[32] A. Houghton, R.A. Pelcovits, and A. Sudbø, Phys. Rev. B **40**, 6763 (1990).

[33] E.H. Brandt, Phys. Rev. Lett. **63**, 1106 (1989).

[34] L.I. Glazman and A.E. Koshelev, Phys. Rev. B **43**, 2835 (1991).

[35] R. Cubitt *et al.*, Nature **365**, 407 (1993).

[36] R.G. Beck *et al.*, Phys. Rev. Lett. **68**, 1594 (1992).

[37] H. Safar *et al.*, Phys. Rev. Lett. **70**, 3800 (1993).

[38] A. Schilling *et al.*, Phys. Rev. Lett. **71**, 1899 (1993).

[39] P.L. Gammel *et al.*, Phys. Rev. Lett. **61**, 1666 (1988).

MUONIUM STATES IN CRYSTALLINE AND AMORPHOUS SEMICONDUCTORS: RELATIONSHIP TO HYDROGEN CENTRES

E A Davis, Department of Physics and Astronomy, University of Leicester, Leicester LE1 7RH, U.K.

Handouts

1. Properties of muon and muonium; precessional frequencies
2. TF MuSR spectra; hyperfine constants
3. Muonium states in silicon
4. Bond-centre muonium
5. Breit-Rabi diagrams for Mu' and Mu^*
6. Diamagnetic fractions and relaxation rates versus T
7. LF repolarisation
8. Meier cusp for Mu^*; theory
9. Repolarisation curves for pcr-Si and a-Si
10. Experimental results for a-Si; MuSR (rotation, resonance and repolarisation)
11. Sites for Mu or H in silicon
12. Energies of Mu and H states. Passivation complexes

	Muon μ^+	**Muonium $\mu^+ e^-$**
mass	$206.7\ m_e = 0.113\ m_p$	
reduced mass		$0.995\ m_e$
g.s. radius		0.532 Å
g.s. binding energy		13.54 eV
spin	$1/2$	0 or 1
magnetic moment $\mu = e\hbar/2m$	4.49×10^{-26} J T^{-1} $= \mu_B/206.7$	
gyromagnetic ratio $\gamma = g\mu/\hbar = ge/2m$	135.5 MHz T^{-1} $= 13.55$ kHz G^{-1}	13.94 GHz T^{-1} $= 1.394$ MHz G^{-1}
hyperfine frequency		4.463 GHz

Diamagnetic muonium

ω (Larmor Precession)
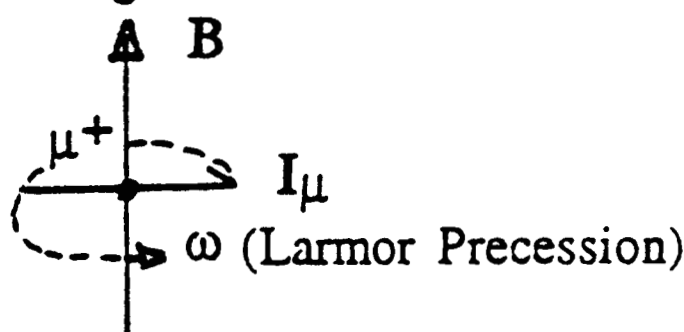
Paramagnetic Muonium
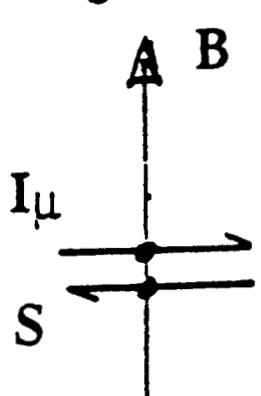
The precession may be rep. by the energy-level diag. of a spin 1/2 system:

E/h

$\Delta E/\hbar = \omega = \gamma_\mu B$

B
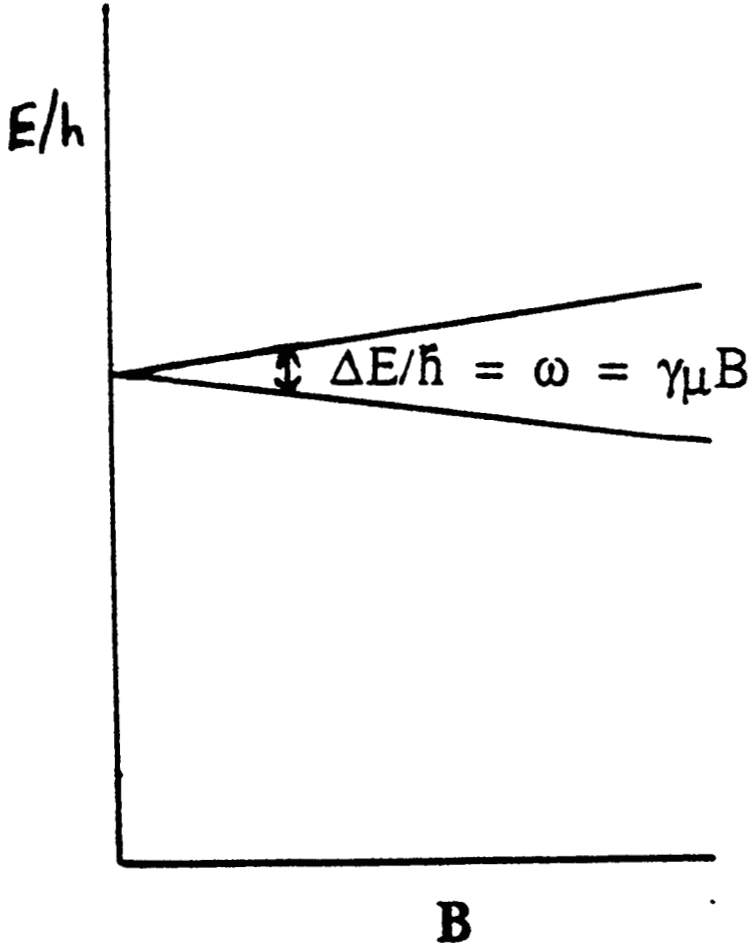
Measured frequencies rep. by e-level diag. of spin 0,1 system (Breit-Rabi Diagram)

E/h

$(\uparrow\uparrow)$

$\frac{1}{\sqrt{2}}(\uparrow\downarrow + \downarrow\uparrow)$

$(\downarrow\downarrow)$

$\frac{1}{\sqrt{2}}(\uparrow\downarrow - \downarrow\uparrow)$

B
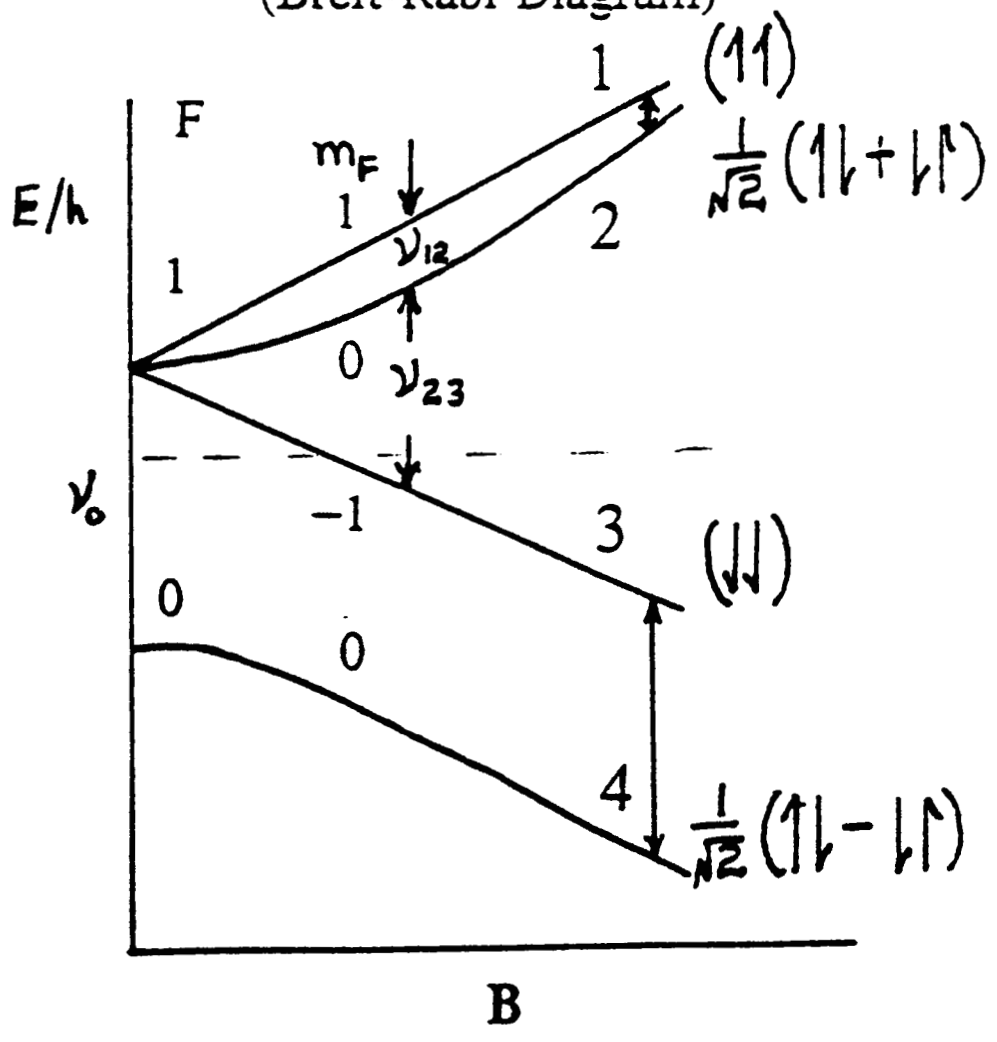
The energy e-states are solutions to S.Eqn. with the <u>spin hamiltonian</u>

$$H = g_e\mu_e B.S - g_\mu\mu_\mu B.I + S.A.I$$
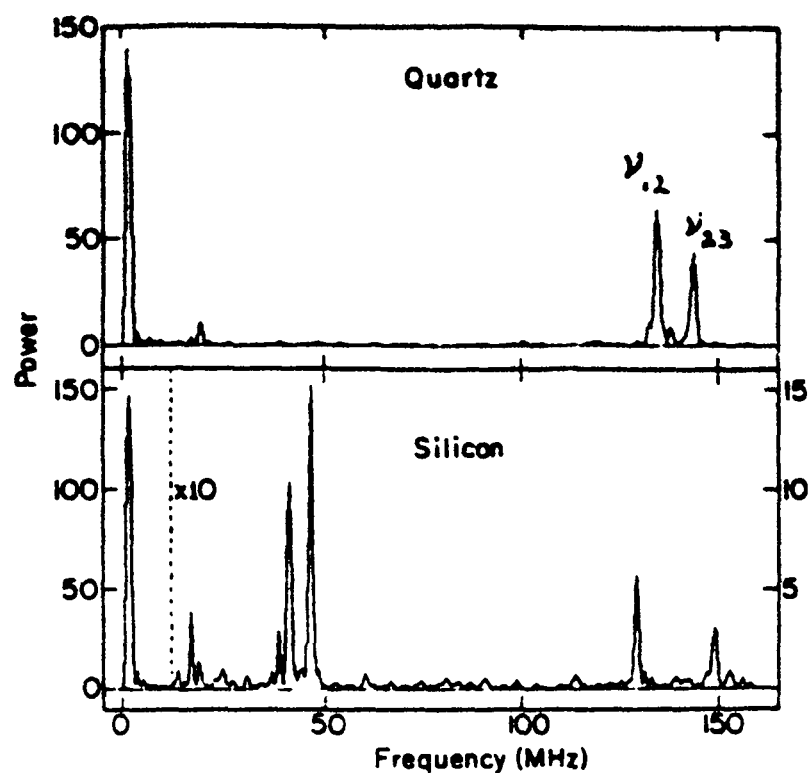
FIG. 26. Transverse-field μSR frequency spectra taken at 10 mT in quartz at room temperature and [111] Si at 77 K showing the precession components from diamagnetic μ^+ ($v_{\mu^+} = 1.36$ MHz) and isotropic Mu (the pair v_{12} and v_{23} centered on 140 MHz). Note the larger Mu splitting in Si, indicating a weaker hyperfine interaction and the presence in Si but not in quartz of Mu* precession lines (v_{12} and v_{34}, $\theta = 70.5^\circ$, at 41 and 46 MHz). From Brewer et al. (1973).
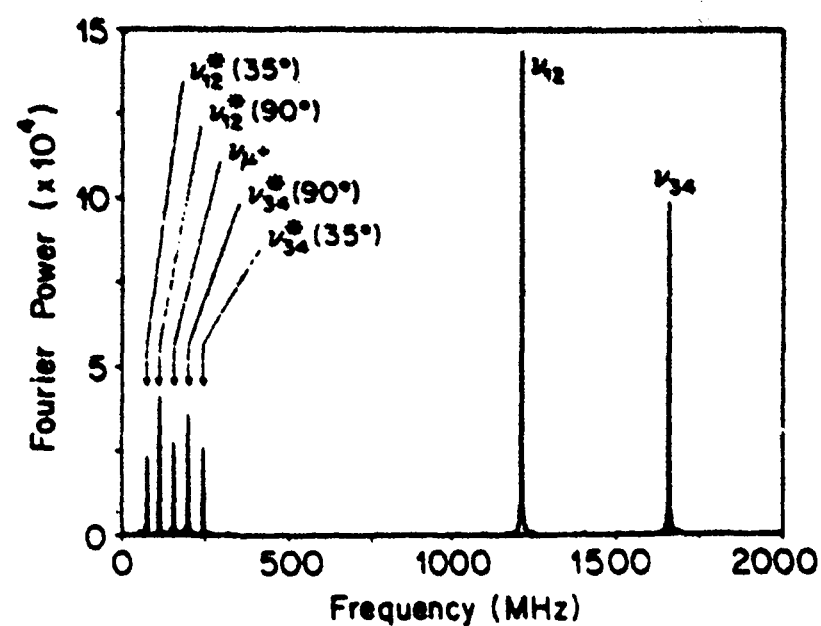
FIG. 29. A μSR frequency spectra taken with the high-field, high-time-resolution apparatus in high-resistivity GaAs at 10 K with a 1.15-T field applied along the [110] axis. Note the two Mu lines v_{12} and v_{34}, the Mu* lines $v_{\parallel}^*(\theta)$ (θ is the angle between the [111] Mu* symmetry axis and the applied field), and the diamagnetic muon line v_{μ^+}. From Kiefl et al. (1985).

B D Patterson Rev. Mod. Phys. 60 (1988) 69
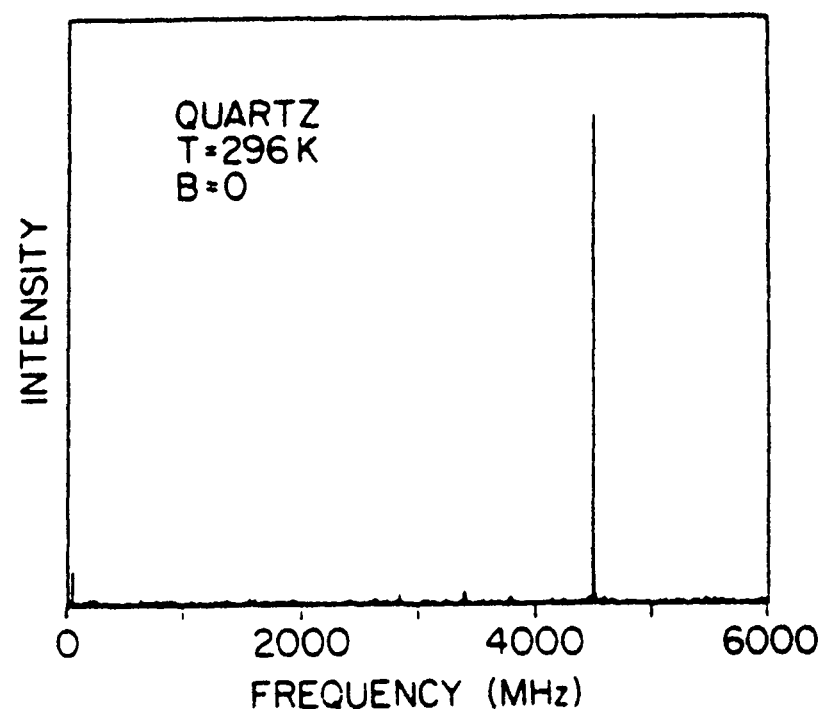
FIG. 27. A zero-field μSR spectrum of quartz at room temperature. The Mu hyperfine frequency is close to the vacuum value ($\omega_0 = 2\pi 4.463$ GHz). The FWHM time resolution is $\delta t = 110$ ps. From Holzschuh et al. (1981b).

S F J Cox J. Phys. C Solid State Physics 20 (1987) 3187

Hyperfine constant for interstitial muonium in semiconductors and dielectrics
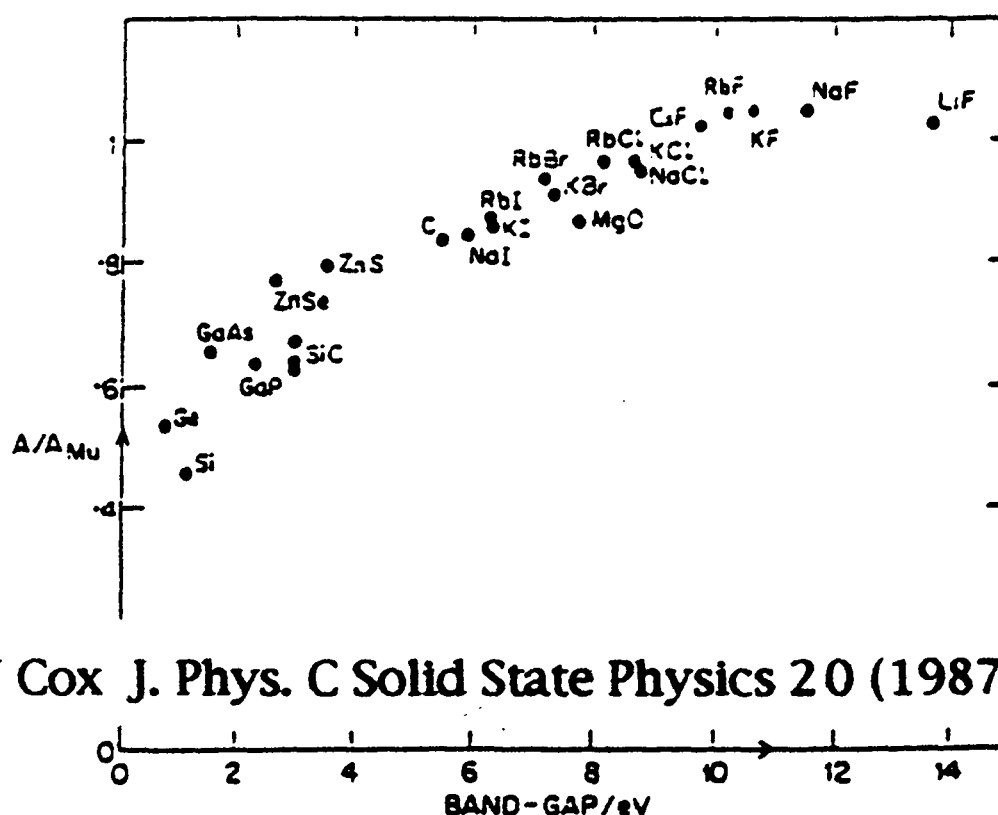
MUONIUM STATES IN SILICON

Possible sites in Si

What are Mu', Mu* and diamagnetic Mu?
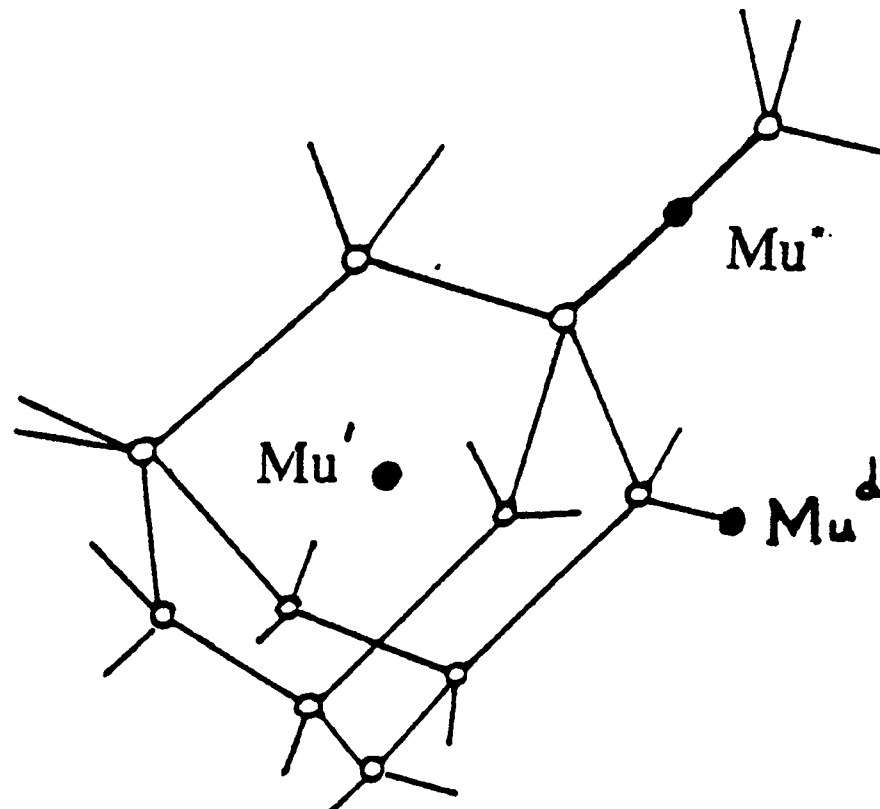
Paramagnetic sites: Mu', Mu*(=MuBC) ;

Diamagnetic sites: Si - Mu, Mu⁻, (Mu*)⁺, etc.

Mu' - μ^+e^- coupling constant A indep of θ - isotropic Mu

Mu*- coupling constant A strongly dependent on θ

- A has to be rep. by a tensor, called the hyperfine tensor

- usually this is just a traceless diagonal matrix left and right multiplied by the spin vectors I and S in the Spin Hamiltonian; for Mu*, A has 2 components

$$H = g_e\mu_e B.S - g_\mu\mu_\mu B.I + A_\parallel I_z S_z + A_\perp(I_x S_x + I_y S_y)$$

Zeeman interactions   Hyperfine interactions

The relative abundances of the possible states must follow the sum rule:

diamagnetic fraction(f_d) + Mu' fraction ($f_{Mu'}$) + Mu* fraction (f_{Mu*}) = 1

$Si(sp^3)$

$(+-)$

$(+-+)$

$(+0-)$

Mu or H $(1s)$

$(++)$

$(+++)$

ADDS 0, 1, OR 2 ELECTRONS!

WAVEFUNCTIONS:

$(+-+)$

$(+0-)$

$(+++)$

see   S F J Cox and M J R Symons Chem. Phys. Lett. 126 (1988) 516
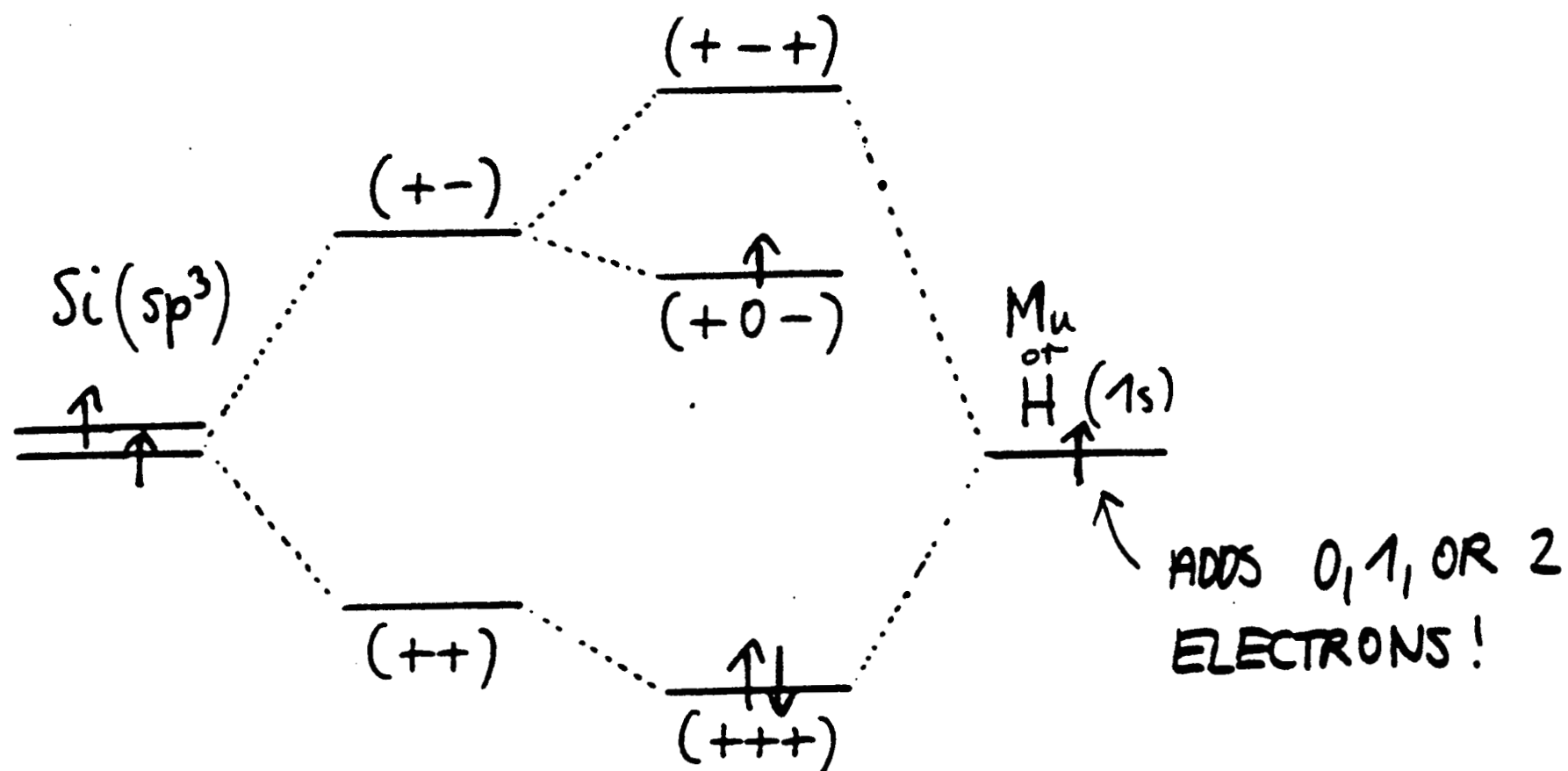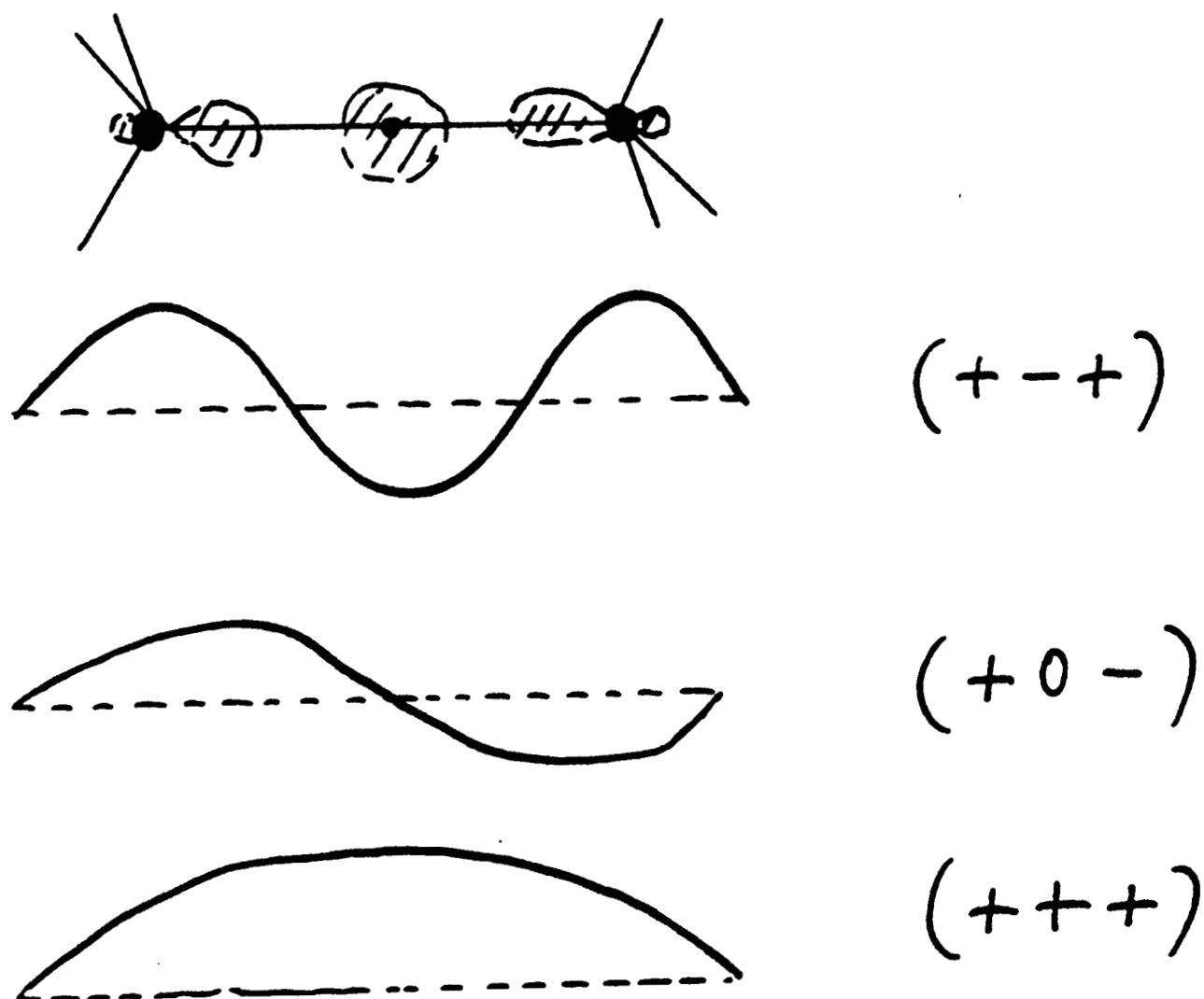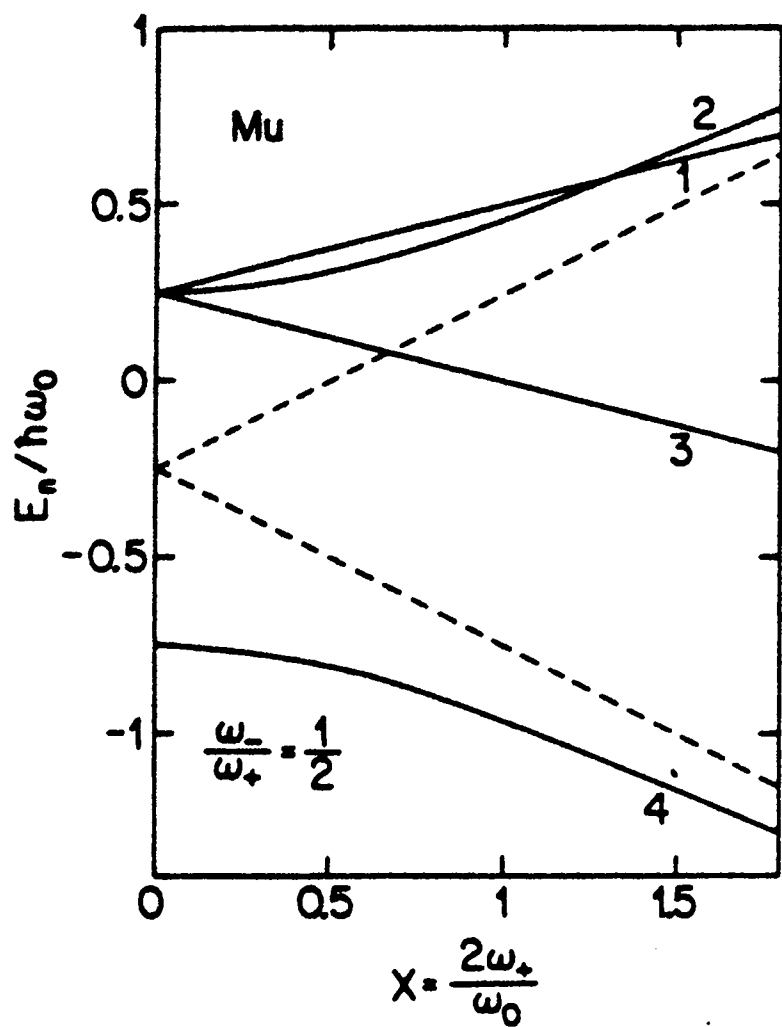
FIG. 1. The hyperfine energy-level (Breit-Rabi) diagram for isotropic 1s-Mu as a function of the dimensionless magnetic field $x = B(g_\mu\mu_\mu - g_e\mu_B)/(hA)$. A fictitious value for the quantity ω_-/ω_- has been used for clarity; its true value is 0.9904. The dashed lines are the high-field asymptotes for levels 2 and 4.
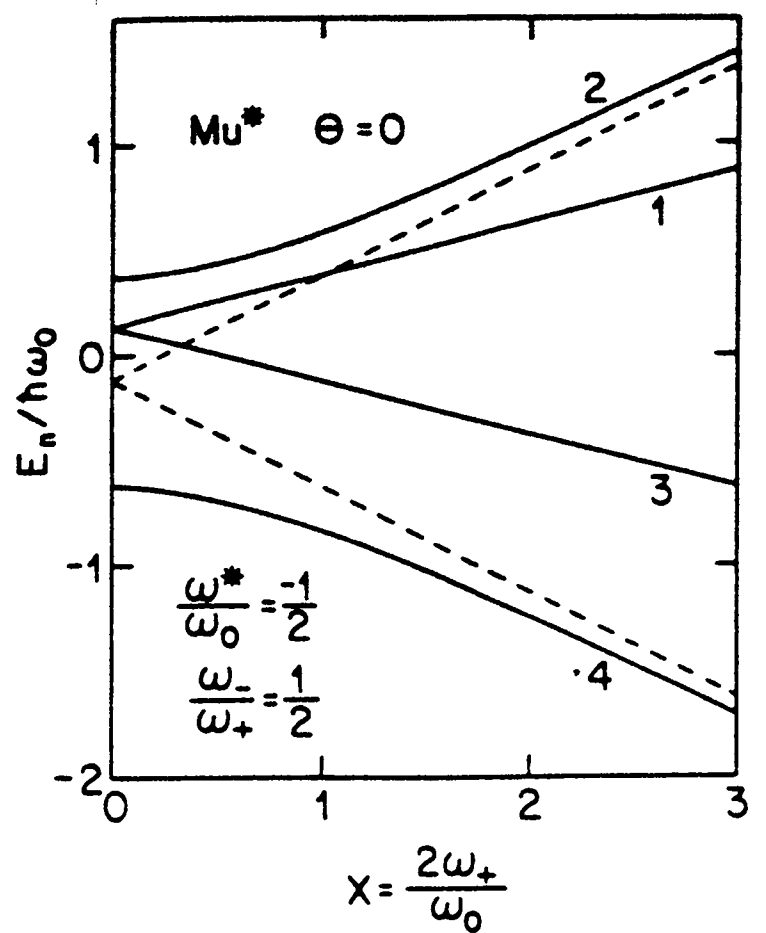
FIG. 2. The hyperfine energy-level diagram for anisotropic Mu* for the case $\theta = 0$ ([111] symmetry axis parallel to the applied field). Fictitious values of both ω^*/ω_0 and ω_-/ω_- have been assumed. The dashed lines are the high-field asymptotes for levels 2 and 4.
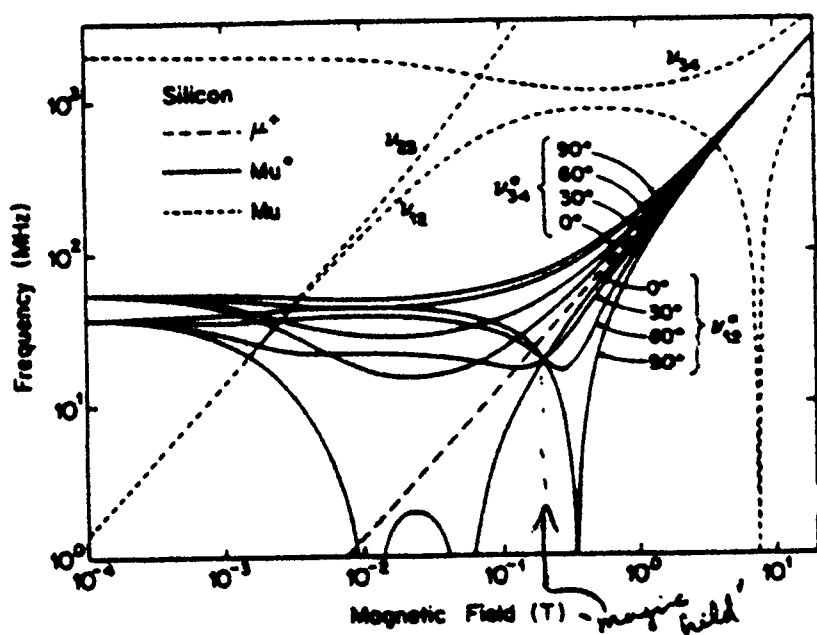
FIG. 5. A log-log plot of the observed transverse-field precession frequencies for the three muon states in silicon. The angles given refer to θ, the angle between the applied field and the Mu* symmetry axis.
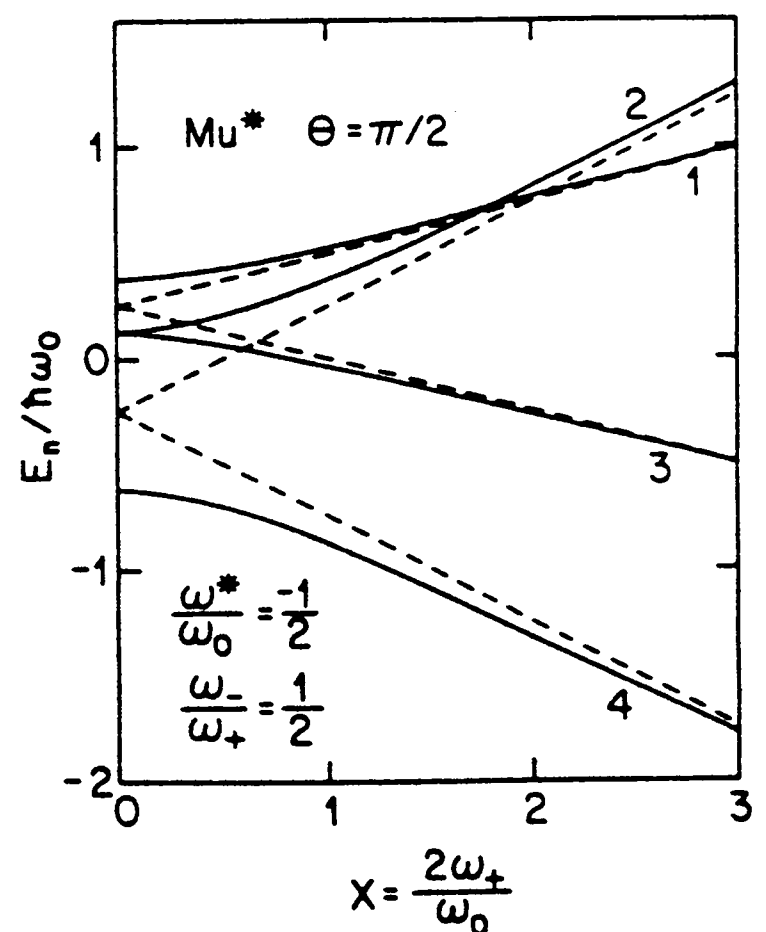
FIG. 3. The hyperfine energy-level diagram for anisotropic Mu* for the case $\theta = \pi/2$ ([111] symmetry axis perpendicular to the applied field). The dashed lines are high-field asymptotes.
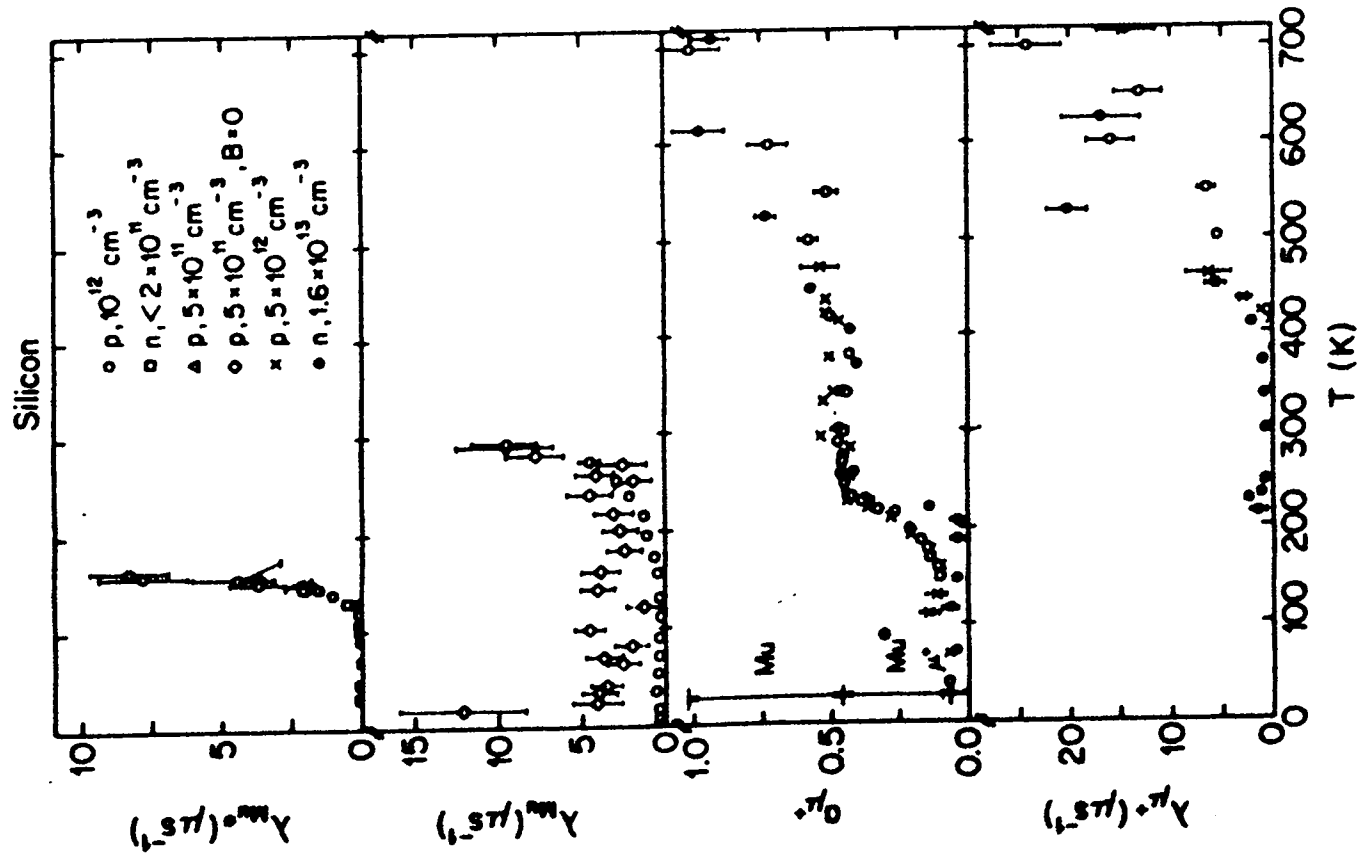
Silicon

○ p,10^{12} cm^{-3}
□ n,<2×10^{11} cm^{-3}
▲ p,5×10^{11} cm^{-3}
◇ p,5×10^{11} cm^{-3}, B○O
× p,5×10^{12} cm^{-3}
● n,1.6×10^{13} cm^{-3}

Germanium

□ <1.5×10^{10} cm^{-3}
▲ <4×10^{10} cm^{-3}
◇ p,2.2×10^{11} cm^{-3}
× p,10^{14} cm^{-3}
● n,10^{14} cm^{-3}

GaAs

○ high resistivity
▲ 4×10^{16} cm^{-3}
□ p,2×10^{12} cm^{-3}

FIG. 67. Collected data on the temperature-dependent dynamics of muon states in high-purity silicon. The indicated low-temperature muon state fractions in the a_{μ^+} panel are from Table VIII. References for the individual data sets are given in Table XV.
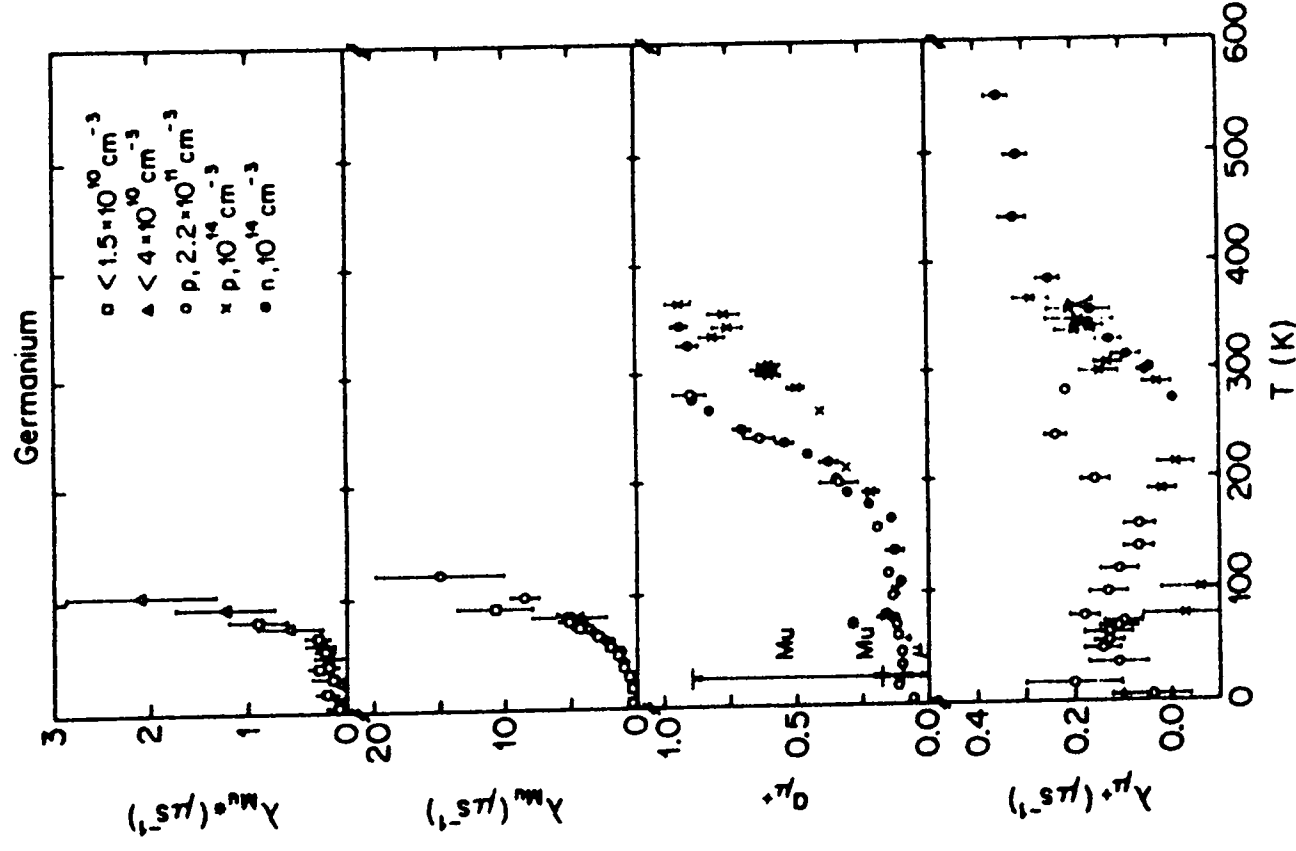
FIG. 75. Collected data on the temperature-dependent dynamics of muon states in high-purity germanium. The indicated low-temperature muon state fractions in the a_{μ^+} panel are from Table VIII. References for the individual data sets are given in Table XVIII.
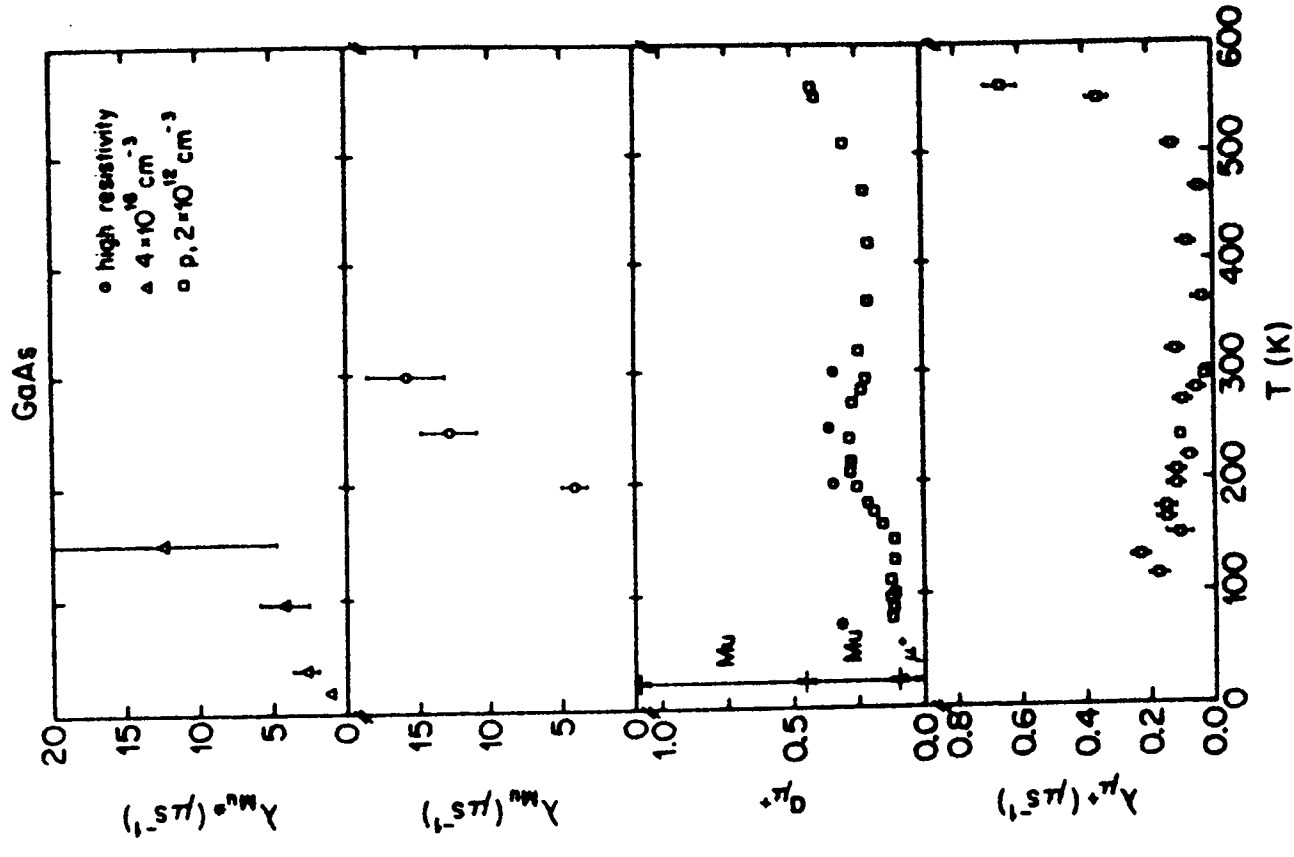
FIG. 83. Collected data on the temperature-dependent dynamics of muon states in GaAs. The indicated low-temperature muon state fractions in the a_{μ^+} panel are from Table VIII. The "high-resistivity" and 4×10^{16} cm^{-3} doped samples were measured at 1.1 T by the Zurich group (unpublished), and the 2×10^{12} cm^{-3} p-doped data were taken at 28 mT by Barsov et al. (1985).

Decoupling or Repolarization Technique

Here applied field is longitudinal to the I_μ direction.

S

I_μ

⟶ B
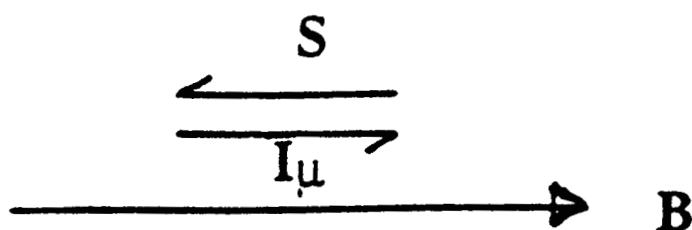
- field decouples the μ^+e^- coupling (the hyperfine coupling)
- plot of initial asymmetry (a_0) (= a measure of muon polarization) - vs field yields <u>decoupling curves.</u>
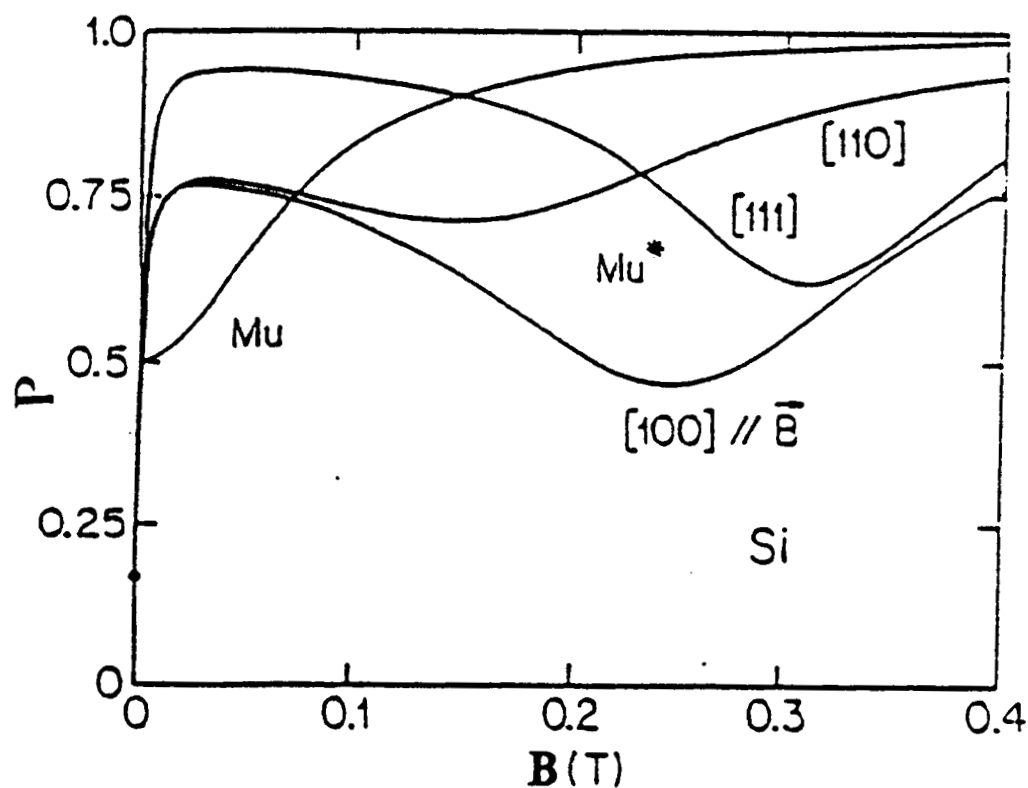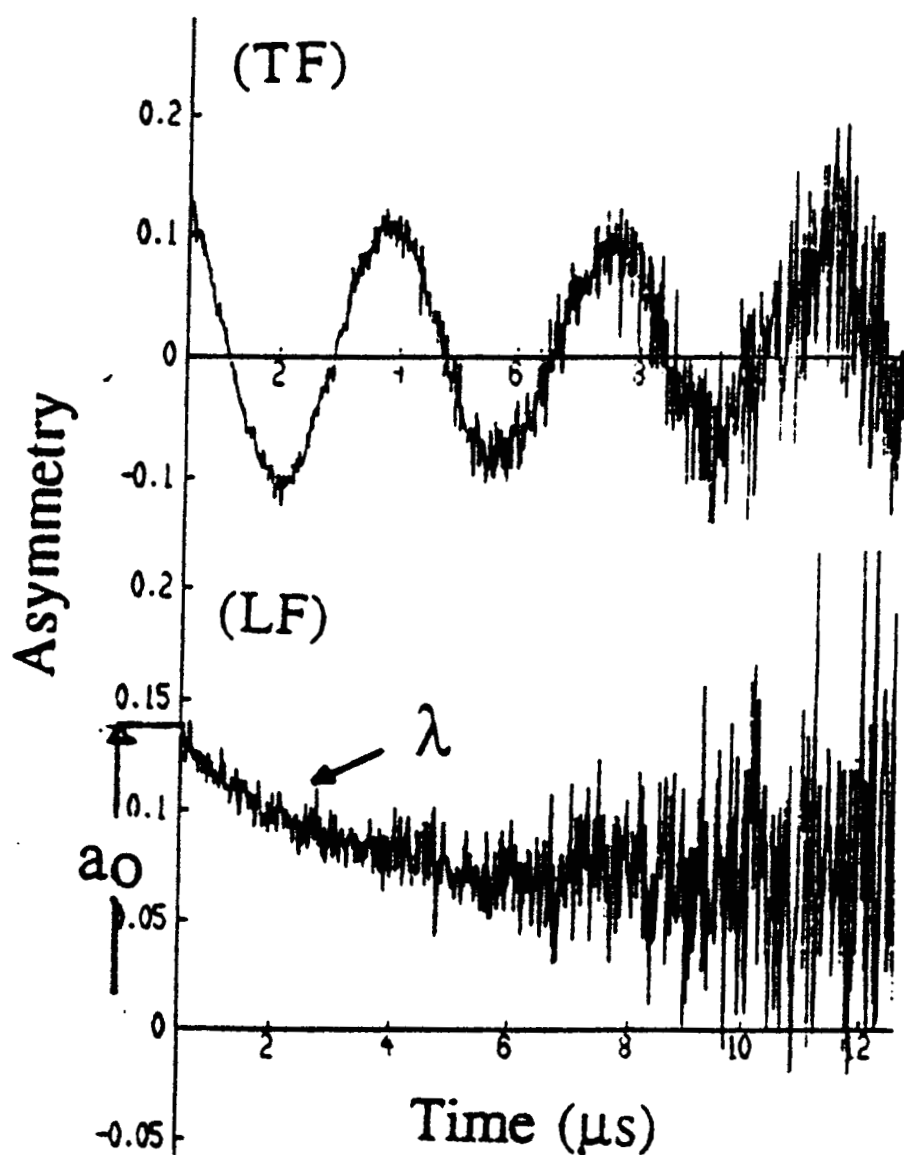
- shape of decoupling curves det. by amount (fraction) of each centre, and its environment (which affects the hf coupling).

TO SUMMARIZE: We implant muons in sample, and measure a_0, v, λ in TF or LF configuration. This tells us (i) **what states are being measured;** (ii) **how much of each there is (i.e. their fractions); (iii) what their environments are; etc., etc., etc.**

S1 REPOL- VARYING mu* FRACTION
Fd = 0.10

S1 REPOL- VARYING Bmu
Fd= 0.10
Fmust = 0.00

Field (Gauss)

Computed by A Singh and F Pratt

Mu^*

[110]
[111]
Mu^*
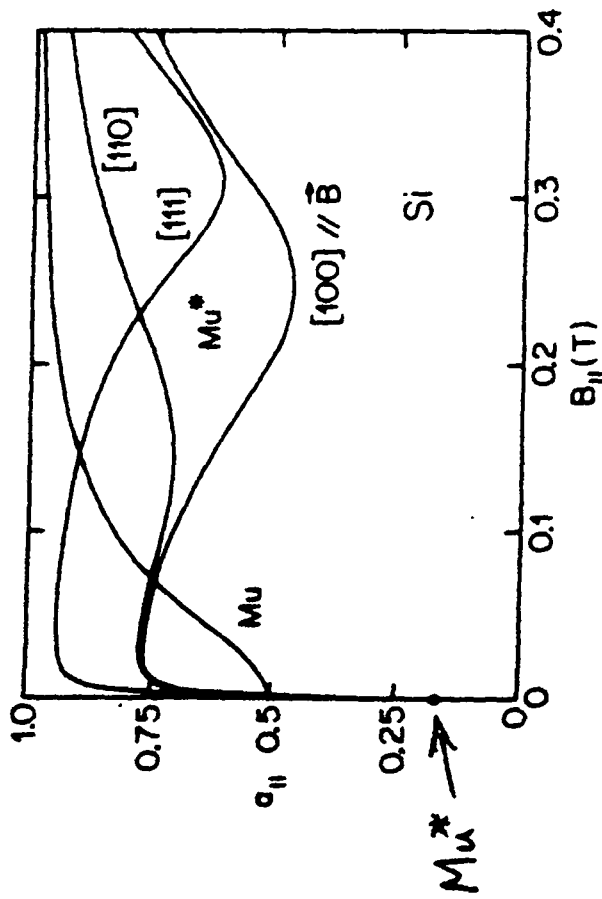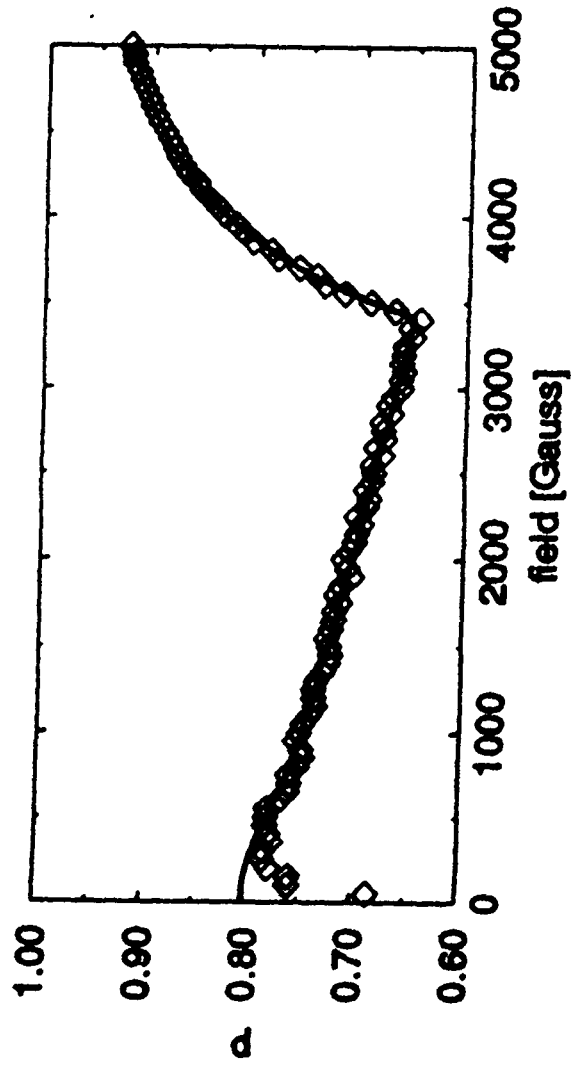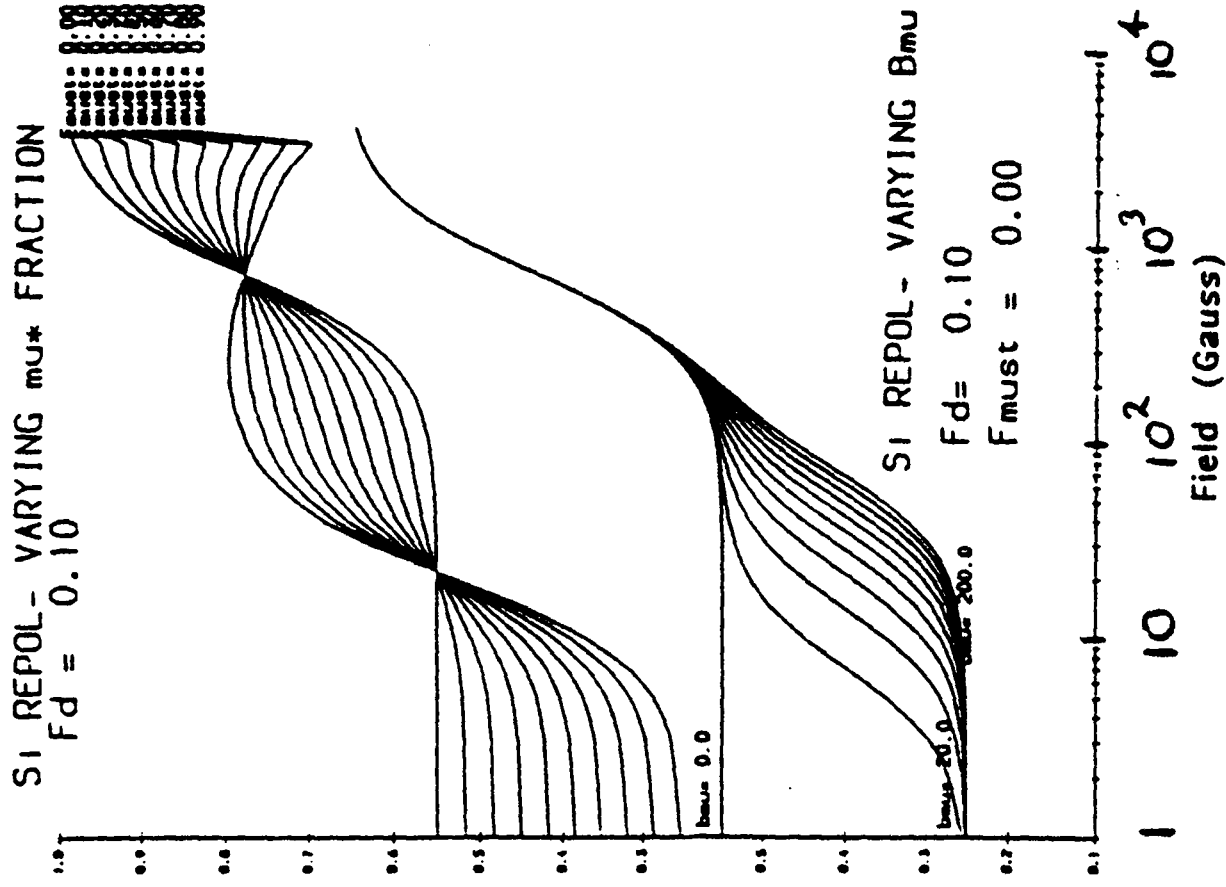[100] // $\vec{B}$
Si
Mu
$a_{\parallel}$
$B_{\parallel}(T)$

FIG. 22. Longitudinal-field quenching curves $a_{\parallel}(B_{\parallel})$ for isotropic Mu and Mu* in silicon. The results for Mu* are averaged over the four possible [111] symmetry axes.
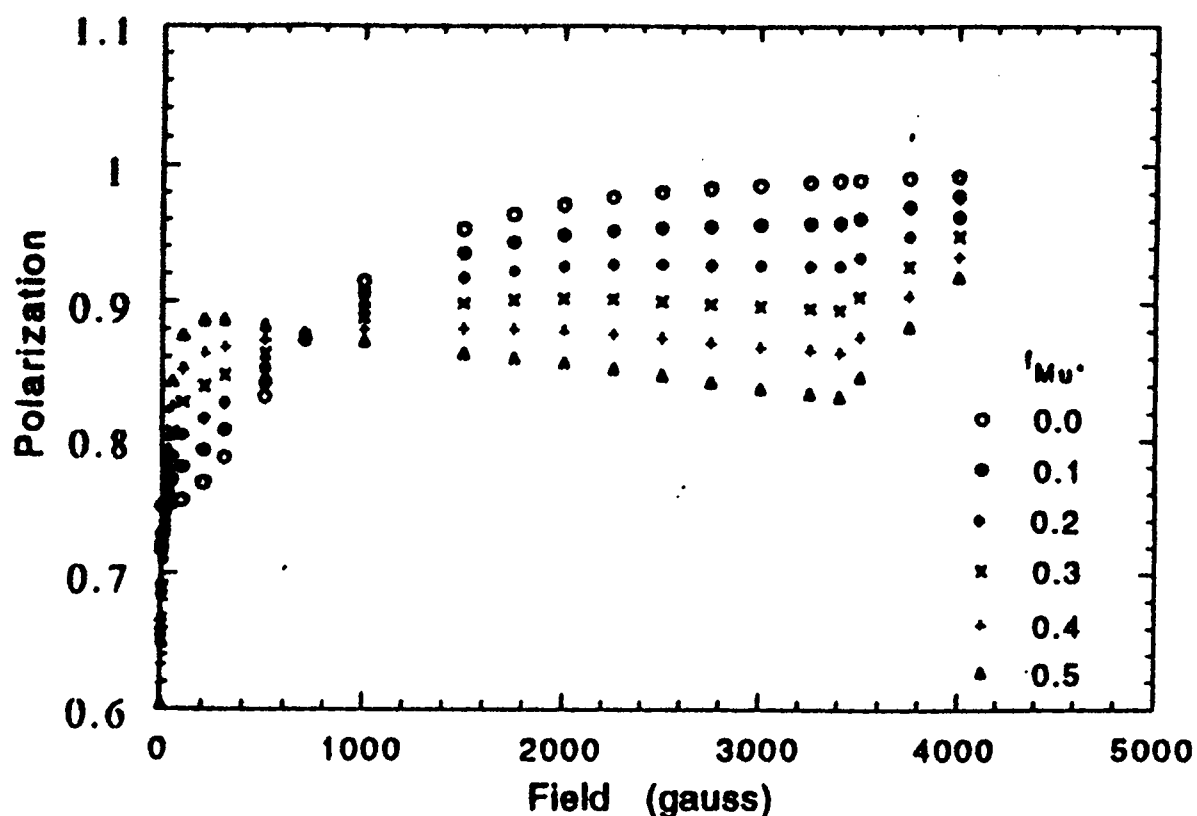
Rev. Mod. Phys. Vol. 60. No. 1, January 1988

field [Gauss]

p

Longitudinal polarisation vs field for polycrystalline silicon calculated with the full spin Hamiltonian (Eq. (1)). The solid line is the approximated result (p).

P Meier, D W Cooke et al (to be published)

Family of theoretical repolarisation curves with a constant diamagnetic contribution of 0.5 but various relative fractions of Mu. The remaining fraction is associated with Mu'.*
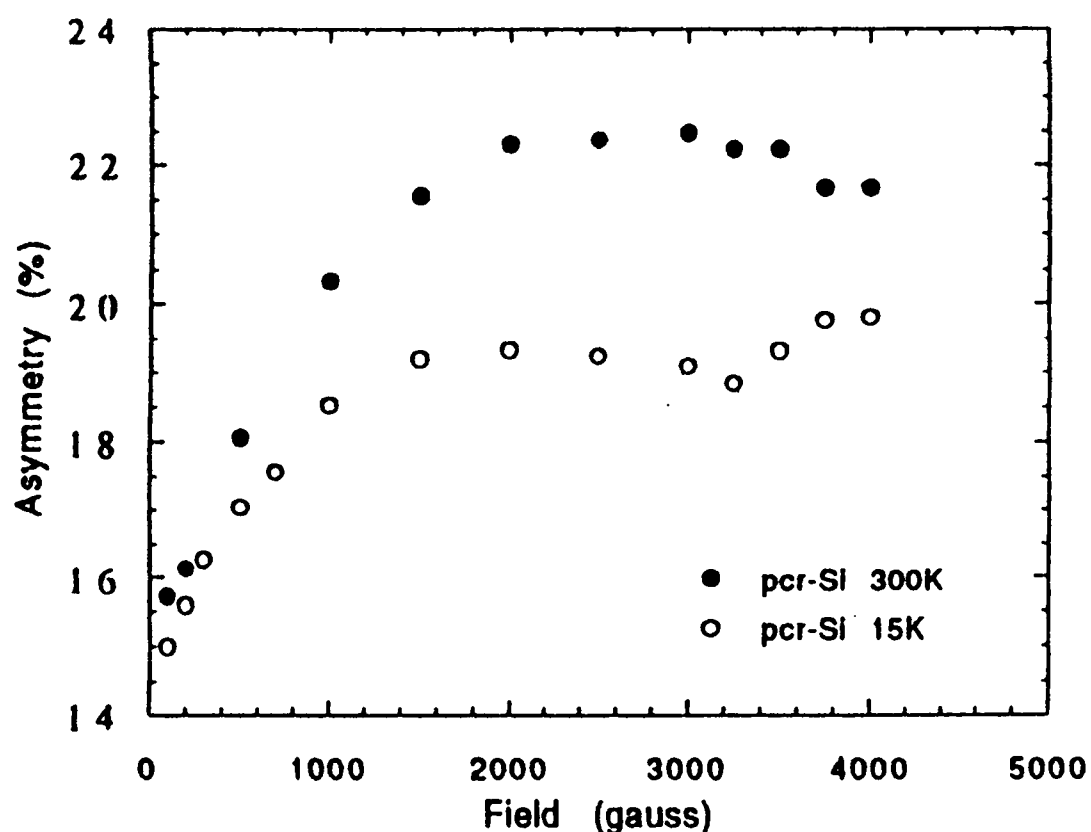
Repolarisation curves for polycrystalline Si. The asymmetry between forward and backward count rates is used as a measure of the polarisation. The cusp at about 3400 gauss in the curve obtained at 15K is associated with Mu. It is not present at 300K owing to ionisation of Mu* to the diamagnetic state.*
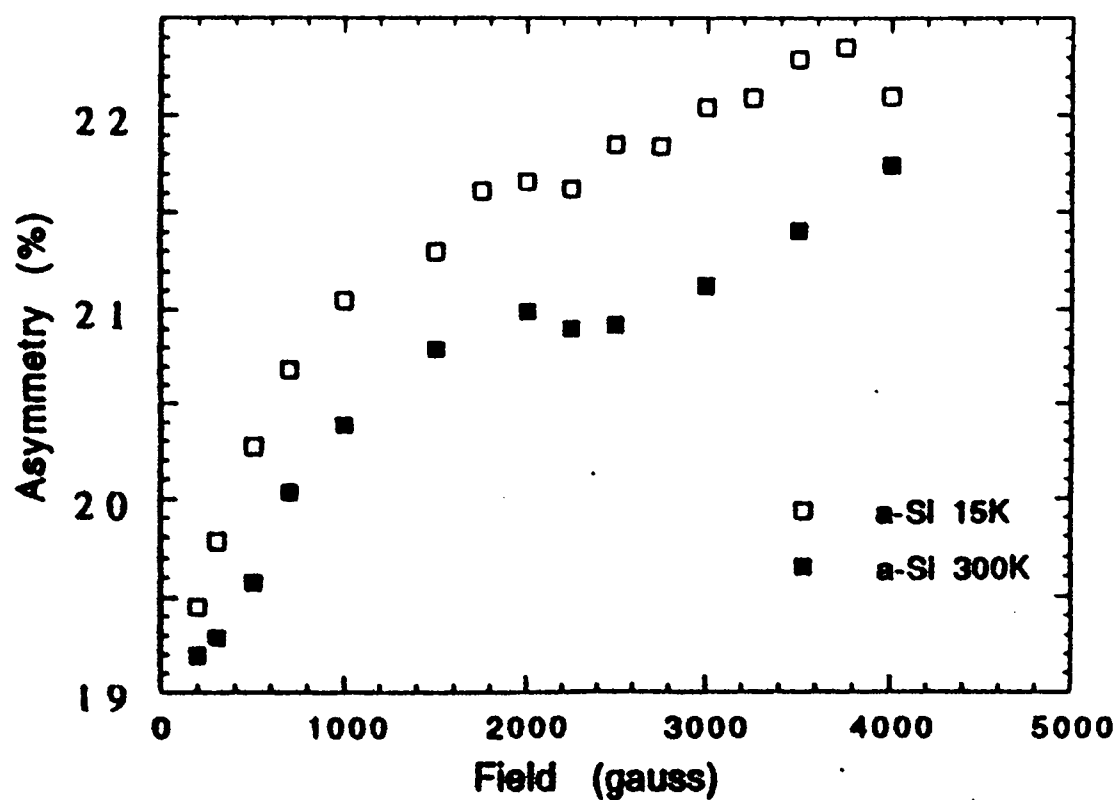
Repolarisation curves for amorphous Si. The minimum occurs at a lower field than in pcr-Si and is present at both 15K and 300K, suggesting different parameters and a greater stability of Mu.*
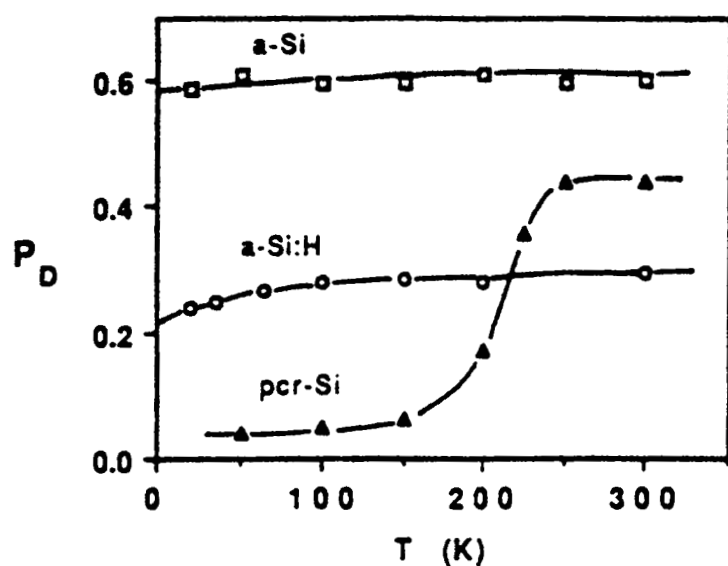
E A Davis, A Singh and S F J Cox (unpublished)

FIGURE 1
Diamagnetic fraction P_D versus temp-
erature for pcr-Si, a-Si:H (reference 5)
and a-Si (this work) determined from the
amplitude of the precession signal in
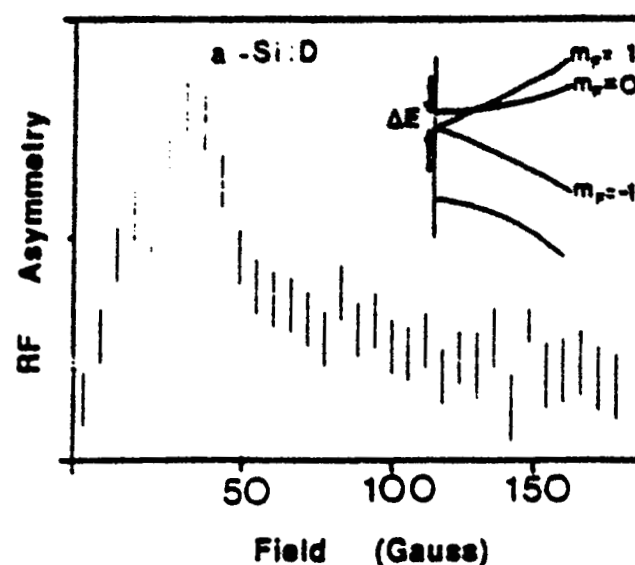muon spin rotation experiments.

FIGURE 2
Muon spin resonance spectrum of a-Si:D
(chosen rather than a-Si:H to avoid
nuclear depolarising fields associated with
hydrogen). The frequency of the r.f. field
was 56 MHz and the temperature was 50K.
The breadth and asymmetric tail suggests
a distribution of zero-field energy splittings
ΔE in the muonium triplet levels as indicated
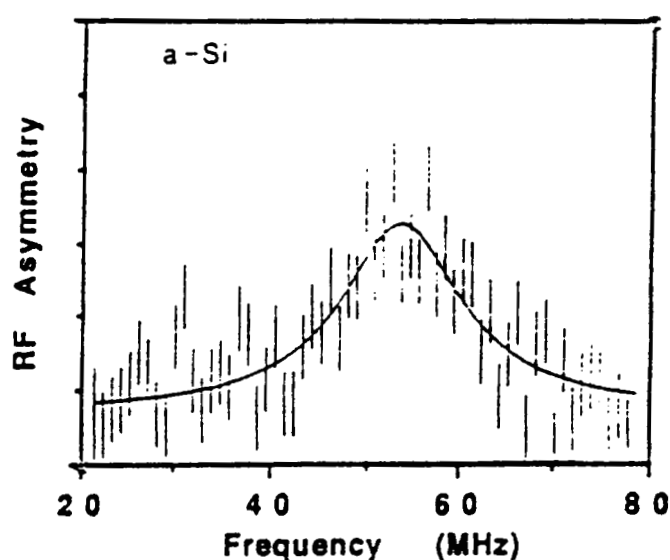in the inset.

FIGURE 3
Muon spin resonance spectrum of un-
hydrogenated a-Si. The magnetic field
was 40G and the temperature was 20K.

FIGURE 4
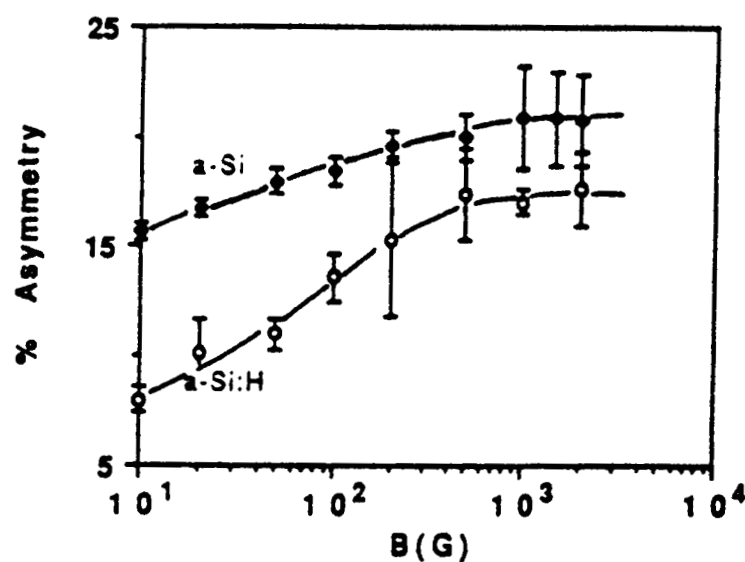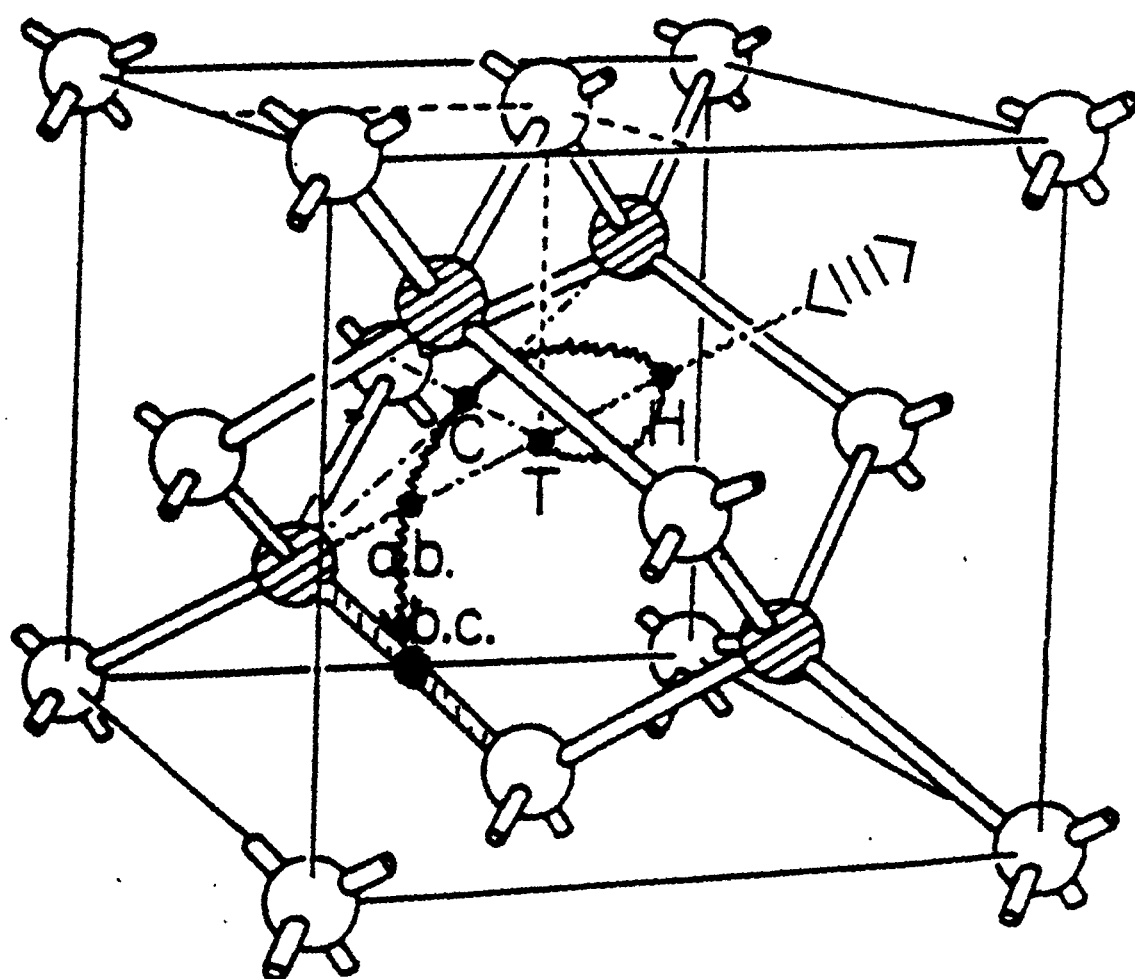Muon repolarisation or decoupling curves
for a-Si:H (reference 5) and a:Si (this work).
Full recovery of the polarisation would
correspond to approximately 23% on the
scale shown.

⟶ THEORIE
SEIT
1970

⟨111⟩

H

T

C

d.b.

b.c.

M Stutzmann (private communication)

$$E_C$$

$$H^+ \Rightarrow BC$$

$$H^0 \Rightarrow BC$$

NEGATIVE u^*

$$H^- \Rightarrow T$$

$$E_V$$

$$H^0 \Rightarrow DB$$

DB

T

BC
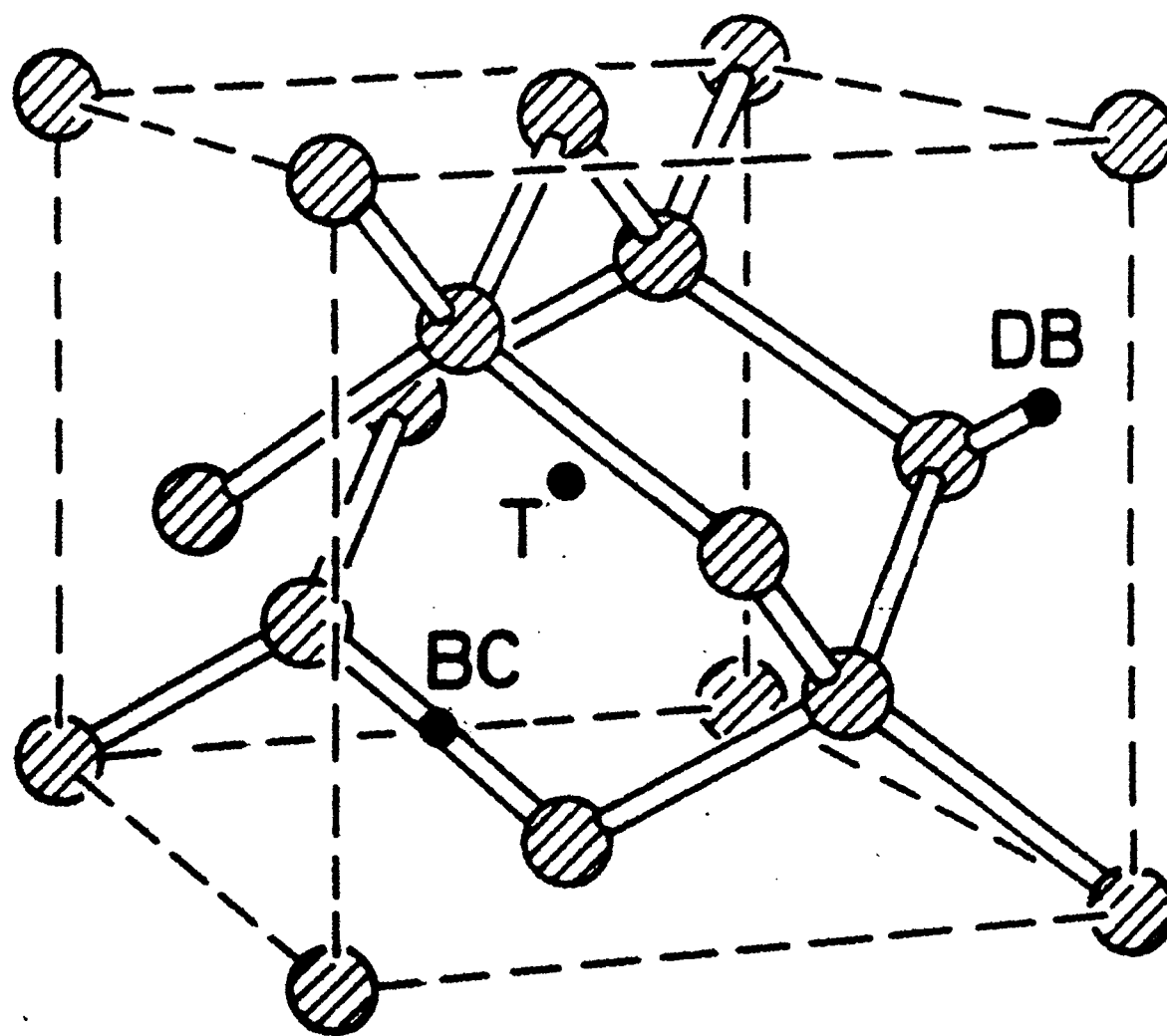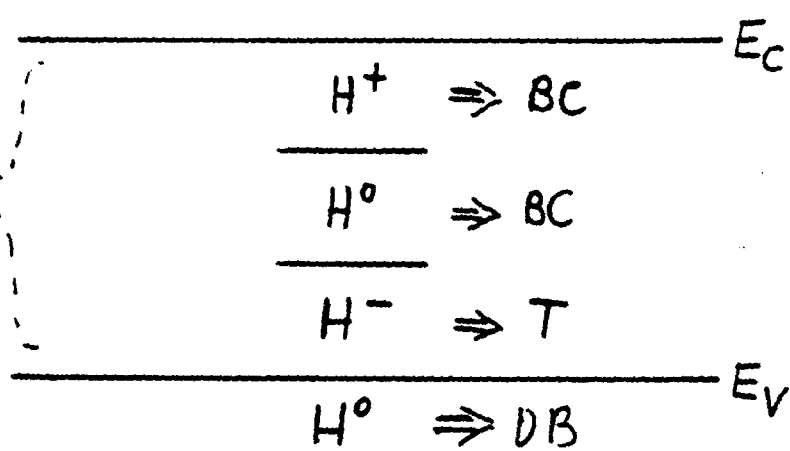
Energy levels associated with hydrogen or muonium

Passivation of an acceptor (a) and donor (b) in silicon by Mu(H). In each case the bonds formed by Mu(H) destroy the four-fold coordination of the dopant, thereby removing its level from the gap.

MUON SITES AND ELECTRONIC STRUCTURE

Steve Cox

ISIS Pulsed Muon Facility, Rutherford Appleton Laboratory,
Chilton, Oxfordshire, OX11 0QX, UK.

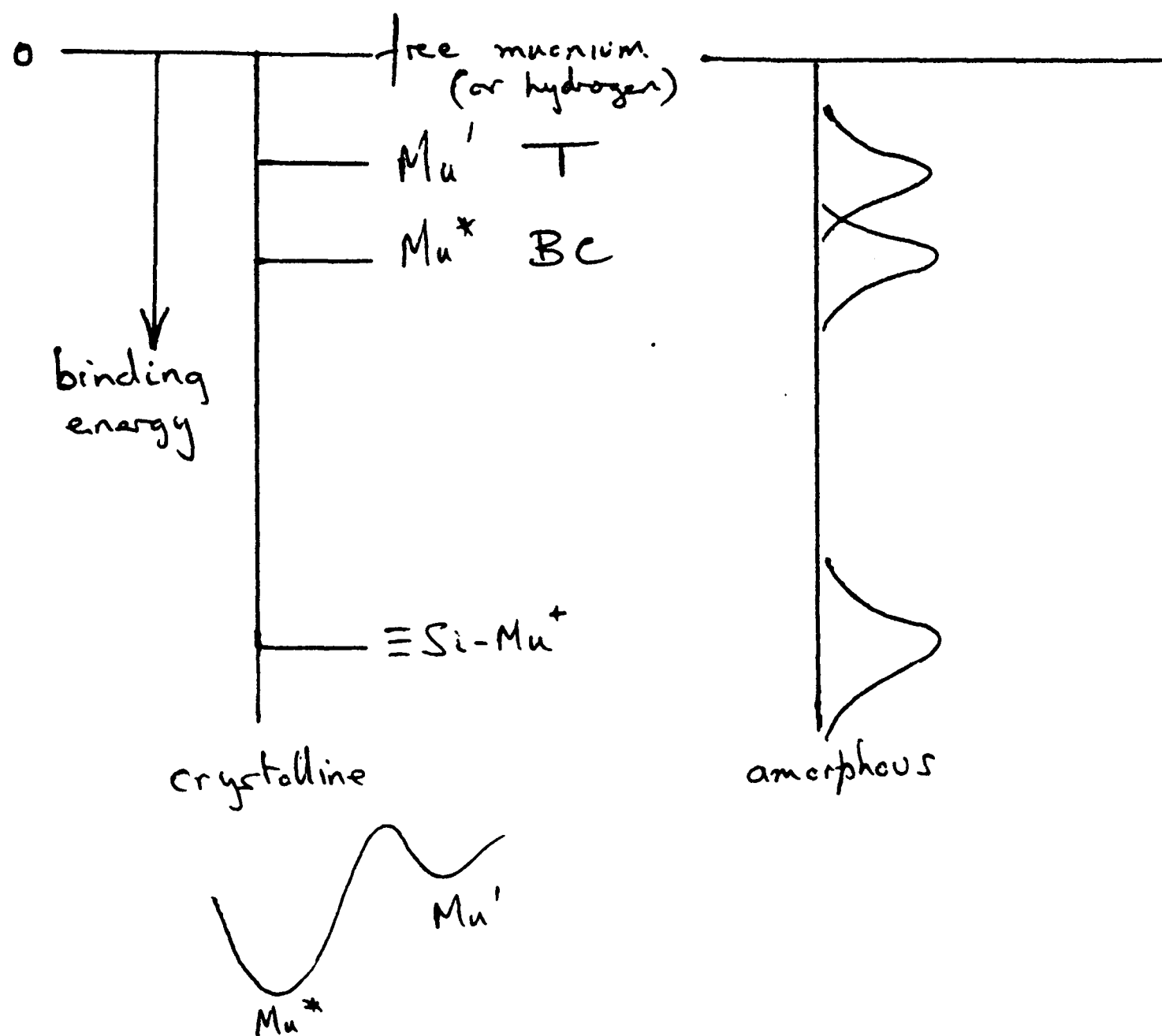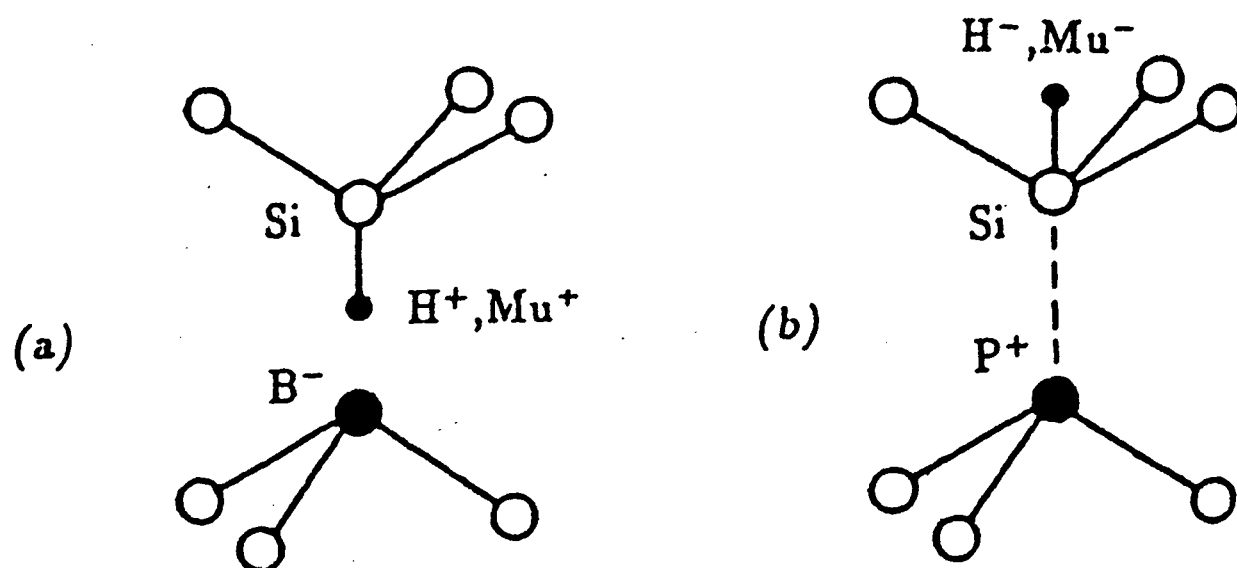This Lecture concerns the sites adopted by positive muons implanted in different materials. It examines how the nature of the material determines the muons' environment, as relevant to μSR studies. The terms *muon state* or *muonium state* are often used (these are not to be confused with the spin states). The guiding principle is that muons, like protons, cannot remain as the free particles once thermalized in matter, whether in gases, liquids or solids. They seek to lower their energy by association with electrons, in inert materials by the formation of muonium – the bound state with a single electron – and in more reactive hosts by becoming intimately incorporated into the structure of the lattices or molecules. Physicists refer to this as *localisation* and *local electronic structure*; chemists simply call it bonding. Analogies with the chemical behaviour of protons or atomic hydrogen are invaluable, provided proper account is taken of the larger zero–point energy of the muon when confined or bound. This leads into those applications of μSR which use the muon to mimic the proton, or muonium to model the behaviour of hydrogen in materials.

The relevant properties of atomic muonium are given, followed by a description of how these are modified in various hosts, dielectric, semiconducting, molecular and metallic. The different possibilities are well illustrated by the muonium states observed in the different allotropes of carbon.

1. MUONIUM

Atomic muonium is formed in a variety of of inert materials, gases, liquids and solids. That is, the initially energetic incoming muon picks up an electron at some stage during
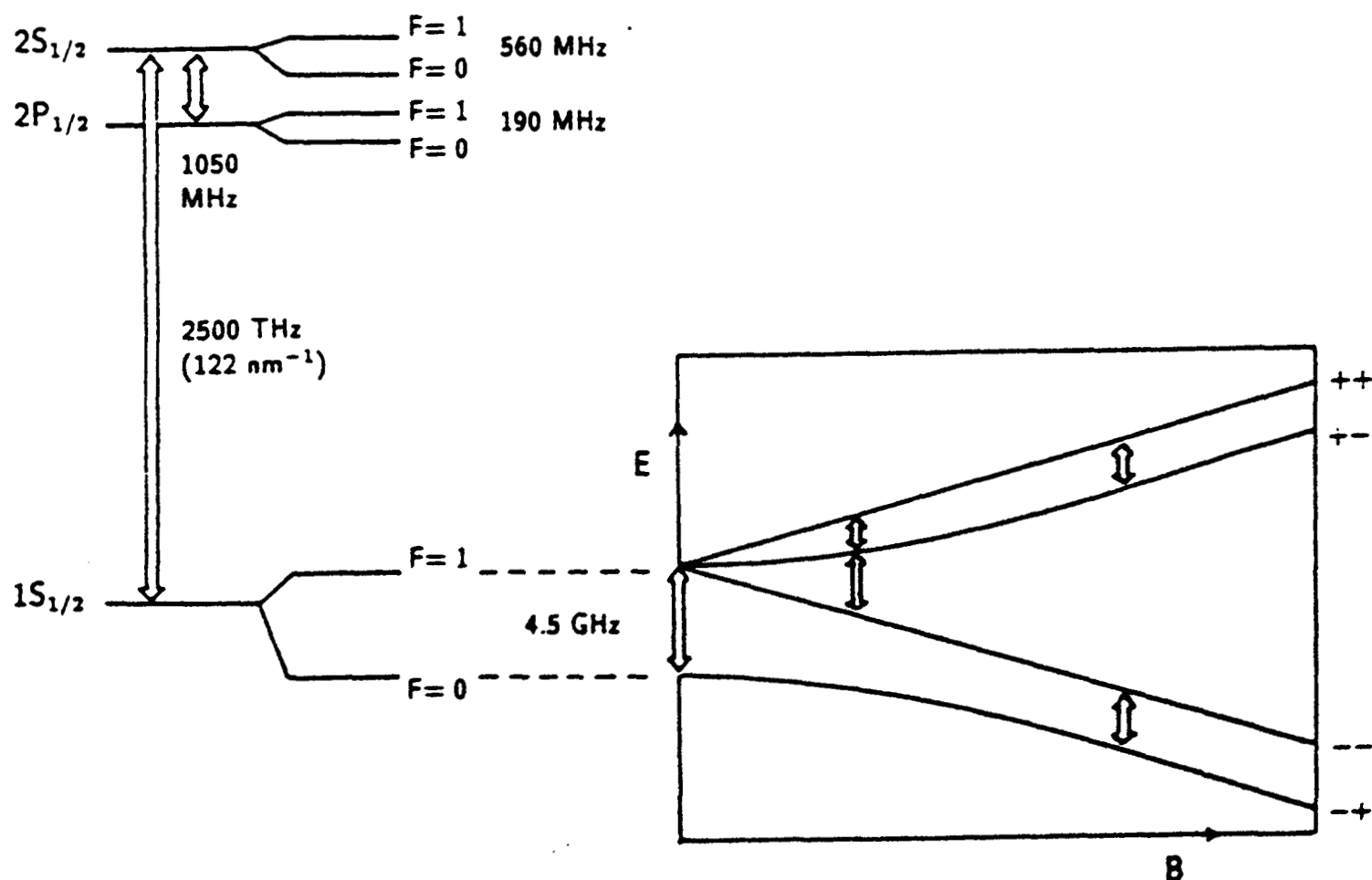
Energy levels for vacuum–state muonium.

the course of its thermalization. The closest approximation to the free–atom state is achieved for muonium formed in rare gases at low pressure, or formed in thin foil or fine powder production targets and ejected into a vacuum space beyond. This serves for the determination of the fundamental spectroscopic parameters [1].

1.1 Hyperfine interaction

We focus attention on the electronic ground state, described by a 1s hydrogenic wave-fuction. The electron spin S and muon spin I are coupled by an interaction of the form $A\mathbf{I.S}$, variously known as the hyperfine, Fermi or contact interaction. It results from the magnetic interaction between muon and electron which has the property – for a spherical or s–state electronic distribution – that it sums to zero except where the electronic wavefunction actually overlaps the nucleus. This is the origin of the name "contact" term and it implies that the *hyperfine constant*, A, is a measure of the electron density at the nucleus: $A \propto |\psi(0)|^2$. The hyperfine constant is usually expressed in units of frequency. For the vacuum–state atoms the value for muonium is greater than that for protium by the ratio (to within about 1%) of the magnetic moments of muon and proton. This implies essentially the same electron density or "spin density" at the nuclei, confirming the notion of muonium as a pseudo–isotope of hydrogen and serving as a starting point for examining the changes which arise on incorporation into materials.
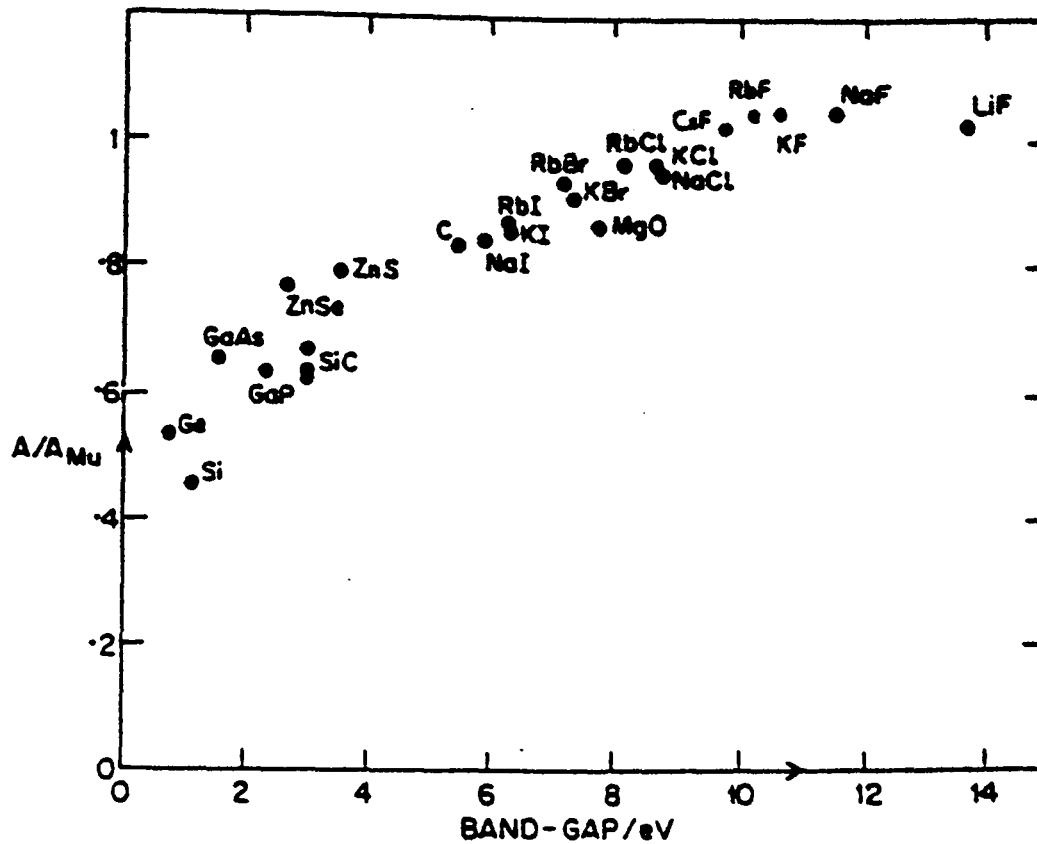
2. MUONIUM IN DIELECTRICS.

2.1 The Breit–Rabi diagram

The energy level scheme for ground state muonium in an applied magnetic field is shown framed in the above figure. It is known as the *Breit–Rabi diagram*, originally conceived for atomic hydrogen (*i.e.* protium). Characteristic frequencies corresponding to the transitions between the various states appear in the transverse–field muon spin rotation spectra, with intensities reflecting the field–dependent selection rules. In principle, the hyperfine constant may be deduced from these frequencies, but they are invariably too high to be seen at a pulsed source. The longitudinal field method known as *repolarization* may be used to get a rough value [2]. Alternatively, one could resort to RF resonance.

2.2 Influence of the medium

In inert and non–conducting solid media, muonium can exist in a form which closely resembles the atomic state, but which is located or *trapped* in the interstitial spaces of the lattice. In some alkali fluorides it is slightly higher than the vacuum–state value, as though the electronic wavefunction were compressed, increasing its amplitude at the muon. More commonly, the hyperfine constant is lower – in the semiconductors considerably lower – than in the free atom. This implies some *dilation* of the electronic wave function, *i.e.* its delocalisation onto the neighbouring atoms. In the group–IV elemental semiconductors, spin density on the muon falls as low as 50% of the free atom value.[1]

---

[1]The broad correlation with band–gap can be justified in a *molecular orbital* description: the greater the disparity between the levels of the states to be mixed, the smaller is the degree of mixing (*i.e. the more the muonium retains its atomic character*).

Hyperfine constant for interstitial muonium in semiconductors and dielectrics [3].

2.3 Level crossing resonance

Provided the muonium is static in the lattice, or nearly so, spin density on the surrounding atoms can be measured by a double resonance technique. The figure shows such a *level crossing resonance* spectrum for one of the cuprous halides, from which the muonium site may be assigned to the centre of the interstititial cage defined by four Cu^+ nearest neighbours.
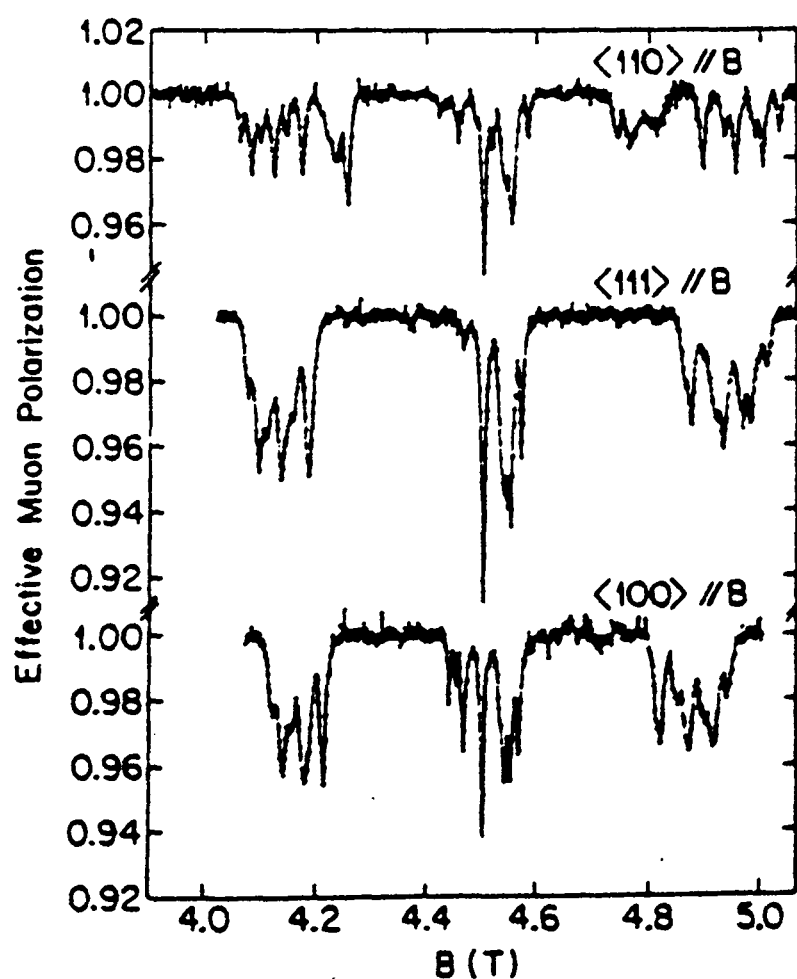
LCR spectrum for interstitial muonium in CuCl [4].

2.4 Zero point energy

In contrast to the free–atom case, where the spin density at the nucleus is the same for all isotopes, the spin density on the muon for muonium in each of the above materials is somewhat less than that on the proton for the equivalent states of interstitial hydrogen. This can be understood in terms of the greater zero–point energy of the lighter isotope, when confined in an interstitial cavity. The text–book cases of square wells and harmonic oscillators are illustrated in the sketch, with representative values of zero–point energy.
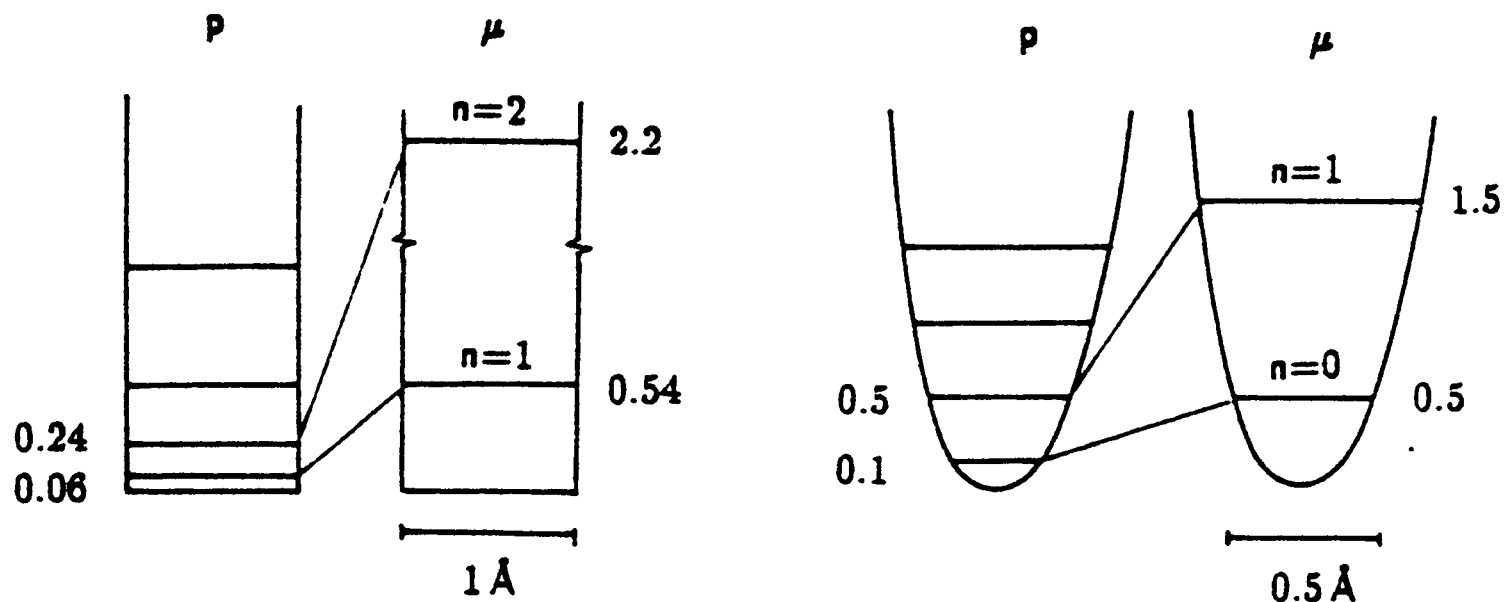

Zero point and vibrational energy levels for confined protons and muons.

In most cases the harmonic potential is the closer approximation to the *potential energy surface* which governs the dynamics, and two observations can be made. Firstly, the uncertainty in the muon position (the spread of the *nuclear wavefunction*) is greater than for the proton. That is, the muon is on average closer to the neighbouring atoms. One can imagine that this forces a greater overlap of the muonium *electronic wavefunction*, reducing its amplitude at the muon. Hence the isotope effect in hyperfine constant. Secondly, since the mass ratio is close to $1/9$, the muon zero point energy is about 3 times higher than that for the proton, in the harmonic approximation. This places its ground vibrational state about on a level with the first excited state for a proton. One can imagine the muon acting as a *hot proton* in its dynamical behaviour.

2.5 Non–spherical confinement

The sketch below illustrates topical examples of muonium confined in spherical and non–spherical cavities. These are muonium trapped *inside* the cages of the fullerene molecules – the *endohedral* states denoted Mu@C_{60} and Mu@C_{70}. The environment is spherically symmetric inside C_{60}; the muonium hyperfine interaction is isotropic and close to the free atom value. But for Mu@C_{70}, it develops a p–wave contribution to match the elongated cavity. The result is an additional zero–field splitting in the Breit–Rabi diagram (lifting the degeneracy of the triplet state) which manifests itself as a low–frequency oscillation in the zero–field spectrum. The isotropic component is correspondingly reduced.
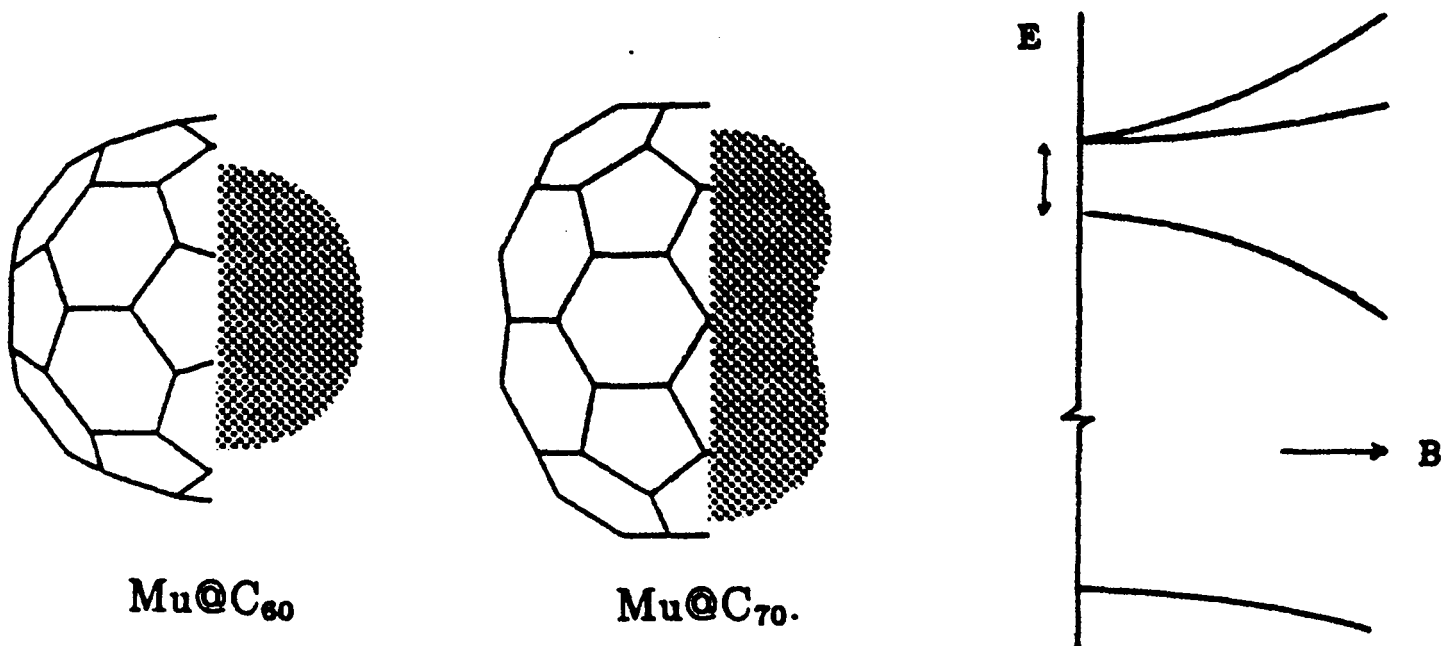
Contours of electronic density for muonium inside C_{60} and C_{70} and the additional zero-field energy splitting for axial asymmetry.

A small degree of anisotropy of the hyperfine tensor for muonium in quartz at low temperature, and also in ice, may also be described in these terms. Species where anisotropy results from spin density located on neighbouring atoms are introduced in the following sections.

3. MUONIUM IN SEMICONDUCTORS

Some classic spectra of the μSR literature are shown in the following figures. Spectra taken at the same low field in silica and silicon reveal a) the effect of the different hyperfine constant on the splitting of the two muonium lines and b) the existence of a group of lines in Si which is absent in SiO_2. The high field spectrum in gallium arsenide similarly reveals two distinct states of muonium. (Notice that these frequencies are well beyond the range accessible at a pulsed source.)
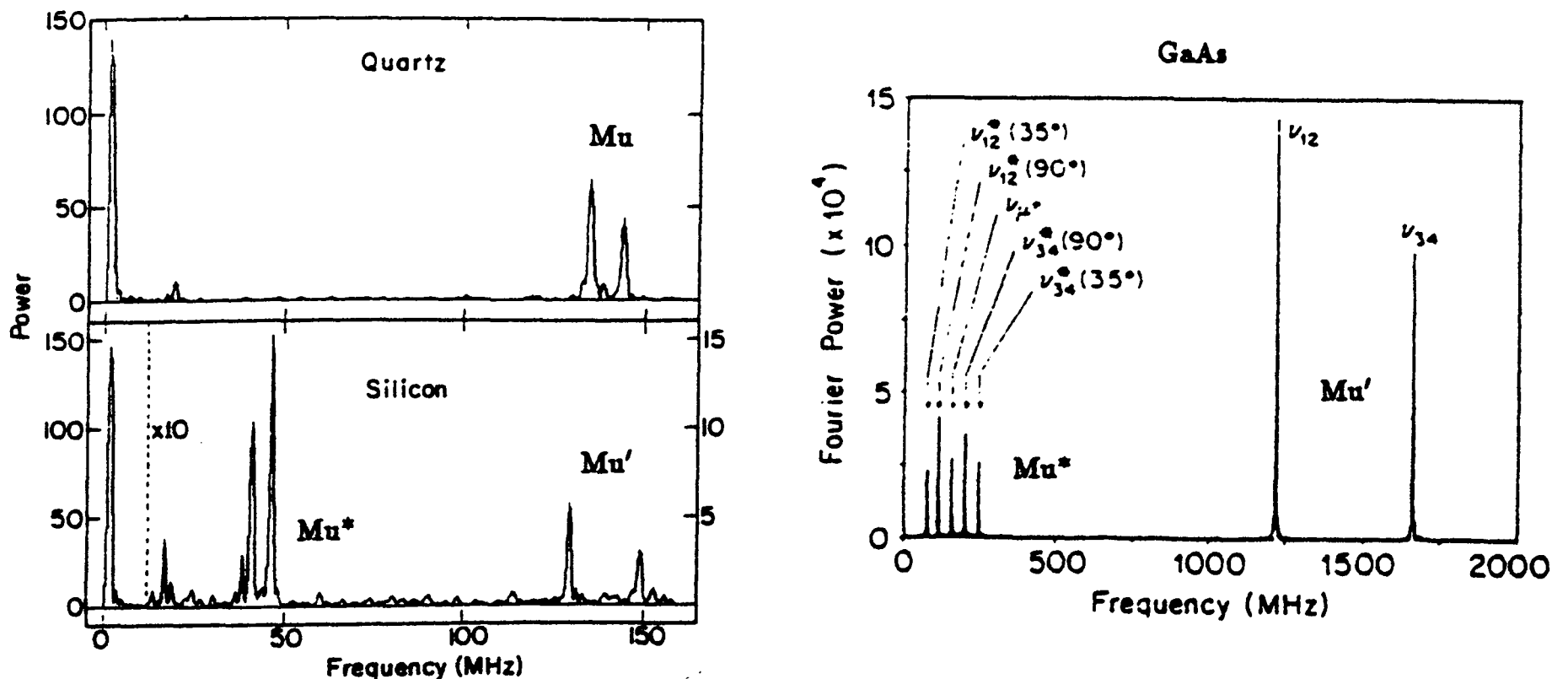
*Fourier transform μSR spectra for SiO_2, Si [5] and GaAs [6].*

3.1 Normal muonium, Mu'

In each case the pair of lines at the higher frequencies indicates an isotropic hyperfine interaction – these frequencies do not depend on the crystalline orientation in the magnetic field and are detectable equally well in polycrystalline samples. They correspond to the expected interstitial state, located at or near the large cage centres or *T–sites* in the tetrahedrally coordinated lattice. The term *normal muonium* is commonly used in the literature despite the low values of hyperfine constant in the semiconductors; in the following, the nomenclature Mu' is used to distinguish this from the free atom. It appears to be a mobile state, diffusing rapidly between the interstitial cages.

3.2 Anomalous muonium, Mu*

The lower frequencies are assigned to another state known variously as *anomalous muonium* or Mu*. For this state, the hyperfine coupling is strongly anisotropic. Careful single–crystal studies as a function of orientation determined the symmetry to be axial about the {111} directions and measured the principal components $A_{\parallel}$ and $A_{\perp}$ of the hyperfine tensor [7].

A Mu* state is observed in the group IV semiconductors Si and Ge, in diamond (which has the same crystal structure) and in a variety of tetrahedrally coordinated compound semiconductors. Despite detailed spectroscopic characterisation, its nature remained a longstanding puzzle. It was analysis of the tensor components in terms of the isotropic and dipolar components which eventually suggested the solution. The isotropic term, with coefficient $A_{iso} = \frac{1}{3}(A_{\parallel} + 2A_{\perp})$, is extremely small in the elemental materials, indicating negligible electron density at the muon site. The anisotropy term, with coefficient $B = \frac{1}{3}(A_{\parallel} - A_{\perp})$, has the form of a dipolar interaction; its magnitude for Mu* suggests that the unpaired electron is nonetheless located close by. Some supporting chemical reasoning pointed to a muon site at the *centre* of a silicon–silicon, or gallium–arsenic bond, as appropriate, so that the muon is at (in Si) or close to (in GaAs) a *node* of the singly occupied orbital [8].

$|\psi_e|^2 = 0$
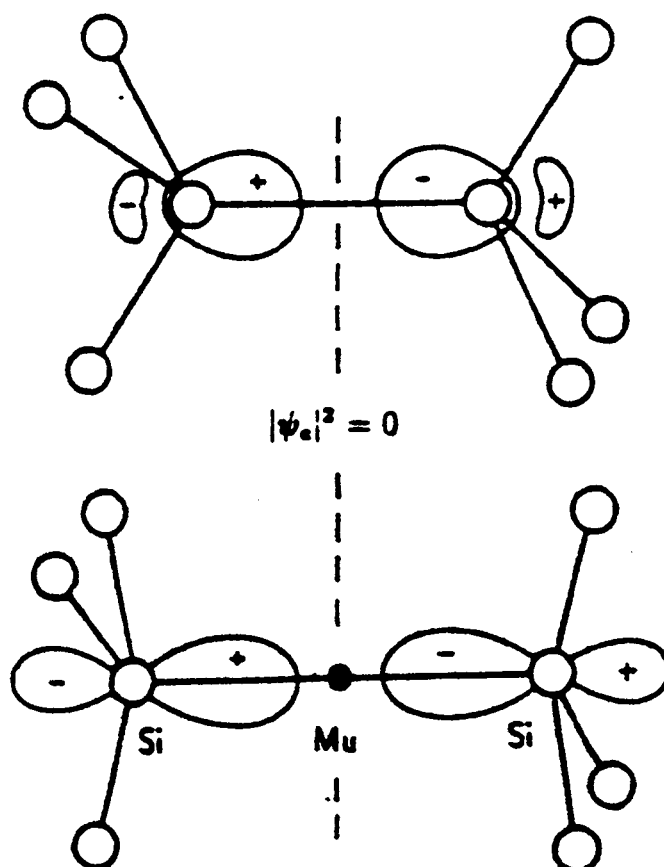
Antibonding orbital for a Si–Si pair as the basis for a model of Mu.*

This assignment is now substantiated by double resonance or *level crossing resonance* experiments which measure how the spin density is partitioned over the neighbouring atoms. Theoretical modelling reveals that, with a suitable *relaxation*[2] of the surrounding lattice, the bond centre in fact provides a deeper potential well for hydrogen or muonium than does the cage centre. The energy required to produce this distortion must represent a barrier to conversion of Mu' to Mu*, however. This would account for their coexistence in the low–temperature spectra, *i.e.* the *metastability* of Mu'.

3.3 Spin–polarization

In silicon, the small isotropic component of the hyperfine tensor is in fact negative, indicating a spin–polarization of bonding orbitals. The effect may be explained as follows. The unpaired electron has a wavefunction which is antisymmetric about the muon site, so the direct contact interaction is zero from this *singly occupied molecular orbital*. The two valence electrons forming the original Si–Si bond, on the other hand, have wavefunctions which are symmetric about the bond centre: their amplitudes are considerable at the muon site.[3] These electrons are spin–paired, so that their net contact interaction with the muon would also be zero if the spatial wavefunctions for the spin–up and spin–down electrons were identical. They are not quite identical, however. The presence of the unpaired electron is said to *polarize* the bonding orbitals. The net contact interaction is negative because the spin state with greater amplitude at the muon is opposed to that of the singly occupied orbital. Similar effects are found in molecular species (Section 4.3) and can contribute to hyperfine fields and *Knight shifts* in metals (Section 5.1).

3.4 Diamagnetic states

The localized electronic states of the muonium defect centres have energy levels which lie deep in the energy gap between valence and conduction band states. In the neutral paramagnetic states the levels are *singly occupied*. Loss of the electron (ionization) or double occupation of the level (when the Fermi level lies higher) both lead to muon states which are said to be *diamagnetic*. Theoretical modelling suggests that, in Si, Mu^+ is stable at the bond centre, $Mu^- = \mu^+ e^- e^-$ at the cage centre.

Diamagnetic muon states coexist with paramagnetic muonium in most dielectrics and semiconductors, in proportions which depend on the material and the temperature. In fluorides, for instance, a state analogous to the particularly stable $(F-H-F)^-$ ion is known (Section 4.2).

Pairing with other impurities can also lead to diamagnetic states; in semiconductors this would correspond to the *passivation* of dopants by hydrogen, a process which drastically alters electronic properties by removing electrically active levels from the gap.

A potentially important link with materials science, μSR studies of passivation, and of the interplay between charge state and location, promise to be fruitful in the future.

---

[2]The term is used here to mean a local distortion; this is not to be confused with *spin–lattice relaxation*.

[3]In fact, their charge density makes this an attractive site for the Mu^+ charge state, which is also stable at the bond centre.

4. MUONIUM IN MOLECULAR MATERIALS

The very limited solubility of hydrogen in materials such as the crystalline semiconductors makes its detection by conventional spectroscopies difficult or impossible. In such cases, muonium has provided a unique substitute. More generally, proton and hydrogen chemistry is well documented and can be used as a guide to the states expected of muons and muonium.

4.1 Protonation of bases

Protons are known to "stick" to to lone electron pairs such as commonly exist on oxygen or nitrogen, in the process known as *protonation*.[4] Positive muons are expected to do likewise and add, for instance, to water:
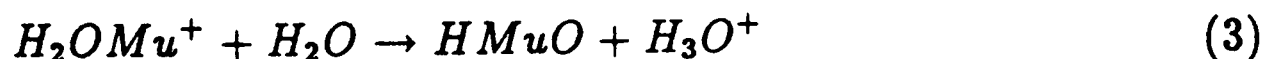
$$H_2O + \mu^+ \rightarrow H_2OMu^+, \tag{1}$$

or to a nitrogen molecule:

$$N_2 + \mu^+ \rightarrow N_2Mu^+. \tag{2}$$

(Note that the free particle is denoted here μ^+ and the chemically bound particle Mu^+.)

In the case of water, either the muon or one of the protons can then change its allegiance, with the net result that the charge migrates away to leave the muon substituted in a neutral molecule:

$$H_2OMu^+ + H_2O \rightarrow HMuO + H_3O^+ \tag{3}$$

4.2 Identification of diamagnetic states: level crossing resonance

The products of reactions such as (1–3), whether ionic or neutral, are all *closed shell, i.e. diamagnetic*. There is no unpaired electron in the vicinity of the muon, and therefore no hyperfine interaction. The same is true for the muonium states in semiconductors which are charged (Mu^- or Mu^+) rather than neutral, or which are paired with other impurities or dopants. The muon spin rotation spectrum for such species shows a single line at a frequency close to the muon Larmor frequency appropriate to the applied field. There is in principle a small *chemical shift*, due to diamagnetic shielding currents in the molecule, but these have only been measured in a few favourable cases.[5]

In crystalline materials, the site of diamagnetic states may often be determined from the orientation dependence of the transverse field μSR linewidth, and occasionally from the form of the zero–field relaxation function. The (F–Mu–F)$^-$ ion, for instance, shows a particularly distinctive zero field relaxation. Otherwise, there may be no signature in the μSR spectra of diamagnetic muon states which readily allows their chemical identity to be established. When the muon is located immediately adjacent to a *quadrupolar* nucleus ($J > 1/2$), however, muon level crossing resonance can provide such a signature. Level crossing resonance experiments use a longitudinal field to tune the muon Zeeman energy to match the combined Zeeman and quadrupolar energy on the neighbouring nucleus.

---

[4] Any substance which has such an affinity for protons, however weak, and can accept them in this manner – more usually by reaction with an acid – is known as a *base*.

[5] RF resonance at high fields offers the best promise for chemical shift measurements.
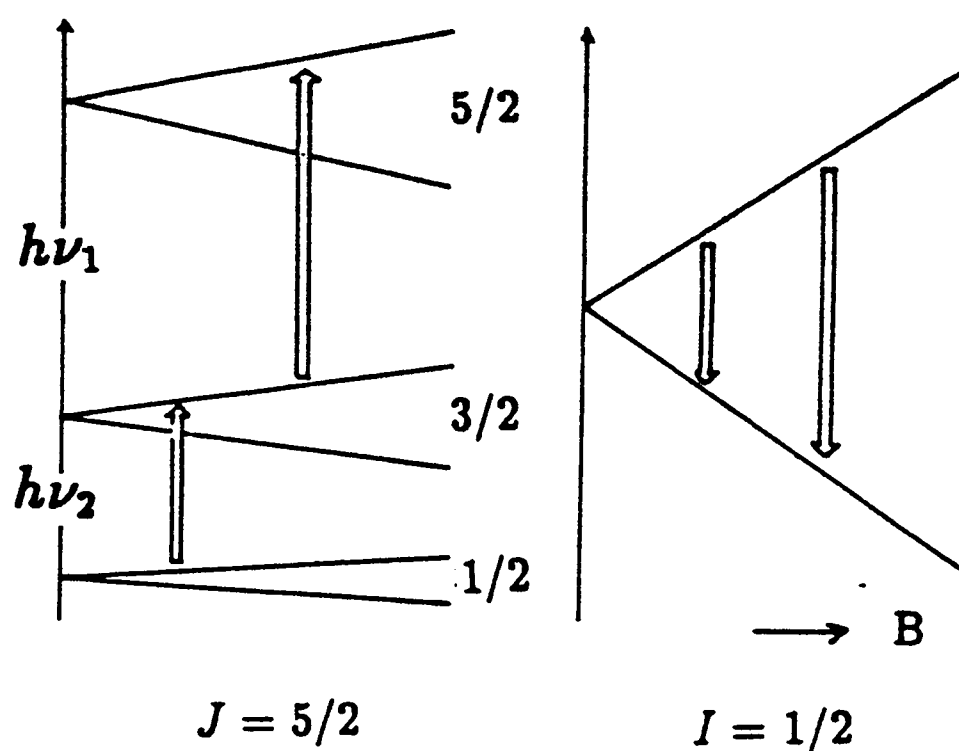
Resonant cross relaxation between a muon $(I = 1/2)$ and a nucleus with $J = 5/2$ (e.g. ^{17}O).

The muons then lose polarization by flip–flop transitions or *cross relaxation* with the neighbour. The technique also requires solid samples, but not necessarily single–crystals, since LCR spectra are only weakly dependent on orientation. The spectra provide a measurement of the quadrupole energy splittings which are characteristic of the molecular species, in the same manner as for interstitial muons in metals. Addition to oxygen and nitrogen has been demonstrated in this way, and the method applied to characterise muon sites in the oxide superconductors. The figure shows the spectrum for ice, recorded at ISIS, with resonances assigned to the substituted molecule HMuO and to the ionic intermdiary, thought to be a muon trapped at a defect in the ice structure.
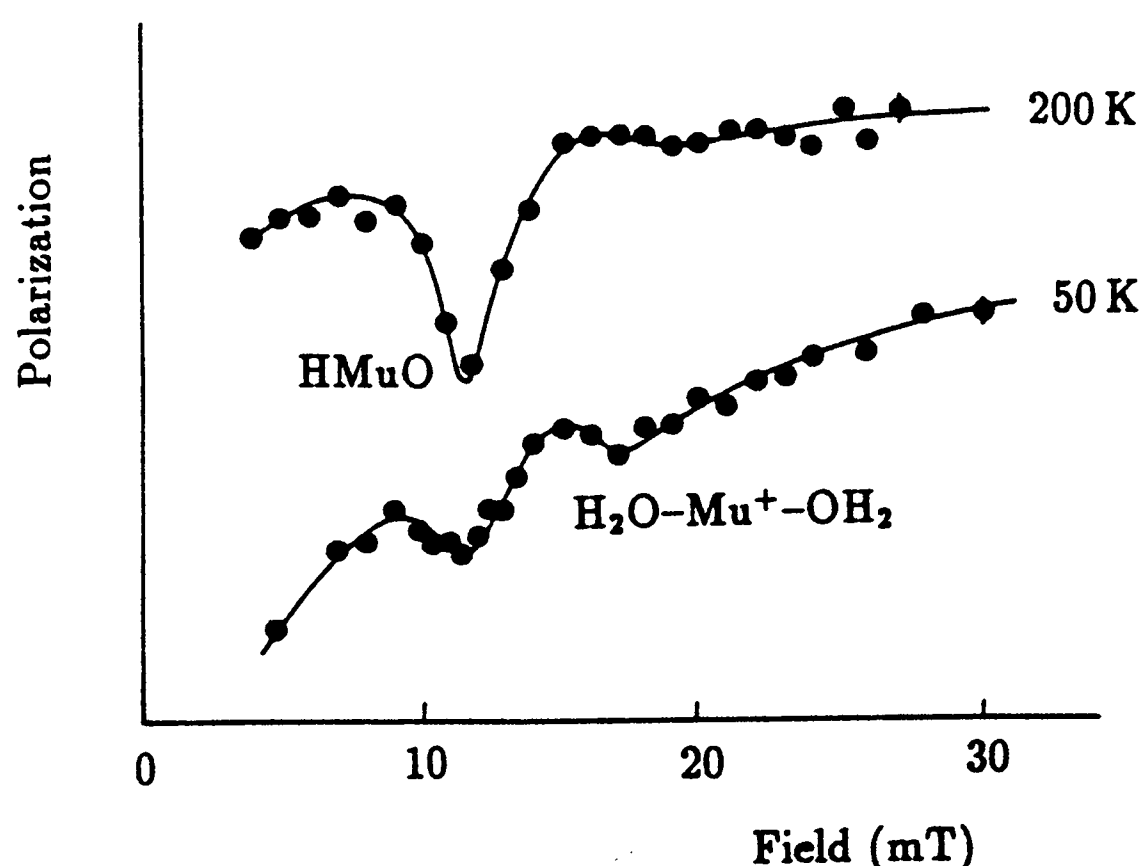
Level crossing resonance spectrum for ice, enriched with $H_2^{17}O$ [9].

4.3. ORGANIC RADICALS

A chemical reaction which is well known for atomic hydrogen is addition at multiple bonds in *unsaturated* organic compounds. Addition to the carbon–carbon double bond of ethylene, for instance, forms the *ethyl radical*, much studied by ESR spectroscopy:

$$H_2C{=}CH_2 \;+\; H\cdot \;\rightarrow\; \dot{C}H_2.CH_3 \tag{4}$$
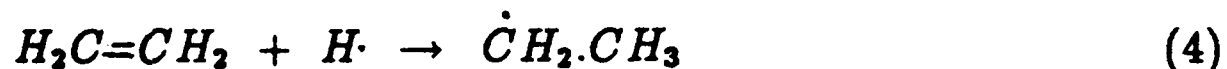
In this notation the dot is used to emphasize the existence of the unpaired electron spin, the term *radical* (sometimes also, especially in earlier literature, *free radical*) being used to to denote open–shell or paramagnetic molecules.[6]

Muonium does likewise, forming the *muonic* or *muonium–substituted* ethyl radical. This is the net result of implanting positive muons in ethylene, liquid or gas.

$$H_2C{=}CH_2 \;+\; \dot{Mu} \;\rightarrow\; \dot{C}H_2.CH_2Mu. \tag{5}$$
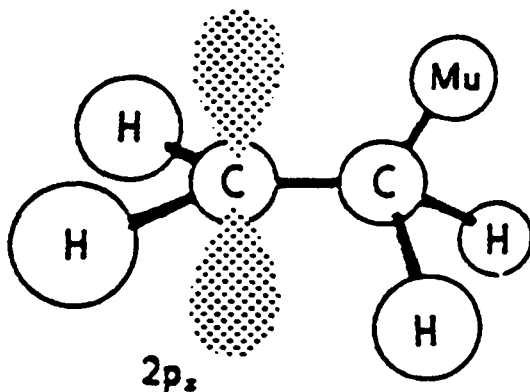
Structure of the muonic ethyl radical, with major spin density in a $2p_z$ orbital on one carbon atom, at the "radical centre".

In these paramagnetic species, there is again a hyperfine interaction between the muon and the unpaired electron. It is much smaller than in muonium, since the wavefunction of the unpaired electron is centred not on the muon but elsewhere in the molecule.

In the addition reaction, the double bond is broken or it reduced, saturating one carbon atom and leaving an unpaired electron spin located, largely, on the other.[7] The notation $\dot{C}H_2.CH_2Mu$ and the sketch showing the unpaired electron occupying a $2p_z$ orbital on this carbon atom give a rather misleading picture of total localization. In reality, the spin density "leaks" over the entire molecular frame.

Another favourite and much studied example is the muonium–substituted *cyclohexadienyl* radical, formed in benzene. *Conjugation* of the bonds results in extensive delocalisation of the electronic spin around the ring [10].

$$C_6H_6 \;+\; Mu \;\rightarrow\; C_6H_6Mu. \tag{6}$$

---
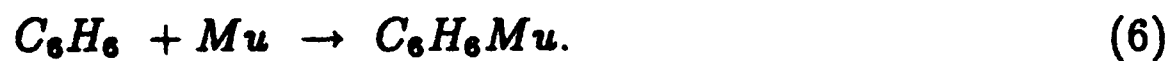
[6]The ethyl radical, in common with all those discussed below, has an electronic doublet ground state, with g–factor close to 2, indicating that the electronic spin is the dominant contribution to the magnetic moment.

[7]Roughly stated, the addition reaction leaves a *dangling bond* on this atom.

The muon–electron hyperfine interaction for such species is expected to be anisotropic. The isotropic component is a measure of the contact interaction, including the direct term representing the density of the singly–occupied molecular orbital at the muon, plus any indirect term representing spin–polarization of the bonding (doubly–occupied) orbitals. In the ethyl and cyclohexadienyl radicals it is of order one tenth the muonium value. The anisotropy represents the dipolar interaction from an electron distribution which, in molecular species, is rarely symmetric about the muon site. Being a traceless term, however, it has the property of being averaged to zero by fast tumbling of the molecules in the fluid phases. Liquid and gas phase spectra therefore give the isotropic term directly. In high field spectra it is just the sum of the two frequencies.
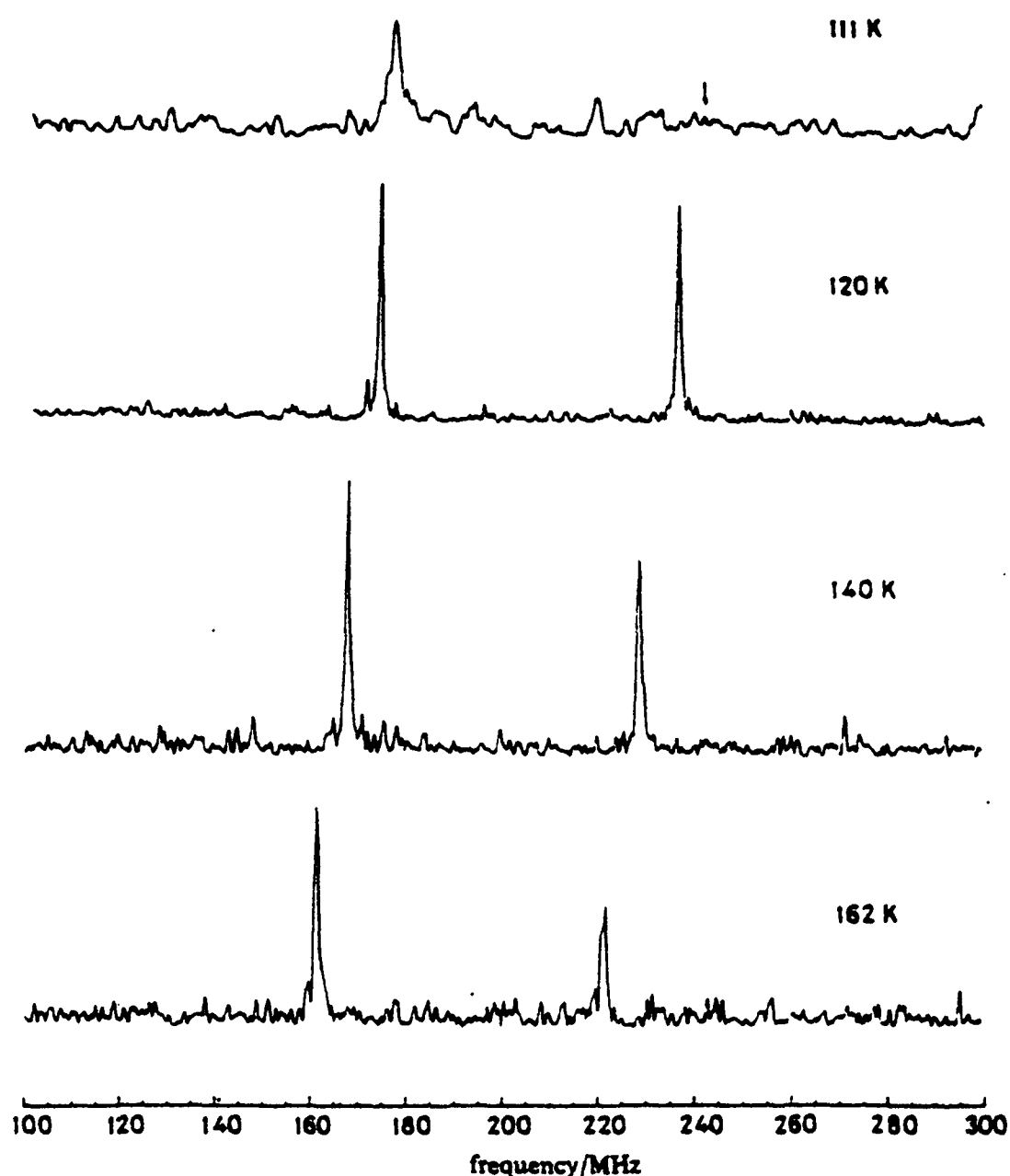

Fourier transform spectra for the $CH_2.CH_2Mu$ radical in liquid ethylene (anisotropy broadening is apparent near the freezing point) [11].

Radical formation by muonium addition at multiple bonds involving oxygen and nitrogen is also known. The temperature dependence of the hyperfine constant is informative on low–lying internal modes of vibration (in the muonic ethyl radical, for instance, on the torsional libration or hindered rotation about the C–C bond) [11]. Level crossing resonance can be used to measure the hyperfine coupling to the other nuclei, *i.e.* to map out the spin density throughout the molecule. Many of the radicals are highly reactive transient species, and μSR detection serves also to determine their chemical lifetimes, in studies of reaction kinetics. Gas phase studies of complex radicals by conventional ESR prove impossible, so here μSR studies of the muonium–substituted counterparts are particularly noteworthy.

4.4 $C_{60}Mu$

A topical example of a particularly interesting muonic radical is $C_{60}Mu$, the muonium *adduct* of C_{60} fullerene. This is distinct from the endohedral complex, $Mu@C_{60}$, describe in Section 2.4.[a] $C_{60}Mu$ is the result of external addition, muonium attacking one of the double bonds much as in the reaction with ethylene, so that the muon is located outside the fullerene cage, covalently bound to a single (saturated) carbon atom. $C_{60}Mu$ is the analogue of the monohydride of C_{60}; it has the distinction of having been detected in μSR studies *before* $C_{60}H$ was recognised in ESR studies.

The μSR spectrum is remarkable in showing strong narrow lines over a considerable temperature range, for *solid state, powder* samples of C_{60}. For the other muonic radicals the solid state spectra, unless from single-crystal samples, are broadened and weakened by the hyperfine anisotropy, often beyond detection. In solid C_{60}, however, the individual molecules can reorient, whilst their centres of mass remain fixed on the lattice structure. The result is a progressive *motional narrowing* of the μSR line-widths in the phase between 90 and 260 K, from which the correlation time for the reorientation can be deduced, with extreme narrowing corresponding to liquid-like rotational diffusion in the phase (still solid) above 260 K.
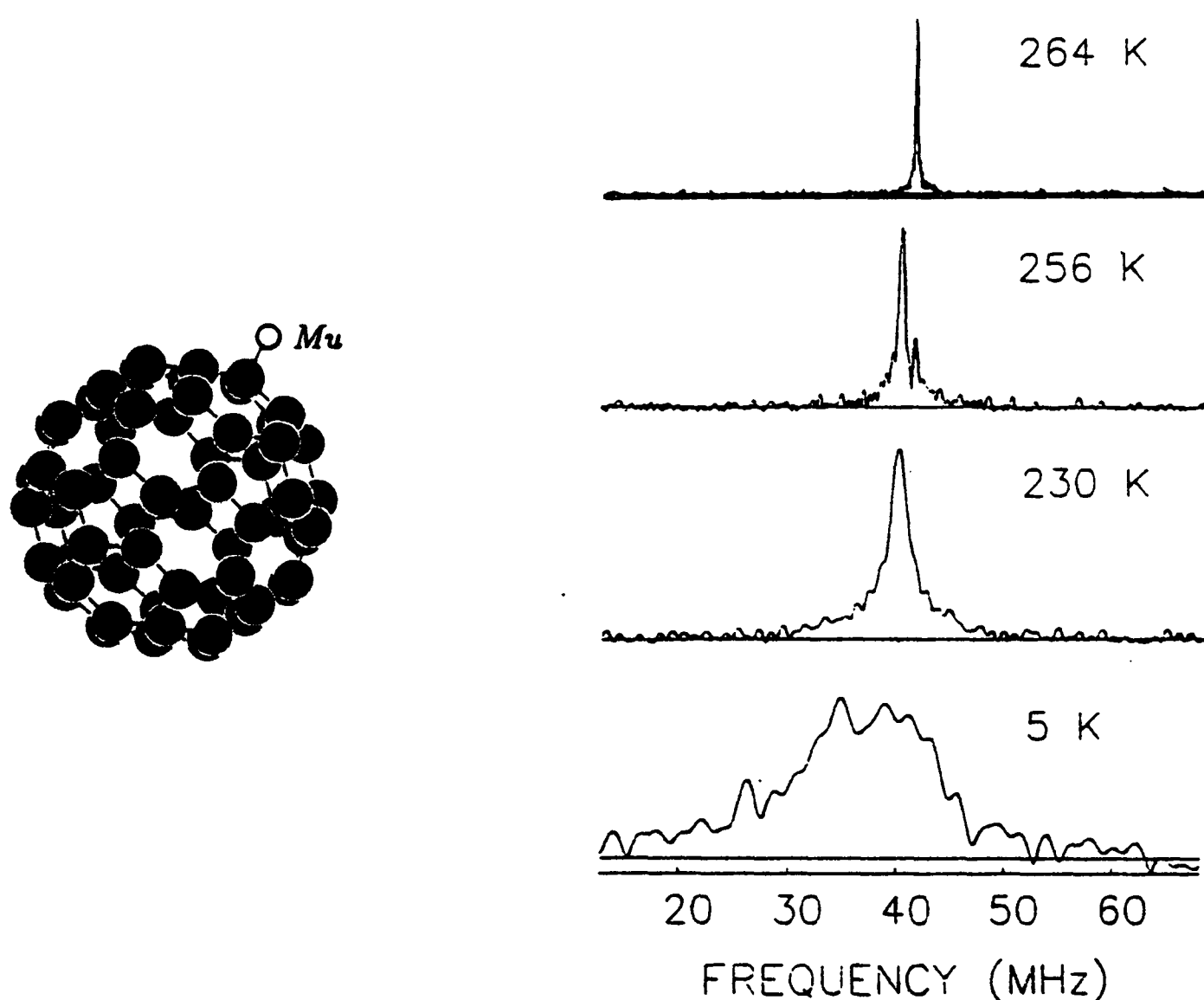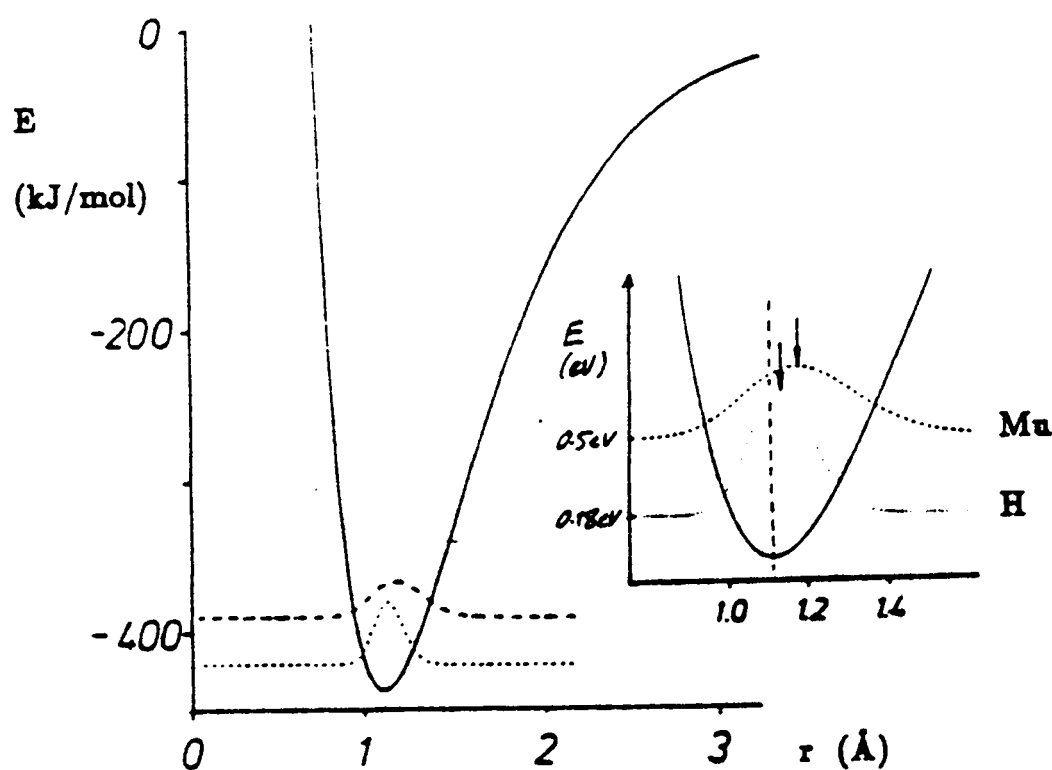

$C_{60}Mu$ and motional narrowing of one of its spectral lines [12].

---

[a]The endohedral state, $Mu@C_{60}$, provides another remarkable example of metastability in muonium studies: some potential barrier prevents reaction with the cage structure from inside. Its signal coexists with that of $C_{60}Mu$ in the μSR spectrum.

4.5 The hyperfine isotope effect

In the muonium-substituted organic radicals, the spin density on the muon is invariably greater than it is on the equivalent proton in the unsubstituted radical.[9] This is revealed by comparing the *reduced hyperfine constant* $A_\mu.\mu_P/\mu_\mu$ from the μSR measurement with the proton hyperfine constant A_p from the ESR measurement. ($\mu_P/\mu_\mu = \gamma_p/\gamma_\mu$ is the ratio of the magnetic moments of proton and muon.)

The radicals $C_{60}X$ (X = H, Mu) are ideal for a discussion of the origin of this effect. Both H and Mu are light atoms bonded to the heavy C_{60} substrate. Their normal modes of vibration are therefore very similar; we focus attention on the bond-stretching mode. A Morse potential describes the total energy of the molecule as a function of the bond length. This is just a 1D cut through the potential energy surface which governs the proton or muon dynamics; within the Born-Oppenheimer or adiabatic approximation it is the same for all isotopes.[10] If there were a hydrogen isotope with infinite mass it would sit at the *equilibrium* position at the bottom of this well, *i.e.* the bond length would be well defined. By virtue of its light mass and zero point energy, the bond length for hydrogen is not fully determinate, but must be described by a spread in the *proton* wavefunction. The zero point energy for muonium and rms spread of the *muon* wavefunction are higher still. The situation may be compared with the harmonic oscillator potential sketched in Section 2.4. The result of a degree of *anharmonicity* in the Morse potential is that the mean bond length (as well as its variance) is slightly greater for X = Mu than for X = H.


Morse potential for the C-X bond and zero-point energies for X=H and X=Mu [13].

The relevance of this to hyperfine coupling is that spin density on the nucleus X is also a function of bond length. This function, like the Morse curve, is also common to all isotopes X. In fact it is a non-linear, rapidly accelerating function: one can imagine that stretching the bond corresponds to withdrawing a hydrogen or muonium atom from the molecule, so that spin density on the proton or muon rapidly approaches the free atom value. The measured hyperfine constant corresponds to an average value, weighted by the nuclear density (the square of the nuclear wavefunction). It is greater for X = Mu than for X = H both by virtue of the longer mean bond length and (since the function is non-linear) the greater variance.
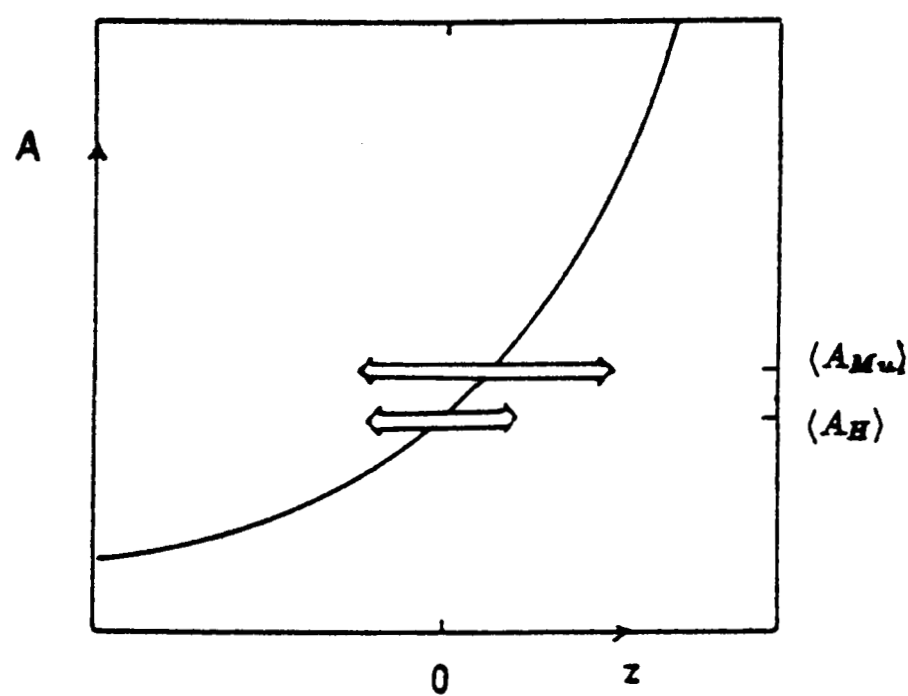
Variation of spin density on X with C–X bondlength and the different averages to be taken for X = H, X = Mu [14].
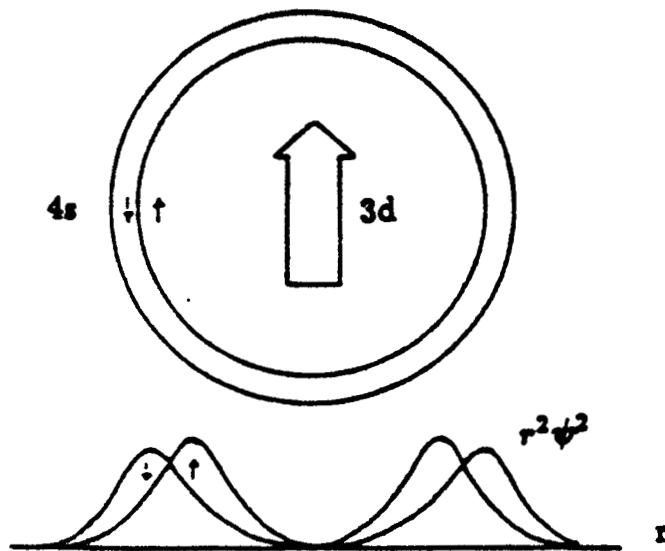
5. METALS

5.1 Screening

Muonium is not formed in simple metals. This seems paradoxical, in that conduction electrons are always at hand, apparently available to be picked up by the muon. In fact the conduction electron density is too high to allow a bound state with a single electron to be formed. The density of these mobile charges adjusts in response to the muon's presence to screen it's Coulomb potential.[11] The muonium binding energy is reduced, not exactly to zero, but to such a shallow level that the lifetime broadening exceeds its depth. Electrons hop and off the muon, so to speak, in rapid succession.[12] Some of the electrons have spin-up, some spin-down. In magnetic metals in their ordered state, the conduction electron polarization can be considerable, and give rise to huge hyperfine fields at the muon.

---

[11]An exception is C_{60}, where the muonium signal persists in material which is doped to become metallic or superconducting. Inside the cage, the muon is insulated from the mobile charges outside.

[12]Note that in muonium and in the muonic radicals, the electron spin states are usually long lived, so that the effective hyperfine field at the muon takes two discrete values, $(2\pi/\gamma_\mu)A.S_z = \pm(\pi/\gamma_\mu)A$, according as the electron is spin-up or spin-down. For short-lived spin states, or rapid *spin-exchange* the two spectral lines collapse to one, exhibiting a *paramagnetic shift* $A.\langle S_z\rangle$.

Exchange polarization of outer by inner electrons in magnetic metals.

In diamagnetic metals the interaction is observed as a *Knight shift* – a small proportional change in the muon Larmor frequency from the value appropriate to the externally applied field [15]. The Zeeman energy $\hbar\gamma_\mu H I_z$ calculated as though for a free muon becomes $(1 + K)\hbar\gamma_\mu H I_z$, with

$$K \propto \rho_\uparrow - \rho_\downarrow. \tag{7}$$

Expressing the electron spin density at the muon in an obvious notation, and with a judicious rearrangement of terms, one can write

$$\rho_\uparrow - \rho_\downarrow = n_\uparrow|\psi_\uparrow|^2 - n_\downarrow|\psi_\downarrow|^2 \tag{8}$$

$$= \frac{1}{2}(n_\uparrow - n_\downarrow)(|\psi_\uparrow|^2 + |\psi_\downarrow|^2) + \frac{1}{2}(n_\uparrow + n_\downarrow)(|\psi_\uparrow|^2 - |\psi_\downarrow|^2). \tag{9}$$

In simple treatments only the first term is retained, evaluated at the Fermi surface. The Knight shift is proportional to the difference in the *populations* of spin–up and spin–down states, *i.e.* the electronic susceptibility. The second term contributes when the spin–up and spin–down wavefunctions are not identical. It is analagous to the *spin polarization* effects noted for bonding electrons in semiconductors (Section 3.3) and organic radicals (Section 4.3).

5.2 the small polaron state

The local accumulation of conduction electron density largely screens the muon's positve charge within a distance comparable with the interatomic spacing. The absence of electrons with short enough wavelength to accomplish this smoothly results in oscillations or "diffraction haloes" at greater distances. The spin density oscillations lag in phase relative to the charge density oscillations. Modelling this response accurately is a severe test of screening theory and μSR data have provided a valuable stimulus in this area.

The muon site in metals is invariably interstitial, and the same as that adopted by the screened proton state of hydrogen in metals. The analogy makes implanted muon studies invaluable in modelling certain aspects of the behaviour of hydrogen in metals, especially in metals such as copper where hydrogen itself is too insoluble to be studied by conventional techniques. Imperfect screening of the muon or proton charge implies that the neighbouring ion cores will be slightly repelled, producing a local elastic distortion on relaxation of the lattice.[13]

---

[13]Phase transitions in the concentrated hydrides can sometimes be described in terms of this distortion exceeding the elastic limit.
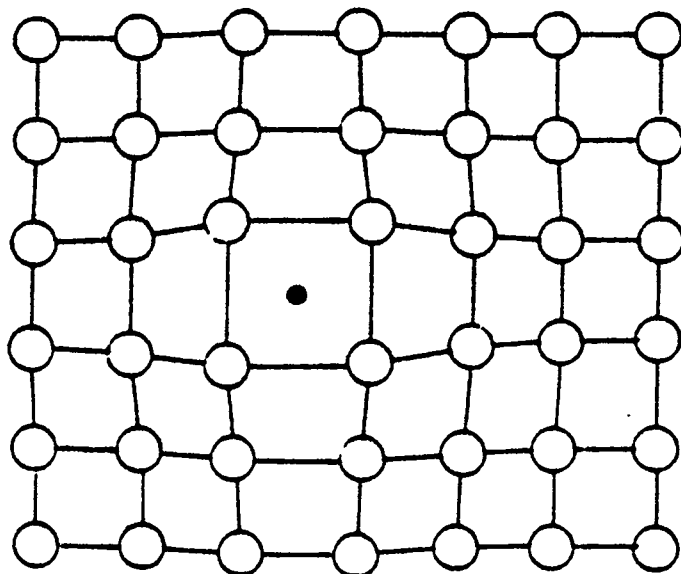
Local elastic distortion.

The lattice relaxation results in a lowering of the interstitial potential at the muon or proton site, favouring localisation. Muons and protons are said to *self-trap* in this

manner. The whole entity, *i.e.* interstitial particle plus screening charge plus elastic distortion, is referred to as a *small polaron* state. Erudite works refer to the particle "dressed" with electron and phonon clouds.

5.3 Quantum diffusion

The localisation or self–trapping does not imply that the small polaron state is necessarily immobile. In many metals, interstitial muons and protons diffuse with remarkable rapidity. μSR and other studies have been concerned with understanding the nature of the elemental step, *i.e.* the mechanism by which the small polaron state can move between adjacent sites. This is not expected to be identical for muons and protons, though the comparison of their mobility may be valuable, with the muon more likely to exhibit *quantum diffusion*: by virtue of its greater zero–point energy in the interstitial well, the muon is often able to tunnel through the intervening barrier to the next site more readily than the proton.

The necessity to transfer the elastic distortion is common to muons in metals and muonium in non–metals. The temperature dependence of mobility is not necessarily monotonic: it can show a remarkable minimum in systems of both types. The low temperature *quantum mobility* is modified in metals by the necessity to carry the screening charge, with evidence that this does not always follow the muon motion adiabatically.

Topical problems include how to distinguish *coherent* tunnelling (best described by band–like or propagating states, which are *scattered* by defects or thermal excitations) from *incoherent* tunnelling (best described by localised states moving step by step in a random walk) and how to express the transition between the two.

6 SUMMARY

6.1 Ionic *vs* covalent bonding, diamagnetic *vs* covalent states

In summary, the muon does not remain as a bare particle when implanted and thermalized in matter, but enters into chemical association with the host. An ionic description can sometimes be used; in metals this will imply an associated screening charge; in non–metals purely electrostatic considerations will be modified by varying degrees of covalency and consequent directional bonding. Muonium can exist as the trapped interstitial atom or react to become covalently bound in molecular species.

In diamagnetic metals and in closed–shell molecular species, the muon spin rotation or resonance spectrum displays a single frequency, displaced from the Larmor frequency by a small Knight shift (metals) or chemical shift (molecules).

When the wavefunction of unpaired or spin polarized electrons has some density at the muon site, large hyperfine fields can add or subtract to the external or distant–dipole fields which the muon experiences. Characteristic multiple frequencies appear in the μSR spectra when the electron spin states are long lived; an average paramagnetic shift results when they fluctuate rapidly, or when an ensemble of conduction electrons is involved.

Atomic muonium is itself paramagnetic, as are the open–shell molecules or radicals formed by muonium addition to unsaturated organic compounds. In the trapped atom state of muonium, the electronic moment and wavefunction are centred on the muon but subject to delocalization over the neighbouring atoms. In the Mu* state, which appears unique to the tetrahedrally coordinated semiconductors (including diamond), and in the radicals, major spin density is located elsewhere, on neighbouring atoms. The isotropic component of the hyperfine tensor provides a measure of the spin density on the muon.

6.2 Carbon from soot to diamond

Muon states in the different allotropes of carbon illustrate most of these possibilities. In graphite, which is commonly used as a standard of asymmetry in μSR experiments to calibrate polarization, all implanted muons reach a diamagnetic state. A large and anisotropic Knight shift to the muon Larmor frequency reflects the almost 2D character of the electronic conduction in this material. Diamond shows the trapped–atom Mu' state coexisting with the Mu* state (in which muonium can be said to have reacted with the diamond lattice); thermal conversion from Mu' to Mu* in diamond is evidence for the metastability of Mu'. The fullerenes also show the metastable trapped atom state, insulated by some potential barrier against reaction from within the cage. But reaction from outside the cage, by addition at a double bond, creates muonium adduct radicals similar to those formed in other unsaturated organic compounds.

References

[1] For recent reviews see V.W. Hughes, Z. Phys. C – Particles and Fields **56** (1992) S35 and K. Jungmann, Z. Phys. C – Particles and Fields **56** (1992) 59.

[2] Ted Davis' Lecture.

[3] S.F.J. Cox, J. Phys. C: Solid State Physics **20** (1987) 3187: Implanted muon studies in condensed matter science.

[4] J.W. Schneider, Thesis, Zurich University (1990); see also J.W. Schneider *et al.* Proc. 'μSR'90: Hyp. Int. **64** (1990) 543.

[5] J.H. Brewer, K.M. Crowe, F.N. Gygax, R.F. Johnson, B.D. Patterson, D.G. Fleming and A. Schenck, Phys. Rev. **31** (1973) 143.

[6] R.F. Kiefl, J.W. Scneider, H. Keller, W. Kündig, W. Odermatt, B.D. Patterson, K.W. Blazey, T.L. Estle and S.L. Rudaz, Phys. Rev. **B 32** (1985) 530.

[7] B.D. Patterson, Rev. Mod. Physics **60** (1988) 69.

[8] S.F.J. Cox and M.C.R. Symons, Chem. Phys. Lett. **126** (1986) 516.

[9] S.F.J. Cox, M.C.R. Symons and J.A.S. Smith Proc. μSR'90: Hyp. Int. **65** (1990) 993.

[10] E. Roduner, The Positive Muon in Free Radical Chemistry (Springer Verlag Lecture Notes in Chemistry **49** 1988).

[11] M.J. Ramos, D. McKenna, B.C. Webster and E. Roduner, J. Chem. Soc. Faraday Trans. I **80** (1984) 267.

[12] R.F. Kiefl, J.W. Shneider, D.M. Garner, M. Senba, A.C. Gonzalez, J.R. Kempton, D.J. Arsenaeau, K. Venkateswaran, P.W. Percival, G. Wei, S. Wlodek, K. Kojima, W.J. Romanov, J.P. McCauley Jr., N. Coustel, J.E. Fischer and A.B. Smith III, Phys. Rev. Lett. **68** (1992) 1347.

[13] E. Roduner and I. Reid, Israel J. Chem. **29** (1989) 3.

[14] T.A. Claxton, A.M. Graham, S.F.J. Cox, Dj.M. Maric, P.F. Meier and S. Vogel, Proc. μSR'90: Hyp. Int. **65** (1990) 913.

[15] A Schenck, Muon Spin Rotation Spectroscopy (Bristol, Hilger, 1985).